

AC ELECTRIC TRAPPING OF NEUTRAL ATOMS

SOPHIE SCHLUNK

AC Electric Trapping of Neutral Atoms

Sophie Schlunk

Thesis Radboud Universiteit Nijmegen - Illustrated

With references - With summary in Dutch and English

ISBN 978-3-00-024481-0

NUR: 926

Subject headings: Low Temperatures / Electric Fields / Cold Atoms

Cover: Design by the author. Front: Absorption images of the atom cloud in the ac trap with the electric fields on. Back: Phase space plots of the trapped atom cloud at different phases of the ac switching cycle.

AC ELECTRIC TRAPPING OF NEUTRAL ATOMS

EEN WETENSCHAPPELIJKE PROEVE OP HET GEBIED VAN
DE NATUURWETENSCHAPPEN, WISKUNDE EN INFORMATICA

PROEFSCHRIFT

TER VERKRIJGING VAN DE GRAAD VAN DOCTOR
AAN DE RADBOUD UNIVERSITEIT NIJMEGEN
OP GEZAG VAN DE RECTOR MAGNIFICUS PROF. MR. S.C.J.J. KORTMANN
VOLGENS BESLUIT VAN HET COLLEGE VAN DECANEN
IN HET OPENBAAR TE VERDEDIGEN
OP VRIJDAG 22 AUGUSTUS 2008
OM 13.30 UUR PRECIES

DOOR

SOPHIE SCHLUNK

GEBOREN OP 13 AUGUSTUS 1976
TE SCHWÄBISCH HALL, DUITSLAND

PROMOTOR : PROF. DR. G.J.M. MEIJER
COPROMOTOR : DR. W. SCHÖLLKOPF
FRITZ-HABER-INSTITUT DER
MAX-PLANCK-GESELLSCHAFT, BERLIN

MANUSCRIPTCOMMISSIE : PROF. DR. W.L. MEERTS

PROF. DR. C. ZIMMERMANN
EBERHARD-KARLS-UNIVERSITÄT, TÜBINGEN

DR. A.P. MOSK
UNIVERSITEIT TWENTE, ENSCHEDE

The work described in this thesis is performed as part of the research program of the “Stichting voor Fundamenteel Onderzoek der Materie” (FOM), which is financially supported by the “Nederlandse organisatie voor Wetenschappelijk Onderzoek” (NWO), and is performed at the FOM-Institute for plasmaphysics ‘Rijnhuizen’ in Nieuwegein, the Netherlands, and at the Fritz-Haber-Institut der Max-Planck-Gesellschaft in Berlin, Germany.

Danksagung

Ich hatte gerade meine Diplomarbeit abgegeben und war auf der Suche nach einer Doktorarbeit, als mir jemand zum ersten Mal von diesem interessanten Projekt in der Arbeitsgruppe von Gerard Meijer erzählt hat: Aufbau einer magneto-optischen Falle für Rubidiumatome, um dann Moleküle mit den kalten Atomen sympathetisch zu kühlen. Die Gruppe war momentan am FOM-Institut für Plasmaphysik ‘Rijnhuizen’ in Holland, würde aber bald nach Berlin umziehen, wo Gerard als neuer Direktor der Molekülphysik an das Fritz-Haber-Institut berufen worden war. Das Thema fand ich spannend und die Kombination Holland-Berlin hat mir auch gefallen. Ich bin dann nach Rijnhuizen gefahren, um mir die Gruppe anzusehen und habe mich dort sofort wohlgefühlt.

Es ist nun fünf Jahre her, dass ich meine Doktorarbeit am FOM-Institut in Holland angefangen habe. Hier möchte ich all denen danken, die zum Gelingen der Arbeit beigetragen haben.

Zuerst möchte ich Gerard dafür danken, dass er mir die Möglichkeit gegeben hat, meine Doktorarbeit in seiner Gruppe zu machen. Ich finde es bemerkenswert, dass Du trotz Deiner rasch wachsenden Gruppe so oft im Büro oder im Labor vorbeigeschaut hast, um den neuesten Stand der Dinge zu erfahren. Außerdem warst Du immer da, wenn wir Fragen hatten, oder Du kamst mit neuen Vorschlägen und Ideen vorbei. Ich möchte Dir auch für die offene, nette Atmosphäre in unserer Gruppe danken, mit so schönen Traditionen wie Kaffee & Kuchen, wenn es eine neue Veröffentlichung zu feiern gibt oder jemand Geburtstag hat.

Dann möchte ich Wieland danken, meinem ‘Copromotor’. Wieland, Du hast zusammen mit mir fünf Jahre am Experiment gearbeitet, um schließlich kalte Rubidiumatome in einer Falle einzufangen. Du hast mit Deinem Hintergrundwissen immer eine Idee gehabt, wie man weitermachen oder wie man ein Problem angehen könnte. Besonders beeindruckt hat mich immer Deine Fähigkeit, etwas so zu erklären, dass man es gut versteht. Und schliesslich hast Du meine Arbeit noch einmal gelesen und sorgfältig auf letzte Fehler durchgesehen.

Als nächstes möchte ich Adela danken. Adela kam im September 2005 mit ans Experiment, hat sofort die Ärmel hochgekrempelt und sich zusammen mit mir an die Laborarbeit gemacht. Wir haben lange Stunden im Labor verbracht und es schließlich geschafft, die Atome nicht nur magnetisch, sondern auch elek-

trisch zu fangen. Du hast immer dafür gesorgt, dass unsere Veröffentlichungen in bestem Stil abgefasst waren: 'Sophie, I don't really like this phrase'. Ausserdem hast Du Dir die grosse Arbeit gemacht, meine Arbeit als erste zu korrigieren, was sehr viel Zeit und Mühe gekostet hat. Danke dafür!!!

Then I want to thank Allard who was my supervisor in the first four months in Rijnhuizen and who initially planned the experiment in the Netherlands. When I entered the lab on my first working day in Rijnhuizen, the optical table was empty apart from the two diode lasers. From April to July 2003, Allard was a very patient teacher and I have learned a lot from him. Within these four months, we set up all the necessary optics for the magneto-optical trap. Due to Allard's preparation and advice, we finally got our first MOT going on August 28, 2003. Thanks Allard, for your excellent planning of the experiment and also that you still had time for our questions when we had already moved to Berlin!

Thanks also to the people in Rijnhuizen who helped to set up the experiment, especially the workshop who built the MOT coils and the Zeeman slower. A special thanks to Paul who was always there to give a hand when we needed help.

Dann möchte ich mich bei Peter bedanken, der uns in Berlin viel beim Aufbauen der bewegten Quadrupolspulen und der elektrischen Falle geholfen hat. Er war DER Vakuum-Experte und kannte alle (Zauber)Tricks, wenn es Probleme gab.

Danke der Elektronikwerkstatt und insbesondere Georg Heyne und Victor, die uns beim Aufbau der Elektronik für unsere Fallen immer zur Seite standen und uns jederzeit auch bei kleineren Problemen unterstützt haben. Danke auch der Werkstatt und insbesondere Herrn Schwäricke, die unsere elektrische Falle gebaut haben.

Und schliesslich möchte ich noch allen anderen Kollegen danken für die schöne Zeit am Fritz. Zuerst einmal Cyndi, mit der ich unglaublich viel Spass hatte in unserem girls' office, sei es bei einer Englischfrage, beim Diskutieren des Mensaspeiseplans, bei einem Flohmarktbesuch oder beim Planen des Abend- oder Partyprogramms. Es war immer total lustig mit Dir und ich bin sehr froh, dass wir ein Büro geteilt haben. Ich hoffe, wir werden irgendwann doch noch zusammen auf Weltreise gehen!

Ein grosses Dankeschön an Henrik, mit dem wir unser Experiment auf langen Mensaspaziergängen diskutiert haben und der bei technischen Fragen oft geholfen und auch immer neue Ideen geliefert hat.

Then I want to thank Amudha for taking over my experiment and making sure it keeps on running. Keep an eye on it!

Und dann vielen Dank an alle in der Abteilung, die mich bei der Arbeit unterstützt haben, allen voran Inga, Christa und Bea, die immer für mich da waren, vor allem wenn es etwas zu organisieren gab. Im Labor hatten Jürgen, Manfred, Rolf, Sandy, Georg, Uwe Hoppe und Wolfgang immer ein offenes Ohr für meine Wünsche.

Danke all den anderen Mädels in unserer Abteilung: Jacqueline, Kirstin, Melanie, Irena, Undine und Frauke, unsere girls' evenings werden natürlich unvergessen bleiben! Und schliesslich Danke an Stolli, Frank, Joop, Steven, Joost, Bas, Rick, Nico, Gert, Sam, Horst, Ludwig, Andreas, Moritz, Fabian, alle Peters, André, Jochen, Bum Suk, Boris Sartakov, Achim Peters und all die anderen, die hier bei uns waren, ich hatte eine wunderschöne Zeit mit Euch allen am Fritz!

Dann möchte ich meinen Freunden in Berlin danken. Natalie, Lena, Friederike, Verena, Melanie und Jakob, es war schön, dass ihr immer dafür gesorgt habt, dass mir abends in Berlin nicht langweilig wird.

Und schliesslich möchte ich mich bei meinen Eltern und bei meiner Familie bedanken, die mich während der ganzen langen Zeit des Studiums und der Doktorarbeit unterstützt haben. Ich möchte mich bei Elke und Luise für unzählige Telefonate und bei Martin und Steffi für unzählige Kaffees am Wochenende bedanken. Danke, dass ihr immer für mich da wart!

Sophie Schlunk
Berlin im März 2008



Abbildung 1: Fotografie der Kaiser-Wilhelm-Institute für Chemie (links, heute Otto-Hahn-Gebäude der FU Berlin) und für physikalische Chemie und Elektrochemie (rechts, heute Fritz-Haber-Institut der Max-Planck-Gesellschaft) um 1913. Im kleineren Gebäude des Kaiser-Wilhelm-Instituts für physikalische Chemie und Elektrochemie ist heute die Molekülphysik untergebracht.

Contents

1	Introduction	1
1.1	Temperature	1
1.2	De Broglie wavelength and quantum degeneracy	2
1.3	Cold atoms	4
1.3.1	Laser cooling	4
1.3.2	Evaporative cooling and Bose-Einstein condensation of atoms	5
1.3.3	Further developments in the field of ultracold atoms	6
1.4	Cold molecules	7
1.4.1	Association of ultracold atoms	7
1.4.2	Direct cooling methods for molecules	8
1.5	Towards sympathetic cooling of molecules	11
1.5.1	Traps	11
1.5.2	Cold collisions	13
1.5.3	Sympathetic cooling	13
1.6	This thesis	14
1.7	Outline	16
2	Theoretical basics and experimental methods	17
2.1	Magnetic trapping	17
2.1.1	Hyperfine splitting in an external magnetic field	17
2.1.2	Trapping principles	18
2.1.3	Density in a quadrupole trap	18
2.1.4	Majorana transitions	19
2.2	Laser cooling	19
2.2.1	Atoms in light fields	20
2.2.2	Doppler cooling and optical molasses	21
2.2.3	Magneto-optical trap (MOT)	23
2.2.4	Density distribution in the trap	25
2.2.5	Zeeman slower	27
2.3	Trapping by ac electric fields	30
2.3.1	Interaction with electric fields	30

2.3.2	Trapping principles	31
2.3.3	Equations of motion in an ac trap	33
3	Experimental apparatus for cold atoms	37
3.1	Atomic properties of rubidium	37
3.1.1	Transitions and properties of ^{87}Rb	37
3.1.2	Zeeman effect of ^{87}Rb	40
3.1.3	Stark effect of ^{87}Rb	41
3.2	Laser system	42
3.2.1	Laser locks	42
3.2.2	Laser beam generation	48
3.3	Vacuum system	51
3.3.1	Rubidium oven and source chamber	52
3.3.2	MOT chamber and ac trap chamber	53
3.4	Magnetic field generation	55
3.4.1	Zeeman slower	55
3.4.2	Quadrupole trap and electronic setup	58
3.5	Evaporation	60
3.6	Imaging	62
3.6.1	Absorption imaging principle	62
3.6.2	Imaging setup	64
3.6.3	Temperature of the atom cloud	65
3.7	Computer control	66
4	Preparation of the cold atom cloud	69
4.1	General sequence	69
4.2	The six-beam MOT loaded from the Zeeman slower	71
4.2.1	Compressed MOT (CMOT)	72
4.2.2	Optical molasses	72
4.3	Magnetic trap and transport	72
4.3.1	Optical pumping	72
4.3.2	Quadrupole magnetic trap	74
4.3.3	Evaporation	75
4.3.4	Transfer of the trapped cloud	75
4.4	Imaging	76
4.5	Characteristics of the cold atom cloud	77
4.5.1	Temperature	77
4.5.2	Lifetime of the magnetic trap	78
5	An ac trap for rubidium	81
5.1	Introduction	81
5.2	AC trap setup	82
5.2.1	Electrode geometry and electronic setup of the ac trap	82
5.2.2	Electric fields in the ac trap	84

5.3	Trajectory calculations	86
5.4	Experimental procedure	86
5.5	Mapping of the electric fields	87
5.6	Loading the atoms in the ac trap	91
5.7	Performance of the ac trap	93
5.8	Probing the phase space acceptance of the trap	97
5.9	Time-of-flight measurements	100
5.10	Prospects for sympathetic cooling	102
5.11	Conclusions	103
Bibliography		105
6	Samenvatting	117
6.1	Een elektrische wisselspanningsval	118
6.2	Experiment	119
7	Summary	123
7.1	Principle of ac electric trapping	124
7.2	Experiment	124
Appendix		127
Curriculum Vitae		131

Chapter 1

Introduction

Ever since physics was revolutionized by the invention of quantum mechanics physicists have become more and more interested in cold matter, because the quantum behavior of particles becomes apparent at low temperatures. In particular since the invention of the laser as a source of coherent light in 1960 [1, 2], tremendous scientific and technical progress has occurred in atomic and molecular physics. It became thus possible to cool particles to much lower temperatures than ever before.

1.1 Temperature

To understand why physicists are interested in low temperatures we should first ask ourselves ‘what do we mean by temperature’? The temperatures we are used to in daily life are between $-20\text{ }^{\circ}\text{C}$, which is the outside temperature on a cold day, and $100\text{ }^{\circ}\text{C}$, which is the boiling point of water. In physics, however, the temperature in gases is directly related to the mean velocity of the gas particles. At room temperature, for instance, the gas particles in the air move randomly in all directions at quite large velocities \mathbf{v} , i.e., several hundreds of meters per second. In fact, the air temperature as we feel it is due to these fast particles hitting our skin.

Physicists measure the temperature on the Kelvin (or absolute) scale. In this concept, a lowest possible temperature is postulated at zero Kelvin, i.e., $-273.15\text{ }^{\circ}\text{C}$. The absolute temperature T is proportional to the average velocity square $\langle v^2 \rangle$:

$$T \propto \langle v^2 \rangle / k_{\text{B}}, \quad (1.1)$$

where k_{B} is the Boltzmann constant. This implies that at zero Kelvin all particles in a sample are at rest.

A temperature, however, is only defined for systems that are in thermal equilibrium. For an ideal gas, the kinetic energy distribution of an ensemble of

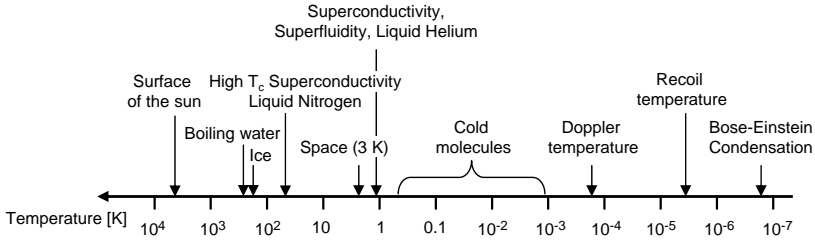


Figure 1.1: The temperature scale in Kelvin.

particles with mass m is given by the Maxwell-Boltzmann velocity distribution which describes the probability $f(v)$ to find a particle at a certain speed $|\mathbf{v}| = v$

$$f(v) \propto v^2 e^{-mv^2/2k_B T}. \quad (1.2)$$

More generally, the energy distribution of a gas in thermal equilibrium at a temperature T can be described by the Boltzmann distribution which reads

$$\tilde{f}(E) \propto g(E) e^{-E/k_B T}. \quad (1.3)$$

Here, $g(E)$ is the density of states at the energy E . Note that the energy E is the total energy, i.e., it includes the kinetic energy, the potential energy, the rotational and the vibrational energy of a particle.

Figure 1.1 shows a logarithmic scale of the absolute temperatures that are important in physics. The scale covers 11 orders of magnitude starting at the surface temperature of the sun which is around 6000 K down to 100 nK which is a typical temperature of a Bose-Einstein condensate (BEC). The boiling point of nitrogen is at 77 K, i.e., -196°C , and its freezing point is found at 63 K, i.e., -210°C . This is also the regime of ‘high-temperature superconductivity’. Close to the temperature of liquid helium, the phenomena of superfluidity and superconductivity are present. Thanks to the advances in the field of cold atoms and molecules over the last 40 years, particles have been brought to much colder temperatures. Cold molecules are mostly produced in the millikelvin range, while ultracold atoms can be brought to the nanokelvin range (BEC). At these ultralow temperatures particles barely move, for instance a rubidium atom that has an average speed of 300 m/s at room temperature only moves at 5 mm/s after being cooled to 100 nK.

1.2 De Broglie wavelength and quantum degeneracy

Let us come back to the question why physicists are so interested in low temperatures. As we have just learned, particles in the gas phase move very fast.

Experiments with fast moving particles inherently entail difficulties. Doppler shifts arise due to the high speeds and may broaden the spectral lines. Moreover, high velocities imply short observation times that result in a limited spectral resolution. As mentioned above, there is another interesting characteristic of cold matter which has attracted a lot of attention lately: at low temperatures the quantum nature of the particles starts to play an important role.

To understand this point we should take a short trip through the history of physics in the early years of the 20th century. When Einstein explained the photoelectric effect in 1905, he proposed the revolutionary idea that light, in spite of the evidence for its wave-like behavior, can behave like a particle. This idea was challenging the electromagnetic wave theory of light which was well-established at the time. For a long time, his new theory was not accepted by leading scientists. Even in 1913 when Einstein was nominated to become a member of the *Preußische Akademie der Wissenschaften*, Max Planck apologized for him by saying ‘that he [sometimes] might have overshot his target in his speculations, as for example in his light quantum hypothesis.’ [3].

In 1923, Louis de Broglie proposed an analogous principle for particles by postulating that particles can also behave like waves. In his concept, he associated a wavelength λ to the momentum p of the particle $\lambda_{\text{dB}} = h/p$, where h is Planck’s constant. This implies that at ultralow temperatures where a particle carries a very small momentum, the so-called de Broglie wavelength becomes large, even comparable to the wavelength of visible light. Therefore a wave-like behavior emerges at low temperatures. These signatures of their quantum nature can change the interactions of the particles, and thus pose interesting questions in both theory and experiment.

Of course, one of the most ambitious goals was to create a Bose-Einstein condensate (BEC) that promised to have intriguing properties. The existence of a BEC had already been proposed in 1924 when Satyendranath Bose suggested a new kind of statistics for photons, based on particle indistinguishability, in order to explain the black-body radiation [4]. Albert Einstein foresaw the consequences for a real gas of particles and derived what is nowadays known as Bose-Einstein statistics for particles that are indistinguishable and have integer spin, the so-called bosons [5, 6]. This statistics predicts that at low temperatures all particles can accumulate in the lowest energy quantum state. Then, the de Broglie wavelengths λ_{dB} of the particles become comparable to the distance between them, the wave packets start to overlap, and the physical properties of the particles can be described by a single wave function. To reach the phase transition to quantum degeneracy the phase space density, i.e., the product of the peak particle density and the de Broglie wavelength cubed, needs to be on the order of one¹. For a long time it seemed impossible from a technical point of view to reach the high densities and low temperatures

¹The exact equation reads $n \lambda_{\text{dB}}^3 \geq 2.612$.

required. The advent of laser cooling of atoms in the 1980s brought these goals into the realm of possibility. Nevertheless, it took until 1995 until the Bose-Einstein condensation of bosonic alkali atoms was demonstrated for the first time [7–9], which was awarded with the Nobel prize in 2001.

Quantum-degenerate molecules might conceal even richer physics because they can possess a permanent electric dipole moment which, in turn, gives rise to long-range dipole-dipole interactions. These interactions can affect the dynamics in a BEC considerably [10, 11]. Bringing (polar) molecules close to quantum degeneracy, however, is difficult, as the complicated molecular level structure precludes a simple extension of laser cooling to molecules. The multitude of vibrational and rotational levels give rise to loss channels when the molecules are repeatedly excited. Therefore, a number of alternative methods are used for cooling molecules. In the next sections, a brief summary of the developments in the fields of both cold atoms and cold molecules will be given.

1.3 Cold atoms

1.3.1 Laser cooling

Although the concept of light pressure was already established at the beginning of the 20th century, it took until the 1970s for its potential as a substantial friction force to be recognized. When narrow-linewidth tunable lasers became available, the idea of laser cooling, i.e., the reduction of thermal velocities using the scattering force of light, came about. This was proposed in 1975 in two independent papers by Hänsch and Schawlow [12], and Wineland and Dehmelt [13]. In 1978, Ashkin suggested to use a laser tuned to the atomic resonance to slow down an atomic beam of sodium. The first laser cooling experiment was reported in 1978 [14] when a cloud of magnesium ions confined in a Penning trap was laser cooled. At the same time, a similar experiment with barium ions was published [15]. Compared to ions, however, trapping and cooling of neutral atoms is more difficult. Ion traps can be made sufficiently deep to confine ions even at temperatures higher than room temperature, which is not at all possible for neutral particles.

It took more than ten years until significant experimental progress was made. A thermal beam of sodium atoms was decelerated in 1982 by Phillips and Metcalf [16]. The first 3D cooling using the radiation pressure of counter-propagating beams was achieved in 1983 by Ashkin and coworkers [17], also for sodium atoms. The same group reported optical trapping of sodium atoms in 1986 [18]. The temperatures obtained in these early experiments were in agreement with the so-called Doppler limit, i.e., temperatures around 200 μK for the alkalis. The first demonstration of simultaneous cooling and trapping was carried out by the Pritchard group in 1987 by combining light and magnetic fields [19]. The new device, a so-called magneto-optical trap or MOT, turned

out to be one of the most successful tools in the field of cold atoms. Essentially every cold atom experiment nowadays is based on a pre-cooling stage in a MOT, before further cooling stages are applied. A typical MOT contains up to 10^{10} atoms, has a density of up to 10^{11}cm^{-3} and a temperature on the order of $10\text{--}500\text{ }\mu\text{K}$. Another very important and puzzling circumstance was discovered in 1988. It was found that the temperatures achieved in optical molasses could, in fact, be much lower than the expected Doppler temperatures [20]. With the densities achieved in the MOT and these low temperatures measured in optical molasses, the realization of a Bose-Einstein condensate, the holy grail of atomic physics, no longer seemed so remote.

1.3.2 Evaporative cooling and Bose-Einstein condensation of atoms

Within a few years, the theory of laser cooling was understood much better. It became clear that the unexpected low molasses temperatures originate from a combination of light shifts and optical pumping, and that in general the MOT temperature is limited by momentum fluctuations of randomly rescattered photons [21]. These scattered photons also give rise to radiation pressure which in turn limits the density [22]. Hence to further cool atoms, alternative cooling methods were required. One of the most promising techniques at the time was evaporative cooling of trapped atoms [23]. The principle of evaporative cooling is simple. A trapped sample of particles at sufficiently high densities is thermalized with a Boltzmann energy distribution, as seen in Eq. 1.3. If the hottest atoms of the sample are forced to leave the trap, the remaining atoms will rethermalize via elastic collisions. Since the ejected atoms carry away more than the average kinetic energy, the removal leads to a decrease of the temperature in the trap. At that time, hydrogen was thought to be one of the most promising candidates for a BEC, and evaporative cooling was demonstrated in different groups working on hydrogen. In the MIT hydrogen group, a temperature of $100\text{ }\mu\text{K}$ was achieved after evaporative cooling [24], but condensation was not reached¹. Other promising candidates seemed to be the alkali atoms (mostly sodium or rubidium) which could be precooled in a MOT.

Two forced-evaporative cooling techniques were most appealing for condensing alkali atoms. In the first method, the atoms were kept in a magnetic trap while a radio frequency (rf) was applied to selectively transfer hot atoms into an untrapped Zeeman sublevel². Evaporative cooling using rf radiation had been proposed by Pritchard [27]. The other method employed a dipole trap whose potential was lowered by reducing the intensity of the laser. Finally, the 70-year-old dream became true in 1995 when the first Bose-Einstein conden-

¹Condensation of hydrogen was finally achieved in 1998 [25], three years after the demonstration of the alkali BECs

²Magnetic trapping of atoms had already been obtained for sodium in 1985 [26] by Metcalf and coworkers.

sates were created using the first evaporation method [7, 8, 28]. Nowadays, the preparation of a Bose-Einstein condensate is almost routine in ultracold atom labs all over the world, and quantum degeneracy has been reached for a number of different atoms and homonuclear molecules¹.

1.3.3 Further developments in the field of ultracold atoms

Since the first experimental realization of a Bose-Einstein condensate the field of ultracold atoms has grown explosively. One of the first major applications was the development of an atom laser, an intense beam of coherent atoms [29, 30]. Loading BECs into optical lattices also attracted a lot of interest, because the lattice depth and thus the amount of tunnelling between neighboring sites can be controlled accurately. In this way it was possible to convert a weakly interacting Bose gas into a Mott insulator [31]. Moreover, 1D and 2D optical lattices can be used to prepare quantum degenerate gases in lower dimensional systems.

Feshbach resonances are another interesting tool because the interparticle interactions can be increased by resonantly enhancing the scattering length. In bosonic systems the strongly interacting regime cannot be reached due to the rapid three-body decay. For Fermi gases, however, losses are suppressed due to the Pauli exclusion principle. Studying fermions is especially interesting because systems of interacting fermions play an important role in many areas of physics, e.g., superconductivity in condensed matter physics. Moreover, they can pair up to form composite bosons. In 2003, the JILA group demonstrated the first molecule formation in an ultracold Fermi gas of ^{40}K [32]. In late 2003 the first observation of a molecular BEC was reported by three groups, the JILA group using ^{40}K [33] and the Grimm group and the MIT group using fermionic ^6Li [34, 35]. A number of follow-up experiments concentrated on exploring the so-called BEC-BCS crossover; it was possible to smoothly cross over from a BEC-type system of tightly bound molecules to a fermionic superfluid with Bardeen-Cooper-Schrieffer (BCS) type pairing. Finally, in 2005 the MIT group directly demonstrated superfluidity in strongly interacting Fermi gases by observing superfluid flow in the form of quantized vortices [36]. More recent experiments started to look into fermionic mixtures with population imbalance [37]. Using optical lattices the periodic environment of crystalline structures can be modelled accurately thus allowing the researchers to explore many interesting questions of condensed matter physics [38]. Bose-Fermi mixtures allow for the study of boson-mediated interactions between fermions [39, 40], as well as the effect of fermions on the bosonic superfluid-to-Mott-insulator transition [41, 42]. Fermi-Fermi mixtures also promise rich physics such as pairing and superfluidity of fermion pairs consisting of atoms with different masses [43, 44].

¹Bose-Einstein condensation has so far been reached for the alkalis (lithium, sodium, potassium, rubidium, cesium), as well as for hydrogen, metastable helium, chromium, and ytterbium.

The physics of ultracold fermions and bosons thus promises many more exciting experiments in the next years.

1.4 Cold molecules

As mentioned above, gases of quantum degenerate polar molecules bear even more interesting physics than atoms due to their richer level structure and long-range electric dipole-dipole interactions. Furthermore, cold molecules are suitable candidates for answering fundamental physics questions, as for instance the search for the electric dipole moment [45]. It was also proposed to use trapped polar molecules for quantum computation [46]. Generally, there are two approaches to produce cold molecules: (i) by association of two (or more) ultracold atoms, and (ii) by application of direct cooling methods. The first method is only applicable to molecules consisting of atoms that can be laser cooled, whereas the second approach provides access to a much larger class of molecules. In the following, an overview of the different existing techniques and the current state of research is given.

1.4.1 Association of ultracold atoms

The difficulties linked with direct cooling of molecules can be circumvented by starting with laser-cooled atoms. The subsequent association of the ultracold atoms can be accomplished in two different ways.

Photoassociation of ultracold atoms

Two atoms can form a molecule in an excited state by resonant absorption of a photon. The photoassociated molecules are translationally very cold, but in a highly excited vibrational level thus leading to short lifetimes. To obtain stable molecules, they have to be transferred to a bound level of the ground (or lower triplet) electronic state. This transfer can be achieved by spontaneous or induced emission with another laser. The experimental methods that have been successfully developed for the production of homonuclear molecules [47, 48] were extended to heteronuclear (polar) alkali molecules. In recent years, different heteronuclear molecules have therefore been created via photoassociation, i.e., RbCs [49], NaCs [50], KRb [51, 52]. Recently, the formation of LiCs molecules induced by the MOT cooling light has been reported, where no additional photoassociation laser is required [53]. After being produced, the molecules can be transferred to the ground state, as has recently been demonstrated for photoassociated RbCs molecules. In this experiment, a laser-stimulated transfer process was used to bring the polar molecules into their vibronic ground state [54].

Association of ultracold atoms via Feshbach resonances

It is also possible to transfer two ultracold atoms (either close to degeneracy or Bose condensed) into a molecular state using a Feshbach resonance. This has been demonstrated for the first time in 2003 [33–35, 55]. A Feshbach resonance is a magnetically tunable scattering resonance where two (unbound) colliding atoms couple to a molecular bound state. Since the magnetic moments of the atomic and the molecular states are different, their energies can be matched by applying an external magnetic field. At ultralow temperatures, the properties of a collision can be completely described by the s-wave scattering length which diverges at the Feshbach resonance. At the same time, the cross section for elastic collisions increases significantly and inelastic collisions (three-body recombination) are also enhanced. The Zeeman energies of the atomic and molecular state intersect at the resonance, giving rise to an avoided crossing. Molecules can be created in two different ways. Firstly, the magnetic field can be set close to the resonance value thereby enhancing the three-body recombination rate, where at sufficiently high densities molecules are formed. Secondly, by slowly sweeping the magnetic field across the avoided crossing at the resonance, two atoms can be adiabatically transferred into a molecular state [56]. In both cases, however, the molecules are created in a highly excited vibrational state.

1.4.2 Direct cooling methods for molecules

In recent years, a number of different cooling methods for molecules have been developed. Direct cooling of molecules has the advantage that the methods are applicable to a whole class of molecules, i.e., paramagnetic molecules (magnetic trapping of buffer-gas-cooled molecules) or polar molecules (Stark deceleration). Another advantage is that the molecules are mostly in low vibrational states and thus internally very cold. However, the phase space densities achieved to date are still far too low to reach quantum degeneracy.

Buffer-gas cooling

The concept of buffer-gas cooling is simple and in principle applicable to any molecule (or atom). The molecules to be cooled are brought into a cryogenic cell filled with a very cold buffer gas, usually helium. The two species thermalize via elastic collisions, and the final temperature is determined by the equilibrium vapor pressure of the buffer gas. The molecules have to reach thermal equilibrium before they collide with the walls of the cryogenic cell and are lost from the experiment. Therefore, a relatively high density of the buffer gas is required. Typical temperatures are on the order of 300 mK for ^3He and 800 mK for ^4He , respectively. The technique was pioneered by the Doyle group [57, 58]. With this technique a number of paramagnetic species have been cooled to millikelvin temperatures and have subsequently been loaded into a

magnetic trap¹ [66]. One difficulty of buffer-gas cooling is to insert the species of interest into the cell. The number of species is so far limited to those where the techniques of either laser ablation of a solid precursor or capillary filling are applicable. Recently, it was proposed to attach a molecular beam to the cell [67] which was demonstrated with a pulsed beam of NH radicals [64, 68]. At sufficiently high densities, it should be possible to perform evaporative cooling in a magnetic trap, as already shown for buffer-gas-cooled atoms [69].

Stark deceleration of molecules

A beam of polar molecules in selected quantum states can be decelerated by applying time-varying inhomogeneous electric fields. The method exploits the fact that the molecules are first adiabatically cooled during a supersonic expansion through a nozzle into vacuum. These molecules are already very cold in the moving frame of the beam, however in the laboratory frame they are travelling at a velocity of hundreds of meters per second. The molecules then pass through the Stark decelerator consisting of an array of electric field stages. If the dipole moment of the molecules is aligned anti-parallel with respect to the Stark decelerator fields, i.e., the molecules are in a ‘low-field-seeking state’, they are attracted to the regions of low field. When the molecules enter a region of higher field they will lose kinetic energy. The electric fields in the Stark decelerator are switched such that the molecules are still in a region of high field, therefore the kinetic energy can not be regained. In this way, the molecules are decelerated at each stage, resulting in a slow packet of molecules at the end of the decelerator. A Stark decelerated beam can be continuously tuned to an arbitrarily low laboratory velocity. This technique has been demonstrated for the first time by the Meijer group in 1999 [70].

A number of experiments have been carried out with Stark decelerated cold molecules [71, 72], namely metastable CO [70], different isotopomers of ammonia [73, 74], OH radicals [75, 76], formaldehyde [77], metastable NH radicals [78], and SO₂ [79]. Stark-decelerated molecules have also been loaded into different types of traps which will be discussed in Sec. 1.5.1. Moreover, they have been stored in both an electrostatic ring [80, 81] and a molecular synchrotron; within the latter device the molecules are repeatedly bunched together in a tight packet as they revolve around the ring [82]. The methods developed to decelerate molecules in low-field-seeking states have also been extended to molecules in high-field-seeking states. In this case, the molecules are flying out of (instead of into) regions of a high electric field. Using the so-called alternate gradient (AG) focusing method, deceleration has been demonstrated for CO [83] and OH [84], as well as for the heavy polar molecules YbF [85], CaF [86], and benzonitrile [87].

¹So far buffer-gas cooling of europium [58], chromium [59, 60], and a number of other atoms [61, 62] has been published. Furthermore, the molecules calcium monohydride [63], NH [64], chromium hydride [65], and manganese hydride [65] have been cooled and trapped.

The slowing process can also be performed using magnetic or optical analogues of a Stark decelerator. In the latter case, a high-intensity pulsed optical lattice is used to decelerate the molecules [88, 89]. Two counterpropagating beams far detuned from resonance are used to generate the lattice whose velocity can be changed by offsetting the frequency in one of the beams. In this way, cold molecules generated in a supersonic beam can be bunched and decelerated to the desired final velocity. Optical Stark deceleration has been demonstrated for benzene [90] and nitric oxide [91, 92].

The magnetic analogue of the Stark decelerator has been demonstrated only recently [93, 94]. In a proof-of-principle experiment, ground-state hydrogen atoms were decelerated using six pulsed magnetic field stages. Fast switching of the magnetic fields in such a slower is difficult due to the voltages induced in the coils. Recently, the method has also been demonstrated for metastable neon atoms [95]. In principle, this technique can be used to decelerate and trap all neutral particles that possess an electronic spin.

Other cooling techniques

Over the last 10 years a number of other cooling techniques for molecules have been developed [96]. Molecules can be decelerated by billiard-like collisions in a crossed molecular beam setup. A single collision between the molecule of interest and a particle from the second beam can bring the molecule to a laboratory velocity that is nominally zero. The scattering distribution is then characterized using velocity mapped ion imaging. This technique was first demonstrated by the Chandler group in 2003, when nitric oxide was cooled to temperatures of about 400 mK [97].

A second technique is based on mechanical cooling using a counter-rotating nozzle [98, 99] that spins at the speed needed to compensate for the velocity of the molecular beam. In this way, Gupta and Herschbach produced slow beams of methyl fluoride, oxygen, and sulfur hexafluoride at speeds of 50-100 m/s .

Another technique employs a guide to perform velocity filtering of a thermal molecular beam [100]. This technique was introduced by the Rempe group and exploits the fact that in a thermal beam a small fraction of the Maxwell-Boltzmann distribution is already very cold. An electrostatic quadrupole with a curved section is used as a guide selecting the molecules with small transverse and longitudinal velocities. Using this technique, filtering of the cold fraction has been demonstrated in formaldehyde and in deuterated ammonia, followed by two-dimensional trapping of the velocity-filtered ammonia molecules [101]. A number of other molecules have been successfully guided in the Softley group. Although the method is relatively easy to implement and can in principle be applied to a large number of molecules, it has the disadvantage that the selected molecules are distributed over different vibrational and rotational levels.

1.5 Towards sympathetic cooling of molecules

Cooling of molecules through elastic collisions with ultracold atoms has been discussed as a promising approach to bring molecules closer to quantum degeneracy. This form of collisional cooling is called sympathetic cooling and has been successfully demonstrated for atoms [102]. It does not rely on specific transitions and can therefore also be applied to molecules. The experimental setup presented in this work has been designed with the aim to produce ultracold molecules via sympathetic cooling. If the ratio of the elastic to inelastic atom-molecule collision rates is sufficiently large, a trapped cloud of ultracold atoms can be used as a coolant and lower the temperature of the molecules towards the ultracold regime. Because both atoms and molecules need to be trapped, a brief review of the traps most commonly used in the cold atom and cold molecule community will first be given. Thereafter, the topic of collisions at low temperatures will be introduced and finally the prospects of sympathetic cooling of molecules will be discussed.

1.5.1 Traps

Trapping of charged and neutral particles has proven tremendously successful for the study of their properties and interactions. To confine particles in a trap, a restoring force towards the center is needed, which can be accomplished by using the interaction energy of the particle with either a magnetic field (Zeeman effect) or an electric field (Stark effect). For particles in states whose energy increases with increasing field strength, it is energetically favorable to be in a lower field and they are therefore driven to the field minima. These particles are in so-called low-field-seeking states, while particles in states whose energy decreases with increasing field are attracted to higher fields and are thus in high-field-seeking states.

Traps for low-field seekers

Particles in low-field-seeking quantum states can be trapped in a minimum of a static field. This was already demonstrated in 1978 for neutrons using a magnetic trap [103]. Magnetic trapping of neutral atoms was accomplished in 1985, when laser-cooled atoms were stored in a quadrupole trap [26]. Using buffer-gas cooling, it was also possible to trap molecules in magnetic traps [63].

Electrostatic traps exploit the Stark interaction of the particle with the electric field. Electrostatic trapping has been first demonstrated for polar molecules in 2000 [73], when Stark-decelerated ammonia molecules were confined in a quadrupole trap. Further experiments succeeded in the trapping of OH [76] and metastable NH radicals [78], as well as metastable CO molecules [104].

Traps for high-field seekers

Particles in a high-field-seeking quantum state cannot be confined in a static field, as static fields cannot possess a maximum in free space [105, 106]. High-field-seeking states can be confined, however, when electrodynamic fields are used.

Optical dipole traps, for instance, have found widespread application in ultracold atom experiments [107]. Here, the interaction of the particle with far-off resonant laser light gives rise to an energy shift. For red-detuned laser light, the light field is attractive and thus the potential minima are at the intensity maxima, while for blue-detuned light the light field is repulsive and the atoms are stored at locations with minimal intensity. Both atoms [18] and molecules [108] have been successfully confined in optical traps.

It is also possible to trap particles in a microwave trap. This has been achieved for cesium atoms in 1994 [109], and recently trapping of polar molecules in such a trap has also been proposed [110]. Paramagnetic ground-state atoms and molecules can be trapped with ac magnetic fields, as has been proven for cesium atoms [111].

Another quite versatile way of trapping (charged and neutral) particles in a large volume is to make use of ac electric fields. Wolfgang Paul was the first to propose such a trap for charged particles. The trap was a further development of the quadrupole mass filter and employs dc and radio frequency ac fields. In 1989 he received the Nobel prize for his invention, the Paul trap for ions [112].

To date, several different ac electric trap configurations for neutral particles have also been proposed [113–115]. The operation principle of an ac electric trap for neutral particles is analogous to that of the Paul trap for ions; a potential energy surface is created with a saddle point at the trap center, resulting in attractive forces (focusing) in one direction and repulsive forces (defocusing) along the other two directions. The electric field configuration is then switched to a second one in which the roles of the forces are reversed. Alternating between these two configurations at the appropriate frequency, using either a sine wave or a square wave, leads to dynamic confinement of the particles.

Trapping with ac electric fields is particularly appealing for polar molecules that show a first-order Stark effect and that can therefore be strongly confined. For ground-state ammonia molecules, ac electric traps with a depth of several millikelvins have been demonstrated [116, 117], and the motion of the trapped molecules has been analyzed in detail [118]. In addition, any ground-state atom or nonpolar molecule can be confined in an ac electric trap via their induced dipole moment. This includes species that are hard to trap otherwise, e.g., singlet homonuclear diatomics. The second-order Stark interaction leads to shallower traps, but has the advantage that all ground-state sublevels can be trapped.

Trapping of rubidium atoms in a macroscopic ac electric trap was first demonstrated in this PhD project [119] and is discussed in chapter 5 of this

thesis. Recently, rubidium atoms were also confined in a three-phase ac electric trap [120]. In 2006, Katori and coworkers achieved trapping of about 100 ground-state Sr atoms in a microstructured ac electric trap on a chip [121].

1.5.2 Cold collisions

At ultralow temperatures, the range of the interparticle forces extends over a large distance due to their long de Broglie wavelength. Also, the collision partners have a longer interaction time, thus significantly altering the collisional characteristics compared to those of high-temperature collisions.

Already for ultracold atoms, the collisional behavior turned out to be crucial to reach degeneracy, as the ratio of elastic to inelastic collisions determines the efficiency of evaporative cooling. The mean field theory, in which the atom interaction energy is described with the s-wave scattering length, proved tremendously successful. The stability and properties of a condensate depend on both the sign and magnitude of the scattering length. As discussed in Sec. 1.4.1, the scattering length can be modified by an external field, thereby changing the inelastic collision rates.

For molecules, additional interactions due to the dipole-dipole force come into play. The characterization of the elastic and inelastic collision rates is thus of great interest, as their ratio is crucial for evaporation or sympathetic cooling. Moreover, the study of cold collisions is an interesting topic in itself. Recently, a Stark-decelerated beam of cold OH radicals with a narrow velocity distribution was collided with a beam of Xe atoms, and the inelastic collision rate was measured as a function of the OH beam velocity [122]. For molecule-molecule as well as for most atom-molecule collisions it is difficult to theoretically predict the corresponding low-temperature cross sections because of uncertainties in the best-known interaction potentials.

1.5.3 Sympathetic cooling

Sympathetic cooling has already been demonstrated with trapped ions [123] and ultracold atoms [102]. For molecules, sympathetic cooling using ultracold atoms is also considered to be one of the most promising approaches to bring molecules closer to quantum degeneracy. To successfully apply it, however, the ratio of elastic to inelastic collisions has to be large, because inelastic collisions can transfer the molecules to untrapped states thus resulting in trap loss.

A number of theoretical studies of molecule collisions with helium have been carried out [124, 125]. Recently, first calculations of the elastic and inelastic cross sections for collisions between rubidium and OH have been published, where the prospects of sympathetic cooling between the two species were also examined [126, 127]. One of the difficulties associated with sympathetic cooling is the number of inelastic collision channels that open up if the molecule resides

in an upper state. To avoid these losses, the molecules and the atoms need to be in their ground state [127].

Therefore, it might be necessary to confine the ground-state atoms and molecules either simultaneously in the same trap or in two overlaid independent traps. Molecules and atoms in their lowest-energy quantum level, however, are always high-field seeking. Hence, as previously discussed, it is not possible to confine them in static electric or magnetic fields; electrodynamic fields have to be used instead.

An appealing method would be to simultaneously confine the ground-state atoms and molecules in the same ac trap. However, polarizable atoms cannot be trapped at the same ac frequencies as polar molecules because of the largely different Stark interaction strengths. Thus, a trap for polar molecules has to be spatially overlapped with a different kind of atomic trap, i.e., a magnetic trap or a dipole trap. Moreover, these traps should not perturb each other. The compatibility of these traps is an important prerequisite for sympathetic cooling of molecules using magnetically trapped ultracold atoms.

To decrease the temperature of the molecules by an order of magnitude, one needs approximately 12 elastic atom-molecule collisions [128]. In principle it should be possible to cool without losing molecules; a tenfold decrease in temperature leads to an increase in phase space density by a factor of 1000. With an initial phase space density on the order of 10^{-12} for the molecules, which is a typical value in a molecule trap, one can reach quantum degeneracy with only 50 atom-molecule collisions.

1.6 This thesis

The experimental setup presented in this work has been designed with the aim to produce ultracold molecules via sympathetic cooling with laser-cooled rubidium atoms. As discussed in Sec. 1.5.3, both the atoms and the molecules should be trapped in their ground state to prevent inelastic collisions. For this purpose, a trap confining the ultracold atoms needs to be spatially overlapped with a trap for ground-state polar molecules. In our experimental approach the molecules will be slowed by Stark deceleration and subsequently trapped. Trapping and cooling of the rubidium atoms is performed in a standard magneto-optical trap before the atoms are transferred into a magnetic trap. Merging the atomic and molecular traps should reveal the effects of cold atom-molecule collisions.

Combining two such different systems is difficult and a large number of requirements has to be fulfilled. Firstly, the number of atoms should be as high as possible, because the number of collisions increases linearly with the density. Densities in a MOT are limited to about 10^{10} atoms/cm³ which might not be sufficient for efficient collision rates. Therefore, the atoms are transferred into a magnetic trap where they can be compressed to higher densities. Secondly, the optical access in the MOT is limited due to the presence of the six cooling

laser beams, the optical pumping beam, the detection beam, and the optics for detection. Moreover, to perform sympathetic cooling, the atom trap and a second trap for the molecules need to be spatially overlapped. Therefore, it is advantageous to transfer the magnetically trapped cloud to a second vacuum chamber allowing for better optical access and implementation of the molecule trap. Additionally, very good vacuum is required because the lifetime and the number of atoms quickly decrease with higher pressure thus affecting the collision rates. A Stark-decelerated molecular beam, however, is a constant source of background gas. Also for this reason, a second vacuum chamber is beneficial because it is possible to connect it to pumps with sufficiently high pumping speed to ensure good vacuum conditions. Also, differential pumping stages are needed for both the atom setup and the Stark decelerator. For the former setup, a differential pumping stage can easily be implemented between the MOT chamber and the second chamber. For a decelerated beam this is more difficult as the deceleration stages extend from the beam source to the end of the machine where the molecules are detected. Furthermore, the molecule trap needs to be as close as possible to the last deceleration stage, as the beam spreads out in free flight thus lowering the density.

We decided to work with ^{87}Rb which has the advantage that it is the best-studied alkali atom in the ultracold atom community. Moreover, the required transitions can be conveniently accessed with commercially available diode lasers that are also easy to maintain. We decided to load the MOT using a Zeeman slower which has high loading rates compared to alternative loading schemes. To transfer the magnetically trapped atom cloud, we use a translation stage which was already successfully demonstrated in other groups [129]. A significant part of this PhD research project was dedicated to designing and constructing the complete setup for the cold rubidium experiment.

Within the framework of this thesis it was not possible to also build up a setup for a molecular beam and a molecular trap incorporating the technical specifications discussed above. Therefore, we decided to first transport the magnetically trapped atoms to a second location where the magnetic trap was spatially overlapped with an ac electric trap. Using this setup, we were able to successfully demonstrate trapping of rubidium atoms in a macroscopic ac electric trap for the first time [119]. Moreover, we directly visualized the dynamic confinement of the rubidium atoms at different phases of the ac switching cycle using absorption imaging. Additionally, we were able to explore how rubidium atoms that are confined in the magnetic trap are perturbed by the ac electric fields. We thus examined the compatibility of two different trap types, namely a magnetic and an ac electric trap, which is an important prerequisite for sympathetic cooling of molecules using magnetically trapped ultracold atoms.

1.7 Outline

This thesis is organized as follows. First, the theoretical background of laser cooling, magnetic trapping, and trapping with ac electric fields is given in chapter 2. In chapter 3, the reader will find a description of the experimental setup, i.e., the preparation of the laser frequencies, the vacuum system, and the optics used to generate all the necessary laser beams. In chapter 4, the series of experimental stages applied in the experiment is described in detail. Finally, in chapter 5 the experimental results on trapping of rubidium atoms in the ac electric trap are discussed in detail, both experimentally and theoretically.

Chapter 2

Theoretical basics and experimental methods

2.1 Magnetic trapping

2.1.1 Hyperfine splitting in an external magnetic field

The interaction of an atom with an external magnetic field depends on the magnetic moment of the atom and therefore on the electronic level structure. The atomic *fine structure* is characterized by the total electronic angular momentum $\mathbf{J} = \mathbf{L} + \mathbf{S}$ (here only Russel-Saunders coupling is considered), which results from the coupling of the orbital angular momentum \mathbf{L} to the spin angular momentum \mathbf{S} . The *hyperfine structure* originates from the coupling of the total electron angular momentum \mathbf{J} to the total nuclear spin \mathbf{I} :

$$\mathbf{F} = \mathbf{J} + \mathbf{I}. \quad (2.1)$$

Each of the hyperfine levels contains $2F + 1$ magnetic sublevels, which are degenerate in the absence of an external magnetic field \mathbf{B} . When a magnetic field is present, this degeneracy is lifted and the potential energy is given by the scalar product of the atomic dipole moment $\boldsymbol{\mu}$ and the external field. Therefore, $E_{\text{pot}} = -\boldsymbol{\mu}\mathbf{B}$ depends on the orientation of the dipole moment relative to the magnetic field. For low magnetic fields, i.e., when the energy shift due to the external field is small compared to the hyperfine splitting, F is a good quantum number. The magnetic dipole moment of the atom is then given by $|\boldsymbol{\mu}| = m_F g_F \mu_B$. The quantum number m_F is the projection of the angular momentum F onto the quantization axis (usually chosen along the axis of the magnetic field), g_F the Landé g-factor, and $\mu_B = \frac{e\hbar}{2m_e}$ is the Bohr magneton, where e is the electron charge and m_e the rest mass of the electron. Hence, the

Zeeman shift of an atomic level in small magnetic fields is given by

$$E_{\text{Zeeman}} = m_F g_F \mu_B B. \quad (2.2)$$

For the case of rubidium the actual Zeeman energies are plotted in Fig. 3.2.

2.1.2 Trapping principles

The interaction of the atomic magnetic moment with an external inhomogeneous field can be used to confine atoms in the resulting potential. Magnetic trapping was first achieved in 1985 [26], actually before the first magneto-optical trap was demonstrated. Na atoms were loaded from a laser-cooled atom beam and confined in a quadrupole trap.

As seen from Eq. 2.2 the energy of a magnetic sublevel for a given magnetic field B depends on the product $m_F g_F$. For atoms with $m_F g_F > 0$, the energy is increasing with increasing field, and they will feel a force towards smaller fields. Atoms with $m_F g_F < 0$, however, will be driven towards higher fields. Therefore, atoms with $m_F g_F > 0$ are called *low-field seekers*, and atoms with $m_F g_F < 0$ are called *high-field seekers*. The divergence of a magnetic field is always zero ($\nabla \cdot \mathbf{B} = 0$), i.e., a magnetic field is source free; it is therefore not possible to create a static magnetic field maximum in free space. However, static local minima can be created allowing one to trap low-field seekers. For moderate magnetic fields, typical trap depths are on the order of a few mK, and atoms have to be cooled before they are loaded into the trap. Much deeper traps on the order of 1 K have also been built, where superconductive coils were used to achieve these high magnetic fields [58].

A very simple way to realize a magnetic trap is to use a pair of coils in anti-Helmholtz configuration, i.e., the current is flowing in the opposite direction through the two identical coils. The field is zero at the center between the two coils and it increases linearly in all directions close to the center. Because the divergence of the magnetic field is zero and due to the symmetry of the quadrupole field, the gradients obey the following equation

$$\frac{\partial B}{\partial z} = 2 \frac{\partial B}{\partial x} = 2 \frac{\partial B}{\partial y}. \quad (2.3)$$

Thus, the gradient on the symmetry axis of the two coils (z) is twice as large as the gradient in the plane (x, y).

2.1.3 Density in a quadrupole trap

Assuming that the atoms do not interact with each other, the density can be calculated using the Boltzmann distribution. For thermal equilibrium at a temperature T the density distribution is given by:

$$n(\mathbf{r}) = n_0 e^{-\frac{E_{\text{pot}}(\mathbf{r})}{k_B T}}, \quad (2.4)$$

where n_0 is the peak density at the center of the trap and k_B is the Boltzmann constant. Inserting the quadrupole potential yields

$$n(x, y, z) = n_0 e^{-B' \sqrt{x^2 + y^2 + (2z)^2}}, \quad (2.5)$$

where

$$B' = \frac{m_F g_F \mu_B}{2k_B T} \frac{\partial B}{\partial z}. \quad (2.6)$$

Additionally, gravity acts along z . To take this into account, the density function has to be multiplied by $e^{-\frac{mg}{k_B T} z}$.

2.1.4 Majorana transitions

As the atoms move in the trap, their spins follow the magnetic field lines adiabatically. However, at the center of the trap the field is zero, and the atoms can undergo spin flips to untrapped states, if their Larmor frequency is smaller than the rate of change of the magnetic field direction. These transitions are called *Majorana spin flips* or *Majorana transitions*. To circumvent this problem, a number of different traps have been designed such that the minimum of the field always has a non-zero value (e.g., the Ioffe-Pritchard trap [130], the TOP trap [131], the baseball trap [132], the cloverleaf trap [133] and the QUIC trap [134]). In the quadrupole trap Majorana spin flips limit the trap lifetime τ depending on the size of the atom cloud

$$\tau = \frac{1}{4} \alpha \sigma_{\text{FWHM}}^2, \quad (2.7)$$

where α was empirically found to be $3.7 \times 10^4 \text{ s/cm}^2$ for rubidium, and σ_{FWHM} is the radial full width half maximum of the cloud [129]. Thus, the lifetime can be severely limited for small atom clouds.

2.2 Laser cooling

The technique of laser cooling was a breakthrough in the field of cold matter. It has led to an intense worldwide activity within the atomic, molecular and optical physics community and has opened up new roads towards the study of the quantum behavior of dilute atomic vapors at very low temperatures. In recognition of these achievements, the Nobel prize in physics was awarded in 1997 to S. Chu, C. Cohen-Tannoudji and W.D. Phillips ‘for development of methods to cool and trap atoms with laser light’.

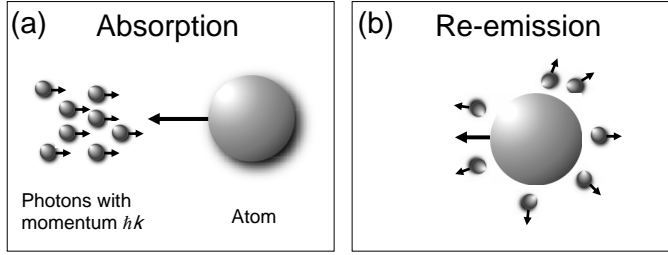


Figure 2.1: Absorption and emission of photons. (a) Photons of a directed light beam are hitting the atoms and thereby imposing a momentum transfer of $\hbar k$ per photon. (b) Subsequent spontaneous emission is distributed randomly in all directions which, on average, results in zero net momentum transfer.

2.2.1 Atoms in light fields

When an atom absorbs or emits a photon, momentum conservation requires the atom to change its momentum along the direction of the light beam \mathbf{k} , where $k = |\mathbf{k}| = 2\pi/\lambda$ is the wave vector and λ is the wavelength. Each photon carries a momentum of $\hbar k$, where $\hbar = h/2\pi$ and h is the Planck constant. Thus, each photon recoil changes the velocity of the atom by $\hbar k/m$ where m is the mass of the atom. This is illustrated in Fig. 2.1(a). If an atom repeatedly absorbs photons from a light beam, the momentum kicks add up and result in a force along the beam direction. On the other hand, the subsequent spontaneous emission of photons is distributed isotropically in space [Fig. 2.1(b)]. Over a number of absorption and emission cycles the average momentum transfer of all spontaneously emitted photons is zero. As the lifetime of the excited state is typically on the order of $10^{-8} - 10^{-9}$ s, many absorption-emission cycles can take place in a relatively short time. This makes it possible to achieve appreciable atom accelerations which reach values up to 10^4 times higher than the gravitational acceleration [135].

For a quantitative description, consider a two-level system with a ground state $|g\rangle$ and an excited state $|e\rangle$ as shown in Fig. 2.2. The energy difference between the two levels is $\Delta E = \hbar\omega_0 = h\nu_0$, where ν_0 is the transition frequency and $\omega_0 = 2\pi\nu_0$ is the angular transition frequency. By absorbing photons from a laser beam with a frequency $\omega_L = \omega_0 - \delta$, the atom can be excited to the upper state. Subsequently, it will spontaneously decay to the ground state $|g\rangle$, releasing a photon of energy $\hbar\omega_0$. The decay rate from the excited state back to the ground state is Γ , and the lifetime of the excited state is therefore given by $\tau = 1/\Gamma$. Γ is called the *natural linewidth* of the transition and is identical to the Einstein A coefficient [136]. For a two-level system the probability ρ_e that the excited state is populated is given by

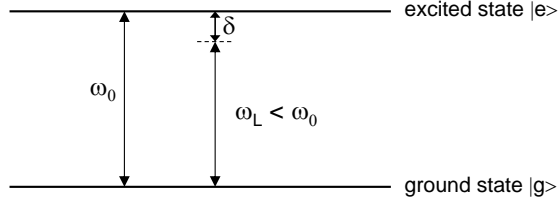


Figure 2.2: Two-level system with ground state $|g\rangle$ and excited state $|e\rangle$. The laser frequency ω_L driving the transition is red detuned by δ from the transition frequency ω_0 .

$$\rho_e = \frac{1}{2} \frac{I/I_{\text{sat}}}{1 + I/I_{\text{sat}} + (\frac{2\delta}{\Gamma})^2}, \quad (2.8)$$

where I is the intensity of the laser light, I_{sat} the saturation intensity, δ the detuning of the laser from the transition frequency $\delta = \omega_L - \omega_0$, and Γ the natural linewidth [135]. The saturation intensity I_{sat} is given by

$$I_{\text{sat}} = \frac{\pi \hbar c}{3\lambda^3 \tau}, \quad (2.9)$$

where c is the speed of light. For low intensities I , the atoms reside mostly in the ground state, while for high intensities the population is equally distributed between the ground and the excited state. Note that additional Doppler or Zeeman shifts can change the effective detuning from the transition frequency ω_0 . Under steady state conditions, the excitation and decay rates are equal, and the scattering rate Γ_{sc} is given by the product of the decay rate Γ and the excited state probability ρ_e :

$$\Gamma_{\text{sc}} = \Gamma \rho_e = \frac{\Gamma}{2} \frac{I/I_{\text{sat}}}{1 + I/I_{\text{sat}} + (\frac{2\delta}{\Gamma})^2}. \quad (2.10)$$

Knowing the scattering rate Γ_{sc} , the force F_{sp} an atom experiences upon absorption followed by spontaneous emission is simply the product of the photon recoil $\hbar k$ and Γ_{sc}

$$F_{\text{sp}} = \hbar k \Gamma_{\text{sc}}. \quad (2.11)$$

In the literature, the force F_{sp} is called the *light pressure force*, the *radiation pressure force* or the *dissipative force* [135].

2.2.2 Doppler cooling and optical molasses

To cool atoms the thermal energy of the atoms needs to be dissipated. The first proposal to cool atoms using laser radiation was made in 1974 by T.W. Hänsch

and A.L. Schawlow [12]. In this section, the principle of Doppler cooling is presented as the most important mechanism to bring atoms from room temperature down to the microkelvin range.

Doppler cooling can be explained most easily in one dimension. Consider a two-level atom which moves with a velocity \mathbf{v} towards a laser beam with frequency ω_L . Depending on its velocity the atom will see the laser light frequency shifted by $-\mathbf{k}\mathbf{v}$ due to the Doppler effect. Therefore, in the light field of two counterpropagating laser beams with the same intensity and with a detuning of δ , a velocity-dependent force will arise. In the case of a red detuning (i.e., to lower energies) of the laser beams the atoms will scatter mostly photons from the beam towards which they are moving. If the atoms repeatedly absorb photons from this laser beam, the momentum kicks from the photons will slow and cool them. The force can be calculated using Eq. 2.11:

$$F_{\text{total}} = \hbar k \frac{\Gamma}{2} \left[\frac{I/I_{\text{sat}}}{1 + I/I_{\text{sat}} + (\frac{2(\delta - kv)}{\Gamma})^2} - \frac{I/I_{\text{sat}}}{1 + I/I_{\text{sat}} + (\frac{2(\delta + kv)}{\Gamma})^2} \right]. \quad (2.12)$$

The forces F_+ and F_- from the two counterpropagating laser beams are plotted in Fig. 2.3 as a function of velocity. The maximum force is achieved for a detuning of the laser of $\delta = -\mathbf{k}\mathbf{v}$. For a laser detuning of $\delta = \Gamma$ and an intensity of $I = I_{\text{sat}}$ the maximum light pressure force occurs for rubidium at a velocity of about ± 5 m/s, respectively. The solid line shows the sum of the forces which leads to a damping of the movement of the atoms and cools them. If the atoms have relatively high velocities (i.e., towards velocities of $v > \pm 30$ m/s) the force becomes small and the atoms will not be slowed. Because of the important role of the Doppler effect, this process is called *Doppler cooling*.

Using a three-dimensional setup, i.e., three pairs of counterpropagating laser beams, the movement of the atoms can be cooled down to the microkelvin range. At the location where the six beams overlap, the atoms behave as if they were moving in a highly viscous medium, hence the name *optical molasses*. Note that the slowing force has everywhere the same strength. Therefore, an atom cloud cannot be confined using such a setup, an additional locally varying force is needed to accomplish trapping.

The emission of photons takes place statistically in all directions and the atoms perform a random walk in velocity space. Therefore, shining laser light on the atoms does not only cool them, but also introduces heating. For this reason, there is a temperature limit, the *Doppler limit* T_D [135], which is the lowest equilibrium temperature reached when Doppler cooling is applied. The equilibrium temperature takes its lowest value for a laser detuning of $\Gamma/2$:

$$T_D = \frac{\hbar\Gamma}{2k_B}. \quad (2.13)$$

The Doppler temperature of ^{87}Rb is $T_D = 146 \mu\text{K}$. The Doppler limit is not the lowest possible temperature which can be obtained with laser cooling. Using

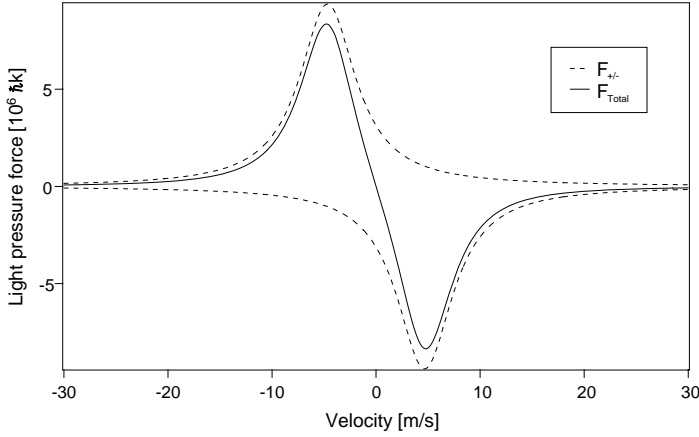


Figure 2.3: Velocity dependence of the light pressure force in a one-dimensional optical molasses for $I = I_{\text{sat}}$ and $\delta = -\Gamma$. The dashed lines show the two components of the force in the $\pm k$ direction. The solid line shows the sum of the two forces, which has a linear behavior for small velocities.

polarization-gradient cooling much lower temperatures can be achieved [20, 21, 137]. These temperatures are on the order of ten times the *recoil limit* when again statistical heating starts to play a role. The *recoil limit* is the temperature associated with the kinetic energy of one photon recoil

$$T_r = \frac{(\hbar k)^2}{mk_B}, \quad (2.14)$$

where m is the mass of the atom. For ^{87}Rb the recoil limit corresponds to a temperature of $T_r = 362$ nK, and the lowest temperatures that have been achieved with ^{87}Rb are around $2 \mu\text{K}$ [138].

2.2.3 Magneto-optical trap (MOT)

As already mentioned in the previous section, the cooling force does not have any dependence on position and therefore cannot spatially confine the atoms. Trapping of atoms was finally achieved by the development of the *magneto-optical trap*. As the name suggests, magnetic fields are applied in addition to the light fields to confine the atoms to a particular location in space. The magneto-optical trap (MOT) was realized for the first time in 1987 [19] and it has rapidly become the starting point for many exciting experiments in the field of cold atoms.

The principle of the MOT is explained here in a one-dimensional model. Consider a linearly varying magnetic field as illustrated in Fig. 2.4(a) and an

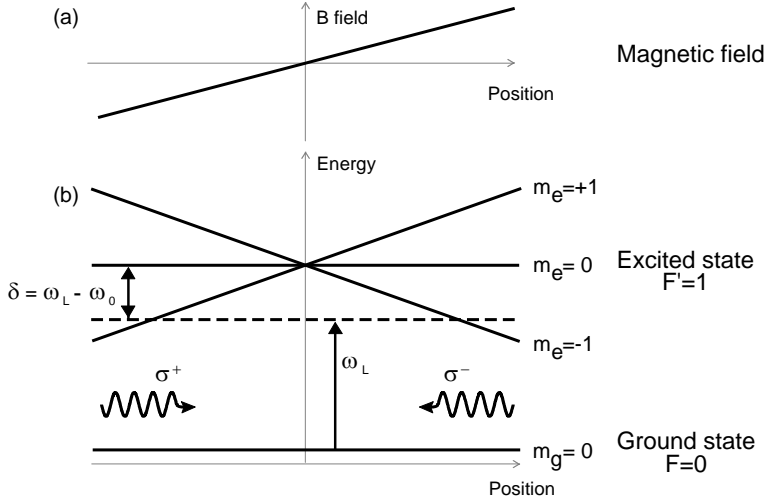


Figure 2.4: Principle of the MOT in one dimension. (a) Linearly varying magnetic field. (b) Zeeman splitting of the magnetic sublevels of the $F = 0 \rightarrow F' = 1$ transition due to the magnetic field. The frequency of the laser ω_L is detuned from the transition by δ , and the two counterpropagating beams are appropriately circularly polarized. The magnetic field B is zero at the center and thus the atoms located there are not on resonance with the laser beams. When an atom moves away from the center, it will get closer to resonance with the beam it is moving towards and further out of resonance with the counterpropagating beam. Therefore, the atom scatters more photons from the former beam, which results in a restoring force that pushes the atom back to the origin.

atom with a ground state F_g and an excited state F_e . For the atomic transition $F_g = 0 \rightarrow F_e = 1$, the upper hyperfine level splits into three magnetic sublevels in an external field [Fig. 2.4(b)]. The two counterpropagating laser beams have circular polarization of identical handedness and are detuned from the transition frequency ω_0 by δ . With respect to the direction of the magnetic field the two counterpropagating beams are then σ^+ or σ^- polarized. Because of the Zeeman effect, the sublevel $m_e = -1$ is shifted up for $B < 0$, while the sublevel with $m_e = +1$ is shifted down. For an atom moving towards more negative magnetic fields (left-hand side in Fig. 2.4), the $\Delta m = +1$ transition is tuned closer to resonance, whereas the $\Delta m = -1$ transition is tuned further out of resonance. As the beam incident from the left is σ^+ polarized, more light is scattered from this beam than from the σ^- beam. Consequently, the atoms are driven towards the center of the trap where the magnetic field is zero. If the atom is moving towards more positive magnetic fields, the roles

of the $m_e = \pm 1$ states are reversed and the atom is pushed to the center by the σ^- beam. In this way, the linearly varying magnetic fields provide spatial confinement. Together with the mechanism of Doppler cooling, atoms can thus be cooled and confined in space in a magneto-optical trap.

The Zeeman shift of a transition between two states $|g\rangle$ and $|e\rangle$ is given by $\delta_{\text{Zeeman}} = (m_F^e g_F^e - m_F^g g_F^g) \mu_B B / \hbar = \mu' B / \hbar$. The total light force $F = F_+ + F_-$ can be calculated from Eq. 2.12 by adding this Zeeman energy term

$$F_{\pm} = \pm \hbar k \frac{\Gamma}{2} \left[\frac{I/I_{\text{sat}}}{1 + I/I_{\text{sat}} + 4[(\delta \mp kv \pm \mu' B / \hbar) / \Gamma]^2} \right]. \quad (2.15)$$

The MOT scheme can be easily extended to three dimensions by using three pairs of red-detuned counterpropagating laser beams. For each pair one beam is σ^+ polarized and the counterpropagating beam is σ^- polarized. As discussed earlier, a magnetic quadrupole field provides a linearly varying magnetic field in all three dimensions with zero field at the center, which can be implemented using a pair of coils in anti-Helmholtz configuration. Even though most atoms do not have transitions as simple as $F_g = 0 \rightarrow F_e = 1$, the scheme also works for $F_g \rightarrow F_e = F_g + 1$ transitions. Occasionally, off-resonant transitions occur and the atoms spontaneously decay to a lower hyperfine state which is not in resonance with the cooling laser. Then the atom has to be pumped back to the upper hyperfine level, otherwise it would be lost from the trap. This can be done by using a second laser which is commonly referred to as *repumper laser*.

2.2.4 Density distribution in the trap

Temperature limited regime

For small atom numbers in the MOT (typically around 10^4 atoms) repulsive forces between the atoms due to multiple scattering of photons can be neglected and the energy of the atoms is only determined by the trapping potential [139–141]. Therefore, for thermal equilibrium at a temperature T the density distribution is given by:

$$n(\mathbf{r}) = n_0 e^{-\frac{E_{\text{pot}}(\mathbf{r})}{k_B T}}, \quad (2.16)$$

where n_0 is the peak density at the center of the trap.

To determine the potential energy in the MOT, it is possible to expand the denominator of the light pressure force for small velocities and small displacements [135]. The resulting equations of motion for every component r_i ($i = x, y, z$) are those of a damped harmonic oscillator with a friction coefficient ξ and a spring constant κ

$$F(r_i, v_i) = -\kappa_i r_i - \xi v_i. \quad (2.17)$$

The spring constant κ is given by

$$\kappa_i = \frac{\mu'}{\hbar k} \frac{\partial B}{\partial r_i} \xi, \quad (2.18)$$

where $\frac{\partial B}{\partial r_i}$ is the gradient of the magnetic field, $\mu' \equiv (m_{\text{F}}^e g_{\text{F}}^e - m_{\text{F}}^g g_{\text{F}}^g) \mu_{\text{B}}$, and ξ is the damping coefficient of the force

$$\xi = 4\hbar k^2 \frac{I}{I_0} \frac{2\delta/\Gamma}{(1 + I/I_0 + (2\delta/\Gamma)^2)^2}. \quad (2.19)$$

Here δ is the effective detuning from the atomic transition, including the Zeeman and Doppler shifts.

The density distribution is Gaussian in x , y and z with a standard deviation of $\sigma_i = \sqrt{k_{\text{B}} T / \kappa_i}$

$$n(r_i) \propto e^{-\frac{r_i^2}{2\sigma_i^2}}, \quad i = x, y, z. \quad (2.20)$$

Note that σ_i depends on the trap parameters and temperature but not on the total number of atoms N . As the spring constant κ is proportional to the gradient of the magnetic field and the divergence of the magnetic field has to vanish (see Eq. 2.3 and [141]), it follows that

$$\kappa_x = \kappa_y = \frac{1}{2} \kappa_z. \quad (2.21)$$

Inserting this in Eq. 2.20 yields

$$n(x, y, z) = n_0 e^{-\frac{x^2 + y^2 + 2z^2}{2(\sqrt{2}\sigma_{\text{MOT}})^2}}, \quad (2.22)$$

where $\sigma_{\text{MOT}} = \sigma_z = \sqrt{\frac{k_{\text{B}} T}{\kappa_z}}$. The number of atoms in a MOT can be obtained

by integrating the density distribution $N = \int n(\mathbf{r}) d\mathbf{r} = n_0 \int e^{-\frac{E_{\text{pot}}(\mathbf{r})}{k_{\text{B}} T}} d\mathbf{r}$. This integral is often referred to as the *effective volume* $V_{\text{eff}} = N/n_0$. In case of a Gaussian distribution it can be written as

$$V_{\text{eff}} = 2(2\pi)^{3/2} \sigma_{\text{MOT}}^3 = (2\pi)^{3/2} \sigma_x \sigma_y \sigma_z. \quad (2.23)$$

Multiple scattering regime

For a medium number of atoms in the trap (typically above 10^4 atoms), reabsorption of scattered photons within the trapped cloud plays a role. In reference [141] it is found that the volume of the trapped cloud grows when more atoms are added while the density remains constant, independent on the number of atoms. This is attributed to repulsive interatomic forces due to reabsorption

of the scattered photons in the cloud. The density in the multiple scattering regime n_{MS} is given by

$$n_{\text{MS}} = \frac{3\kappa c}{I_{\text{tot}}\sigma_{\text{L}}^2(\sigma_{\text{R}}/\sigma_{\text{L}} - 1)}, \quad (2.24)$$

where I_{tot} is the total light intensity of the six trapping beams, σ_{L} is the optical cross section for absorption of photons from the laser field and σ_{R} is the optical cross section for absorption of photons reradiated from atoms in the trapped cloud. If even more atoms are loaded into the trap, the cloud will eventually fill the central, strongly confining region and will then spread out radially. This is referred to as the *two-component regime* in [141].

With a total number of 5×10^8 atoms our MOT is well above typical values for the temperature limited regime. Taking the detuning, the overall intensity of the laser beams, and the gradient in our MOT into account, we can assign it to the multiple scattering regime.

2.2.5 Zeeman slower

A MOT can be loaded either from the vapor background or from a predecelerated beam and has typical capture velocities between 10 m/s and 40 m/s. If the MOT is loaded from vapor background only a small part of the Boltzmann distribution of the gas can be loaded into the trap, as the average velocity at 300 K is much higher than the capture velocity of the MOT. Usually a vapor background MOT implies smaller lifetimes as the trapped atoms collide with faster atoms from the background leading to trap losses. In this experiment, the MOT is loaded from a slow beam to ensure fast loading rates, long lifetimes and therefore high atom numbers and densities.

A standard method to decelerate a beam of atoms is to exploit the Doppler shift and to cool the atoms along the beam axis by using the light force F_{sp} . In a typical setup a laser beam is sent counterpropagating to the atom beam coming from the source chamber. The light force, however, is velocity dependent due to the changing Doppler shift and therefore the resonance frequency changes if the atoms become slower. Eventually, the atoms will fall out of resonance and will no longer be decelerated if they have been slowed down too much. To decelerate atoms from several hundreds of meters per second to a few tens of centimeters per second one needs to compensate for the changing Doppler shift. This can be achieved by sweeping the frequency of the laser beam to keep it resonant with the decelerated atoms, which results in small packets of slow atoms. Another method is to apply a spatially varying magnetic field which shifts the Zeeman levels of the atomic resonance. To produce the inhomogeneous magnetic field a so-called *Zeeman slower* is used as drawn schematically in Fig. 2.5. In the first successful experiment where an atom beam was decelerated such a Zeeman slower was used [16].

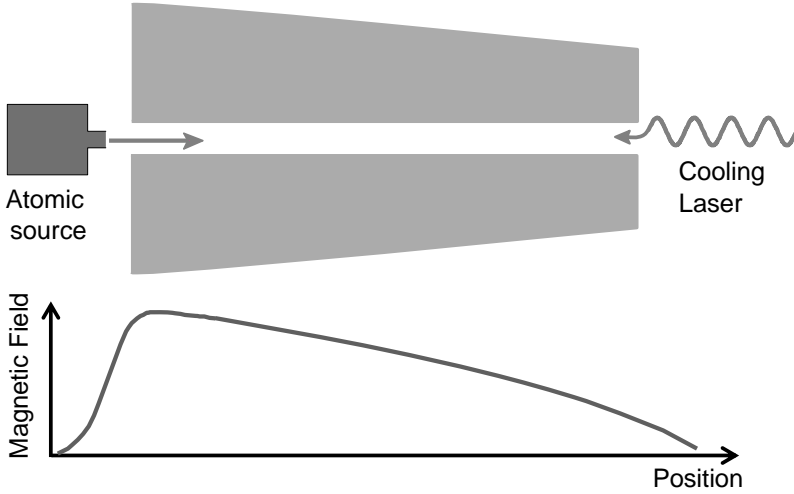


Figure 2.5: Scheme of a Zeeman slower. The atoms coming from an oven enter the slower where they are decelerated by the counterpropagating beam. The Zeeman slower provides the inhomogeneous magnetic fields needed to keep the atoms on resonance. The magnetic field as a function of position is schematically shown in the lower part.

To match the magnetic field in our Zeeman slower exactly to the change in the resonance frequency one needs to find the correct detuning from resonance. It is advantageous not to keep the atoms exactly at the top of the resonance profile shown in Fig. 2.3 for F_+ and F_- , because this would be an unstable configuration. An atom that is too fast can get on the 'wrong' side of the resonance where it will feel a smaller force and therefore get further out of resonance. If an atom, however, experiences about half the maximum light force the situation will be stable. A fast atom will then experience a stronger force and be more decelerated, whereas a slow atom will no longer be decelerated until it is resonant again. So the atom velocity at the exit of the Zeeman slower is fairly well peaked around a certain velocity. It is advantageous to slow down the atoms at a constant deceleration a . The maximum deceleration is $a_{\max} = F_{\text{sp},\max}/m$ where $F_{\text{sp},\max} = \hbar k \Gamma / 2$ is the maximum light pressure force. For a constant deceleration a the velocity of the atoms changes according to

$$v(z) = v_0 \sqrt{1 - \frac{2az}{v_0^2}}, \quad (2.25)$$

where v_0 is the initial velocity. The changing Doppler shift $\mathbf{k} \cdot \mathbf{v}$ has to be

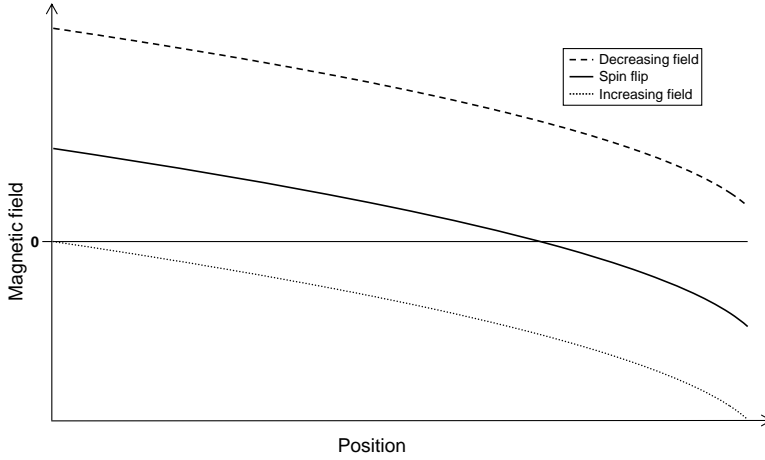


Figure 2.6: Magnetic field versus position in the Zeeman slower for different Zeeman slower configurations.

compensated by the Zeeman shift and the detuning δ of the laser beam

$$\mathbf{k}\mathbf{v} = \mu' B/\hbar + \delta, \quad (2.26)$$

where $\mu' = (m_F^e g_F^e - m_F^g g_F^g) \mu_B$ takes into account the difference in magnetic moments between the ground and the excited states. Inserting Eq. 2.25 in Eq. 2.26 yields

$$B(z) = \frac{\hbar}{\mu'} (kv_0 \sqrt{1 - \frac{2az}{v_0^2}} - \delta), \quad (2.27)$$

where the acceleration is typically chosen to be $a = \frac{1}{2} a_{\max}$.

There are several types of Zeeman slower that differ in the magnitude of the magnetic field across the length of the Zeeman slower and in the detuning of the laser frequency. One possibility is to use a so-called *increasing-field* Zeeman slower where the magnetic field is zero at the beginning of the slower and increases towards the end where the atoms enter the MOT (dotted line in Fig. 2.6). The laser beam needs to have a large red detuning to be resonant with the fast atoms from the oven. Disadvantages of this system are the high fields close to the MOT which need to be compensated for and the large laser detuning.

A different approach is the *decreasing-field* Zeeman slower with high magnetic fields at the entrance of the slower and decreasing fields towards the MOT (dashed line in Fig. 2.6). The laser beam needs then to be resonant with the slow atoms at the exit of the Zeeman slower. A problem here is that the atoms

which just exit the slower are still resonant with the laser beam and can potentially be accelerated back in. Additionally, the slowing beam disturbs the atoms in the MOT. For both types, high magnetic fields are employed, either at the beginning or at the exit, causing high power dissipation.

To decrease the absolute value of the magnetic field and to circumvent the problems described above, the Zeeman slower can be operated in *spin-flip configuration*, where a magnetic field is created with a zero value somewhere in between the beginning and the exit (solid line in Fig. 2.6). At the entrance of the slower there are moderate fields which then decrease to zero, after which the field increases again but with reversed direction. When the atoms pass through the zero field, the orientation of the magnetic moment stays the same with respect to the moving direction. This results in a spin flip with respect to the reversed direction of the field. The sign of the Zeeman shift changes, and therefore the Doppler shift is still compensated. One problem with this configuration are possible Majorana spin flips in the zero field region where the atoms can lose their spin orientation. This can be prevented by applying a weak bias field perpendicular to the slower axis.

2.3 Trapping by ac electric fields

2.3.1 Interaction with electric fields

The interaction of a particle with an external electric field \mathbf{E} is called the *Stark effect*. An overall neutral system with a non-uniform distribution of positive and negative charges is polar. The polarity of a particle is characterized by the dipole moment \mathbf{p} and the interaction energy of the dipole moment with the electric field is given by

$$E_{\text{Stark}} = -\mathbf{p} \cdot \mathbf{E}. \quad (2.28)$$

If a particle with a permanent dipole moment is brought into an electric field which is not collinear with \mathbf{p} , it will align itself along the electric field. If a particle without a permanent dipole moment, however, is brought into an electric field \mathbf{E} , it will become polarized by the field according to its polarizability α . The Stark energy E_{Stark} can then be written as

$$E_{\text{Stark}} = -\frac{1}{2}\alpha\mathbf{E}^2, \quad (2.29)$$

where α depends on the quantum state of the particle. This *quadratic Stark effect* is common for many atoms. Hydrogen and hydrogen-like atoms in Rydberg states, and many ground-state molecules show a *linear Stark effect* [142]. In this thesis, only the quadratic interaction of ground-state rubidium atoms with electric fields is discussed.

2.3.2 Trapping principles

As for magnetic fields, the sign of the second order Stark interaction is determined by the sign of the polarizability, as \mathbf{E}^2 is always positive in Eq. 2.29. If α is negative the particle is a low-field seeker, if α is positive it is a high-field seeker. For trapping, a restoring force is needed to bring the particles towards the center and therefore the divergence of the force needs to be negative, i.e., $\nabla \cdot \mathbf{F} < 0$. In the case of a quadratic Stark effect it can be shown that

$$\nabla \cdot \mathbf{F} = \alpha \sum_{i,j=1}^3 \left(\frac{\partial^2 \Phi}{\partial x_i \partial x_j} \right)^2, \quad (2.30)$$

where Φ is the electric potential and x_i denotes the coordinates x, y, z [143]. If the particle has a negative α , $\nabla \cdot \mathbf{F} \leq 0$ and the particle can be trapped in an electric field minimum. From Maxwell's equations, it is possible to create such a minimum in free space. If $\alpha > 0$, i.e., in the case of high-field seekers, an electric field maximum must be created to trap the particle. Similar to the magnetic trap case, from Maxwell's equations it can be shown that it is not possible to create a static electric field maximum in free space. This result is also known as Earnshaw's theorem. Nevertheless, it is possible to trap high-field seekers using dynamic fields. The operation principle of an electric trap for neutral particles is similar to that of the Paul trap for ions [112]. A potential energy surface is created with a saddle point at the trap center (i.e., $\nabla \cdot \mathbf{F} = 0$). Along the direction where there is a maximum of the electric field, the high-field seekers experience a focusing force. In the other two directions the electric field has minima and high-field seekers feel a defocusing force. In a so-called ac electric trap, this configuration is switched to another one where the roles of the forces are reversed. Alternating between the two configurations at the appropriate frequency, using either a sine wave or a square wave, leads to dynamic confinement of the particles. An ac electric trap has been demonstrated for the first time in 2005 for ground-state ammonia molecules [116].

Different electrode geometries suitable for ac trapping have been proposed (see Fig. 2.7) and will be discussed here only shortly; for a more extensive description see [118] and [144].

(a) *Linear ac trap*: The linear ac trap consists of four identical electrodes [see Fig. 2.7 (a)] where the same voltage but with different polarity is applied to two opposite electrodes, while the two other electrodes are on ground potential. High-field seekers are focused in the plane of the two electrodes that are on ground potential and defocused along the other direction (along the y axis). Along the symmetry axis, high-field seekers are always confined as the field has a maximum at the center of the trap which results in a static focusing force. This linear ac trap has been demonstrated for ground-state Sr atoms on a chip [121] and for neutral molecules in a macroscopic trap [117].

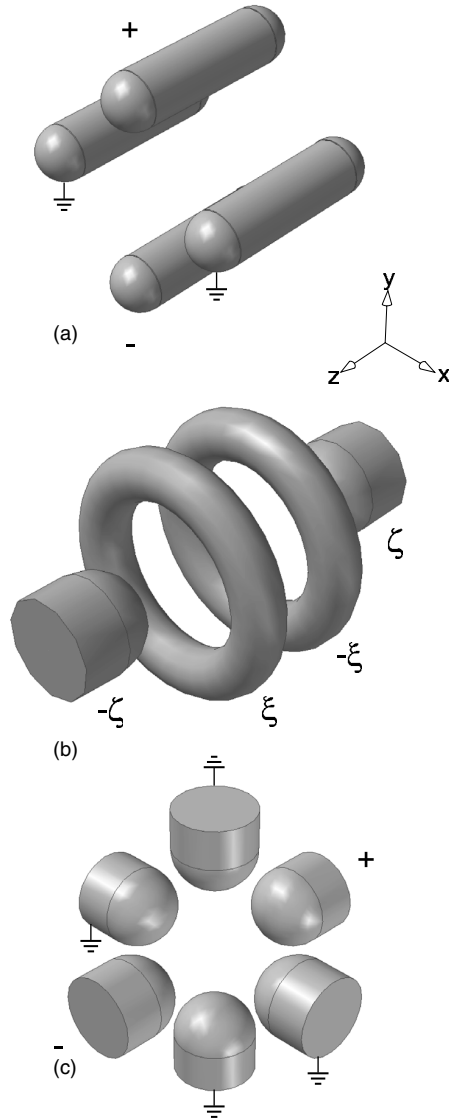


Figure 2.7: Schemes of the different ac trap geometries suitable for trapping. (a) Linear ac trap. (b) Cylindrical ac trap. (c) Three-phase ac trap. The figure is taken from [118].

(b) *Cylindrical ac trap*: This trap also consists of four electrodes, namely two end cap electrodes and two ring electrodes, as illustrated in Fig. 2.7 (b) and Fig. 2.8. Negative voltages are applied to one end cap and to one of the rings while the other two electrodes are on positive voltages. This trap was first proposed for neutral atoms by Peik in 1999 [115] and is the analog of the Paul trap for ions [112]. It has been first demonstrated in 2005 for high-field- and low-field-seeking ammonia [116]. The ac trap used for the experiments described in this thesis also has cylindrical symmetry.

(c) *Three-phase ac trap*: This trap also consists of three pairs of electrodes where each pair is composed of two opposing rods [see Fig. 2.7 (c)]. All six electrodes point towards the center of the trap. While two pairs of electrodes are on ground potential, high voltages with different polarity are applied to the remaining pair. For trapping, the configuration is switched such that high voltage is consecutively applied to each pair of electrodes. This trap is the analog of the three-phase trap for ions [145] and was proposed by Shimizu and Morinaga [113, 114]. An experimental implementation of their idea was recently realized for ground-state rubidium atoms [120].

2.3.3 Equations of motion in an ac trap

To create the required two saddle-point configurations, Peik suggested in his paper to superpose an alternating hexapole field and a static dipole field [115]. As only the hexapole field is switched, the field strength remains constant at the center of the trap preventing unwanted Majorana transitions.

The electric field in such a trap can be derived from the electric potential via $\mathbf{E} = -\nabla \cdot \Phi$. It is useful to write the electric potential as a series of spherical multipoles $\sum_{l,m} a_{lm} r^l Y_{lm}$. Taking the cylindrical symmetry into account, this can be simplified using the Legendre polynomials P_l and cylindrical coordinates¹ as:

$$\Phi(\rho, z) = \sum_{n=0}^m \left[\frac{\Phi_n}{z_0^n} (\rho^2 + z^2)^{n/2} P_n\left(\frac{z}{\sqrt{\rho^2 + z^2}}\right) \right], \quad (2.31)$$

where z_0 characterizes the dimensions of the trap, i.e., the distance between the end cap electrodes. Taking only the first five terms into account (higher-order terms are negligible in our system) we can write:

$$\begin{aligned} \Phi(\rho, z) = & \Phi_0 + \Phi_1 \frac{z}{z_0} + \Phi_2 \frac{z^2 - \rho^2/2}{z_0^2} + \Phi_3 \frac{z^3 - \frac{3}{2}z\rho^2}{z_0^3} + \\ & \Phi_4 \frac{z^4 - 3\rho^2 z^2 + \frac{3}{8}\rho^4}{z_0^4} + \Phi_5 \frac{z^5 - 5z^3\rho^2 + \frac{15}{8}z\rho^4}{z_0^5}. \end{aligned} \quad (2.32)$$

¹Due to axial symmetry all multipole moments m are zero apart from $m = 0$. Then $\sqrt{\frac{4\pi}{2l+1}} Y_{l0}(\theta, \phi) = P_l(\cos \theta)$. Transformation to cylindrical coordinates yields $r = \sqrt{\rho^2 + z^2}$ and $\cos \theta = \frac{z}{\sqrt{\rho^2 + z^2}}$.

The first term describes a constant voltage, the second term represents a constant dipole field, the Φ_2 term is the quadrupole potential and the Φ_3 term is the hexapole component. The Φ_4 and Φ_5 terms are unwanted octupolar and decapolar field components. The electric field strength can be derived from 2.32 using the expression $E(\rho, z) = \sqrt{(\frac{\partial \Phi}{\partial \rho})^2 + (\frac{\partial \Phi}{\partial z})^2}$. As mentioned before, the energy of an atom with a second order Stark effect is $E_{\text{Stark}} = -\frac{\alpha}{2}E^2$, and the force can be derived via $\mathbf{F} = -\nabla E_{\text{Stark}}$. The forces in ρ and z read

$$F_\rho = \frac{\alpha}{2} \left[\frac{2\Phi_2^2 \rho}{z_0^4} + \frac{9\Phi_3^2 \rho^3}{z_0^6} - \frac{6\Phi_1 \Phi_3 \rho}{z_0^4} \right], \quad (2.33)$$

and

$$F_z = \frac{\alpha}{2} \left[\frac{8\Phi_2^2 z}{z_0^4} + \frac{36\Phi_3^2 z^3}{z_0^6} + \frac{4\Phi_1 \Phi_2}{z_0^3} + \frac{12\Phi_1 \Phi_3 z}{z_0^4} + \frac{36\Phi_2 \Phi_3 z^2}{z_0^5} \right]. \quad (2.34)$$

In Eq. 2.33 the first two terms will always be defocusing independent of the sign of Φ_2 and Φ_3 , whereas the third term changes sign if the voltage Φ_3 is switched. We assume that trapped particles experience only small displacements from the center, and that the quadrupole component is much smaller than the dipole and the hexapole components:

$$\rho^2 + z^2 \ll z_0^2 \text{ and } \Phi_2 \ll \Phi_1 \approx \Phi_3. \quad (2.35)$$

The third term dominates in F_ρ and thus leads to trapping, when an alternating voltage Φ_3 is applied. In Eq. 2.34 the crucial term is the fourth term which is proportional to $\Phi_1 \Phi_3$ and linear in z , and thus governs the trapping forces. The first two terms are defocusing but small. The last term is proportional to $\Phi_2 \Phi_3$ and changes sign with Φ_3 . It is proportional to z^2 and therefore anharmonic, but due to the small value of Φ_2 it is much smaller than the fourth term. The third term is proportional to $\Phi_1 \Phi_2$ and results in a static force which can be used to counteract gravity. This is important if the trapping forces are comparable to gravity, as is the case for atoms with small polarizabilities. Setting this term equal to $F_g = mg$ where g is the acceleration due to gravity, we obtain

$$\Phi_2 = \frac{mgz_0^3}{2\alpha\Phi_1}. \quad (2.36)$$

To derive the equations of motion we focus on the fourth term of the force F_z in Eq. 2.34. We assume that the voltage Φ_3 varies in time according to a sinusoidal function

$$\Phi_3(t) = \Phi_3 \sin \omega t, \quad (2.37)$$

where Φ_3 now denotes the amplitude of the oscillation. The equations of motions are then

$$\frac{\partial^2 z}{\partial \tau^2} - 2q_z \sin 2\tau z = 0, \quad (2.38)$$

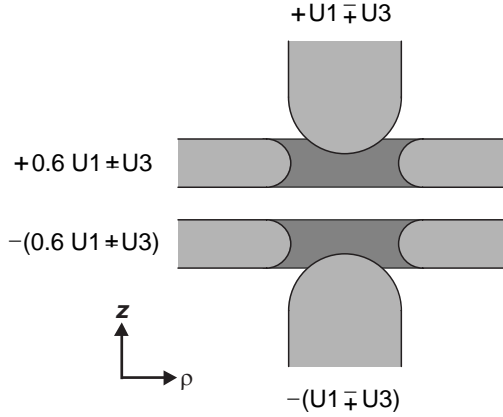


Figure 2.8: Schematic view of the ac trap geometry. It consists of two end cap electrodes and two ring electrodes. The distance between the two end caps is $2z_0$. To generate a constant dipole field superposed onto an alternating hexapole field, the voltages $\pm(U_1 \mp U_3)$ are applied to the end cap electrodes and the voltages $\pm(U_1 \pm 0.6 U_3)$ are applied to the ring electrodes.

with

$$\tau = \frac{\omega t}{2} \quad \text{and} \quad q_z = \frac{12\alpha\Phi_1\Phi_3}{m\omega^2 z_0^4} \quad (2.39)$$

This equation is known as the *Mathieu differential equation* and it has stable solutions as long as $|q_z| < 0.907$. A similar equation can be derived for the ρ direction.

From radio frequency ion trap experiments it is known that the motion of the trapped ions consists of a fast *micromotion* driven at the switching frequency ω and a slower *secular motion*. More generally, if $q_z \ll 1$ the dynamics of the trapped particle can be separated into the two different motions and a static *pseudopotential* Ψ can be derived [115].

$$\Psi(\rho, z) = \frac{\mathbf{F}^2}{4m\omega^2} = \frac{1}{64} [q_z^2 m \omega^2 (\rho^2 + 4z^2)]. \quad (2.40)$$

In this case, the secular motion is a harmonic oscillation with frequencies $\omega_z = \omega q_z / \sqrt{8}$ and $\omega_\rho = \omega_z / 2$. From Eq. 2.40 we can see that the trapping potential is deeper when the driving frequency ω is smaller, if the voltages Φ_1 , Φ_3 are kept constant.

It is more difficult to derive the equations of motion if the voltage applied to the electrodes is switched using a square-wave function, as is the case in our experiment. The equations of motion have to be solved piecewise, and the

solution is known as *Hill's equation*. For a detailed description see Refs. [118] and [144].

To create the desired field (a dipole field superposed onto an alternating hexapole field) in the cylindrical ac trap, high voltages U_1 and U_3 are applied as shown in Fig. 2.8. To match the voltages as perfectly as possible to the electrode geometry, a finite-element software (Comsol) was used to simulate the electric field. The simulated field was subsequently fit with Mathematica using a multipole expansion up to the ninth order (see Eq. 2.31). If only the voltage U_3 is applied to the electrodes, an almost perfect hexapole field is created: from the fit, we get $\Phi_1 = 0.02 U_3$, $\Phi_3 = 0.99 U_3$, $\Phi_5 = 0.01 U_3$ and $\Phi_7 = -0.013 U_3$, the other multipole terms are zero. If only the voltage U_1 is applied (i.e., $\pm U_1$ to the end caps and $\pm 0.6 U_1$ to the rings, see Fig. 2.8), the dipole field is not as perfectly matched: $\Phi_1 = 0.888 U_1$, $\Phi_3 = 0.005 U_1$, $\Phi_5 = 0.106 U_1$ and $\Phi_7 = -0.005 U_1$, the other multipole terms are zero or negligibly small. The field has a rather big Φ_5 component which introduces nonlinearities that can lower the trap depth considerably.

Chapter 3

Experimental apparatus for cold atoms

3.1 Atomic properties of rubidium

3.1.1 Transitions and properties of ^{87}Rb

The alkali element rubidium is the workhorse in the field of cold atoms. It is easily available, the transition frequencies in the near infrared can be provided conveniently using diode lasers, and it has been studied in great detail. There are two rubidium isotopes, ^{85}Rb and ^{87}Rb , where the natural abundance is 72.2% for ^{85}Rb and 27.8% for ^{87}Rb . Of these two isotopes, only ^{85}Rb is stable, while ^{87}Rb has an extremely slow decay rate of more than 10^{10} years which makes it practically stable. ^{87}Rb has 37 electrons and 87 nucleons. The vapor pressure at 25°C is $P_v = 4.0 \times 10^{-7}$ mbar, as can be seen from the rubidium vapor pressure curve (Fig. A.4). All relevant physical properties of ^{87}Rb can be found in Table A.1 in the appendix.

^{87}Rb has an electron spin of $S = 1/2$ arising from an unpaired electron in the outermost shell. Therefore, in the ground state $J = 1/2$ and the term symbol is $5^2S_{1/2}$. The coupling between the nuclear spin of $I = 3/2$ and the ground state angular momentum results in two hyperfine states, $F = 1$ and $F = 2$. Figure 3.1 shows the D_1 and the D_2 transitions. The wavelengths are in the near-infrared region, 795 nm for the D_1 transition and 780 nm for the D_2 transition. The D_2 transition $5^2S_{1/2}(F = 2) \rightarrow 5^2P_{3/2}(F = 3)$ in ^{87}Rb is used as cycling transition for laser cooling, as indicated in Fig. 3.1 where the red detuning of the beam in the experiment is $\Delta = -14$ MHz. The lifetime of the $5^2P_{3/2}$ excited state is $\tau = 26.2$ ns, corresponding to a linewidth $\Gamma = 1/\tau = 2\pi \times 6.1$ MHz.

The separation between the $5^2P_{3/2}$, $F = 2$ and $F = 3$ hyperfine states is

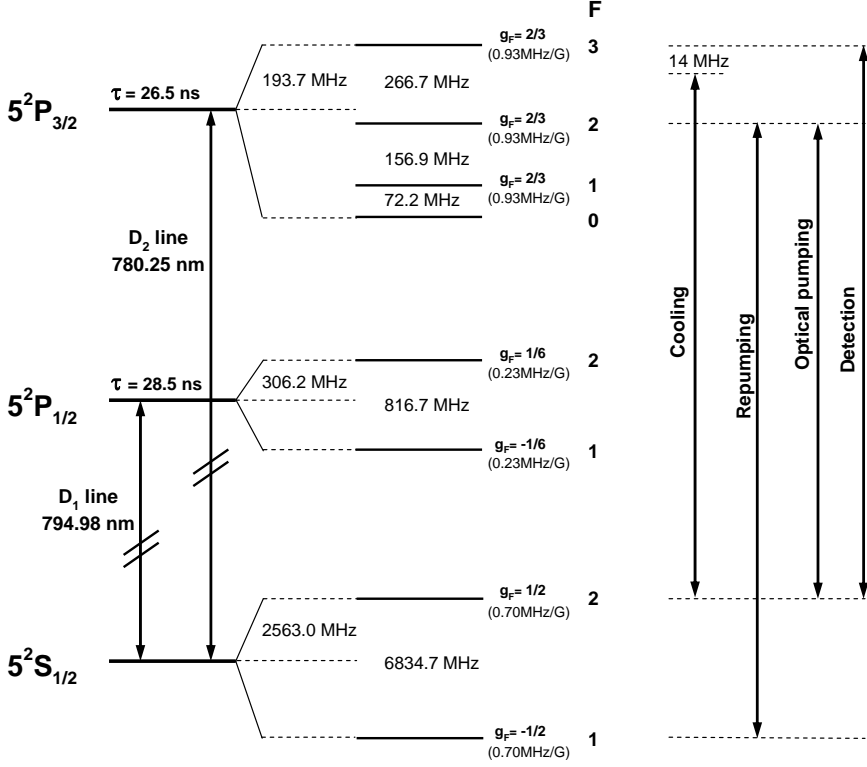


Figure 3.1: Hyperfine structure of ^{87}Rb with corresponding frequency splittings. The arrows on the right-hand side show the relevant transitions used for cooling, repumping, optical pumping and detection. The g_F Landé factors for each level are also given along with the corresponding Zeeman splittings between adjacent magnetic sublevels.

267 MHz. As the levels are so close together, there is a nonzero probability that the atoms are excited to the $5^2P_{3/2}$, $F = 2$ state which can decay to both hyperfine levels of the ground state, $F = 2$ and $F = 1$. If a transition to the $F = 1$ ground level occurs, the atoms are no longer affected by the cooling light and leave the trap. Even though the probability of falling into the untrapped hyperfine state is very small ($\approx 3 \times 10^{-5}$ for a saturation intensity of $I = I_{\text{sat}}$ and a detuning of 2Γ), it becomes important as the cycling transition has to be driven several thousand times before an atom is cooled down from room temperature to the Doppler temperature. To prevent the atoms from falling to the $5^2S_{1/2}$, $F = 1$ level and subsequently leaving the trap, a second, so-called *repumper laser* is added which is tuned to the $5^2S_{1/2}(F = 1) \rightarrow 5^2P_{3/2}(F = 2)$

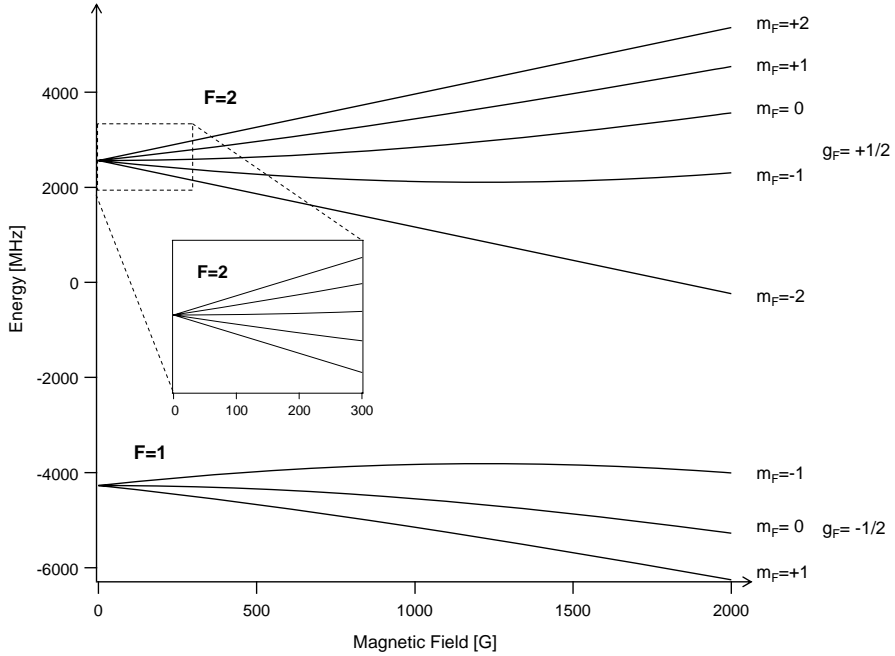


Figure 3.2: Zeeman effect of ^{87}Rb . Plotted is the Zeeman energy of the $5^2S_{1/2}$ ground state in MHz versus the magnetic field in G. The $5^2S_{1/2}$ ground state consists of two hyperfine levels, $F = 1$ and $F = 2$. Low-field-seeking states that can be trapped in a static magnetic trap are the $m_F = -1$ sublevel of the lower hyperfine state $F = 1$, and the $m_F = +2$ and $m_F = +1$ sublevels of the upper hyperfine state $F = 2$. The inset is a zoom-in on the low-field splitting of the $F = 2$ state.

transition, as indicated on the right-hand side of Fig. 3.1. This laser pumps the atoms to the upper $5^2P_{3/2}$, $F = 2$ level from which they can fall back into the $F = 2$ ground state, and therefore are back in the cycling transition.

As we later intend to magnetically trap the atoms in the $m_F = +2$ sublevel of the $5^2S_{1/2}$, $F = 2$ state, we need to be able to pump them into this sublevel. For this purpose, an optical pumping beam is tuned to the $5^2S_{1/2}(F = 2) \rightarrow 5^2P_{3/2}(F = 2)$ transition. Lastly, absorption imaging is carried out on the trapping transition with zero detuning. Both laser frequencies, optical pumping and detection, are indicated on the right-hand side of Fig. 3.1. All optical properties of the $5^2S_{1/2}(F = 2) \rightarrow 5^2P_{3/2}(F = 3)$ transition can be found in Table A.2 in the appendix.

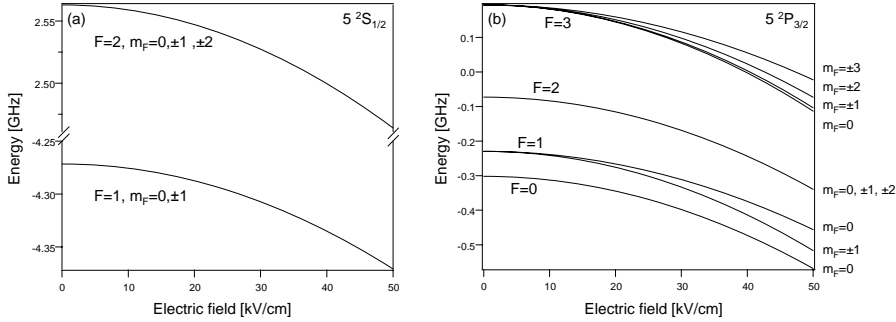


Figure 3.3: Stark effect of ^{87}Rb . Plotted is the Stark energy in GHz versus the electric field in kV/cm. The Stark energy of the $5^2S_{1/2}$ ground state is shown in (a), where all sublevels of the $F = 1$ and $F = 2$ hyperfine states are degenerate. In (b) the energy of the $5^2P_{3/2}$ state is plotted illustrating how most of the sublevels are split. Note that sublevels with the same m_F but different sign are degenerate.

3.1.2 Zeeman effect of ^{87}Rb

In weak magnetic fields the Zeeman sublevel splitting can be described using Eq. 2.2. For strong magnetic fields, F is no longer a good quantum number and the levels split according to their J and m_J values (Paschen-Back regime). For intermediate fields it is difficult to determine the splitting, but for the ground state the Breit-Rabi formula can be used to calculate the energy shift [146, 147]. This formula was used to calculate the energy of the ^{87}Rb $5^2S_{1/2}$ ground state shown in Fig. 3.2. To magnetically trap ^{87}Rb , one needs to identify the low-field-seeking states, i.e., the states where the Zeeman energy is rising with increasing field strength. As can be seen from Fig. 3.2, in the lower hyperfine state $F = 1$ only the upper level $m_F = -1$ is low-field seeking for low magnetic fields. For higher fields the curve bends down and the state becomes high-field seeking. In the upper state $F = 2$ there are two low-field-seeking states, $m_F = +1$ and $m_F = +2$. From these two states it is preferable to magnetically trap the $m_F = +2$ sublevel as its Zeeman shift is larger, and therefore an atom in this state experiences a deeper trapping potential compared to the $m_F = +1$ sublevel. Furthermore, it is easy to optically pump the atoms into the $m_F = 2$ stretched state. Also, in this doubly polarized state spin-exchange collisions do not occur because two $m_F = +2$ states cannot scatter to any other channel that has the same projection of the total angular momentum F [148]. Alkali atoms meet these criteria, and are by far the most widely-studied atoms in the ultracold regime.. For even higher fields the sublevels group according to their m_J values, which is not shown here because such high fields are not applied in our experiment.

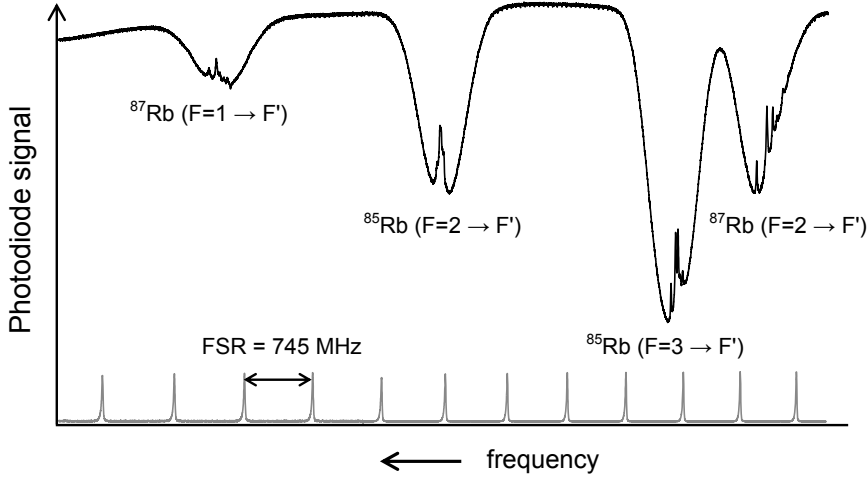


Figure 3.4: Doppler-free absorption spectrum of rubidium at 780 nm. The spectrum is obtained with the cooling laser using saturated absorption spectroscopy. Shown are the $5^2S_{1/2}(F=1) \rightarrow F'$ and $5^2S_{1/2}(F=2) \rightarrow F'$ lines for ^{87}Rb and the $5^2S_{1/2}(F=2) \rightarrow F'$ and $5^2S_{1/2}(F=3) \rightarrow F'$ lines for ^{85}Rb . In the lower part the transmission curve of the Fabry-Perot interferometer is shown indicating that the laser is running in single mode. The free spectral range (FSR) of the Fabry-Perot interferometer is 745 MHz.

3.1.3 Stark effect of ^{87}Rb

Rubidium has a second order Stark effect. For small electric fields, i.e., when the shift due to the external electric field is small compared to the hyperfine splitting, an analytic expression can be derived to calculate the energy shifts [147]. For higher fields, the levels split according to their m_J values, which will not be discussed here. In Fig. 3.3 the level splittings of the $5^2S_{1/2}$ and the $5^2P_{3/2}$ states are shown. All levels are high-field seeking, i.e., the Stark energy is decreasing with increasing field strength. In the ground state, all sublevels of each hyperfine state are degenerate. In the $5^2P_{3/2}$ state, the sublevels of each hyperfine state are split, but levels with the same $|m_F|$ value are degenerate. As all levels are high-field seeking, it is impossible to trap rubidium in a static electric trap; an electrodynamic trap must be used instead.

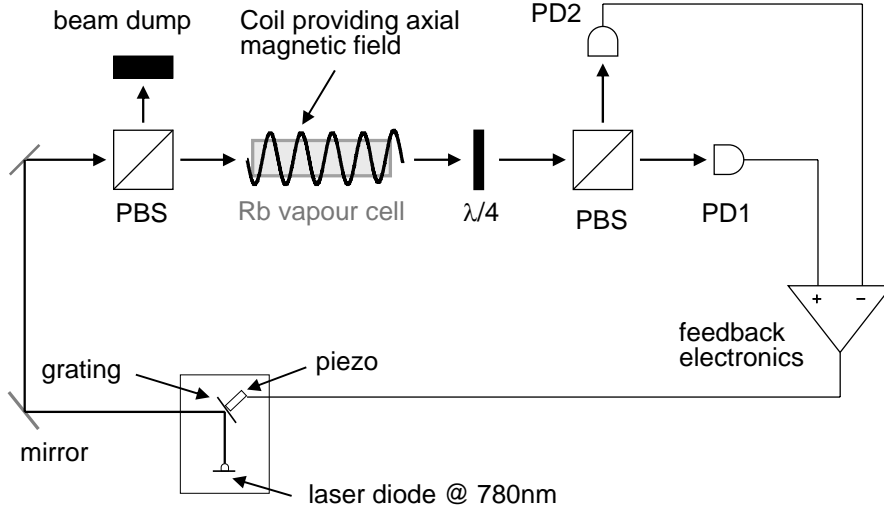


Figure 3.5: Setup of the DAVLL spectroscopy. The light from the master laser is sent to through a cleaning PBS. Then it passes through a rubidium vapor cell with an axial magnetic field followed by a $\lambda/4$ plate. The beam is split by a PBS and sent to two photodiodes, PD1 and PD2. The signals of the two photodiodes are subtracted from each other resulting in a curve with a zero crossing where the frequency is locked at.

3.2 Laser system

3.2.1 Laser locks

Two laser frequencies are needed in the experiment, one for the cooling transition and one for the repumping transition. The wavelengths can be readily obtained using commercially available diode lasers at 780 nm. The trapping light comes from a commercial tapered amplifier system (Toptica, TA 100). The light from a grating-stabilized laser diode (30 mW output) is injected [149] into a tapered amplifier chip where it is amplified to about 500 mW. The repumper laser is a DL 100 (Toptica) with an output power of about 40 mW. In both systems, an optical isolator is placed behind the diodes. This prevents the laser light from being reflected back into the diode which could damage it. The Doppler-free absorption spectrum of rubidium is illustrated in Fig. 3.4. The spectrum was recorded using a simple saturation spectroscopy setup [150], where a strong pump laser beam is sent through a vapor cell containing both rubidium isotopes. A counterpropagating weak ‘probe’ beam is sent to a photodiode resolving the Doppler-free spectrum. Only at the transition frequency, both the pump laser and the probe laser interact with the same velocity group

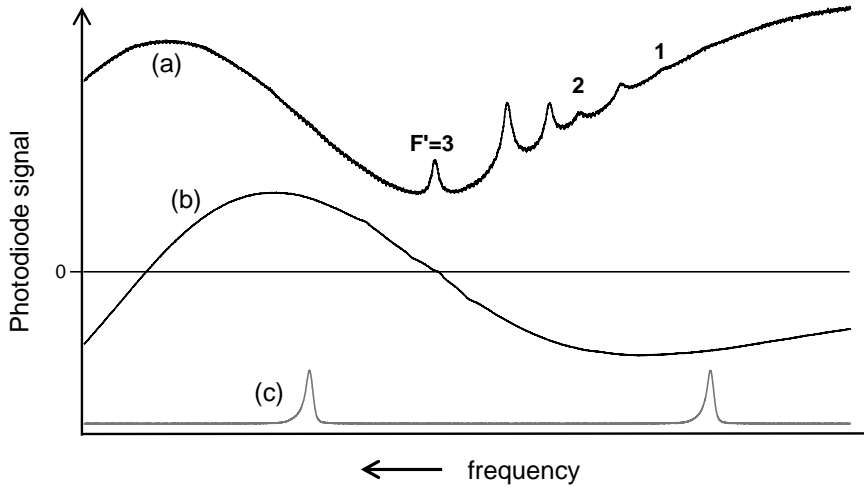


Figure 3.6: (a) Doppler-free spectrum of the cooling transition $5^2S_{1/2}(F = 2) \rightarrow F'$ of ^{87}Rb . The numbers on top of the peaks indicate to which upper hyperfine level they belong to. The peaks in between the pure lines are the crossover peaks. (b) DAVLL signal, the laser is locked to the zero-crossing which coincides with the $F = 2 \rightarrow F = 3$ transition. (c) Transmission signal of a Fabry-Perot interferometer with a FSR of 745 MHz.

of atoms, namely those that have zero velocity along the laser beam axis. Due to saturation by the pump beam, there is a reduced absorption of the probe beam at this frequency resulting in small dips in the Doppler-broadened signal. The whole spectrum spans over about 7.5 GHz, thus in Fig. 3.4 we see from the left to the right: the (repumping) transition $F = 1 \rightarrow F'$ of ^{87}Rb , then the (repumping) transition $F = 2 \rightarrow F'$ of ^{85}Rb , further to the blue the $F = 3 \rightarrow F'$ (cooling) transition of ^{85}Rb and the $F = 2 \rightarrow F'$ (cooling) transition of ^{87}Rb .

Both lasers have to be frequency stabilized which is a prerequisite for stable trapping in a magneto-optical trap. The cooling light is locked using a dichroic-atomic-vapor laser lock (DAVLL) [151]. In this technique the Zeeman effect is employed to generate an error signal about a Doppler-broadened atomic resonance. The setup for this lock is shown in Fig. 3.5. A small part of the laser light emitted by the diode is split off, while most of the light is injected into the tapered amplifier chip. First, this beam is sent through a polarizing beamsplitter cube (PBS) to make sure that its polarization is clean. Then the beam passes through a vapor cell that has a magnet wire coil wrapped around it. This coil generates a constant magnetic field along the beam axis (≈ 90 G). In the presence of a uniform magnetic field the central frequency of circularly polarized light is shifted towards higher (lower) frequencies for σ^-

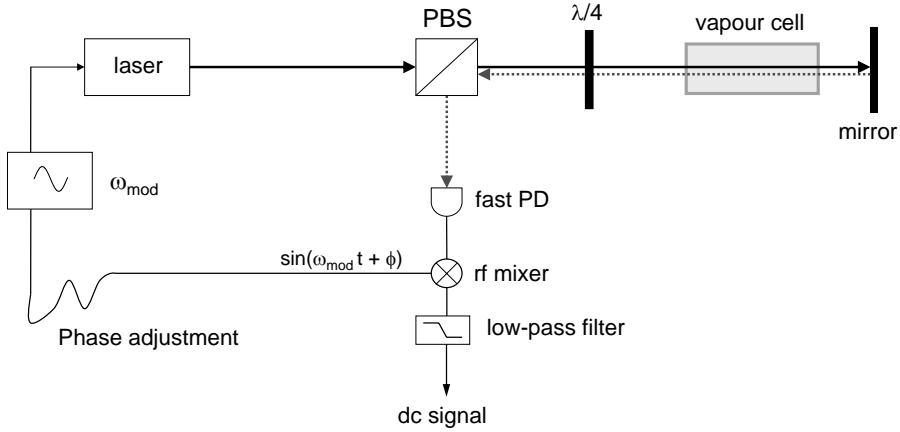


Figure 3.7: The light from the repumper laser which is modulated with an external rf frequency is sent to a saturation spectroscopy setup consisting of a PBS, a rubidium vapor cell and a $\lambda/4$ plate. Then, the signal of a fast photodiode is mixed with the rf oscillator signal and filtered by a low-pass filter. The laser is locked to the resulting dc signal, and the feedback signal is sent to the piezo of the grating.

(σ^+) light. To split the light into its two circular components, the beam is then sent through a quarter-wave plate and through another polarizing beamsplitter. The σ^- - and σ^+ -polarized beams are detected by two photodiodes (Thorlabs, PDA 55). A simple electronic device subtracts the two photodiode signals from each other, resulting in an error signal which can be used to lock the laser. This signal is then sent to a home-built proportional-integral-derivative (PID) regulator which actuates the piezo that controls the grating of the laser.

Figure 3.6 (a) shows the saturated absorption spectrum of the $F = 2 \rightarrow F'$ transitions recorded using the cooling laser. All hyperfine transitions are resolved, and the corresponding F' is indicated on top of the peaks. Peaks in between the pure lines are so-called crossover lines which are always located in the middle of two pure lines (provided these have a common ground-state level). The laser is locked to the $F' = 3$ pure line, which is the zero-crossing of the DAVLL signal (b). A Fabry-Perot interferometer is used to ensure that the laser is running in single mode; the Fabry-Perot transmission is shown in Fig. 3.6 (c).

The repumper laser is locked using frequency-modulation (FM) spectroscopy [152]. The setup is shown in Fig. 3.7. The current of the laser diode is modulated with a radio frequency, in our case 20 MHz. If the optical carrier frequency is ω_0 and the laser light is modulated with the rf frequency ω_{mod} of an external rf source with amplitude A_{mod} , the FM spectrum of the laser

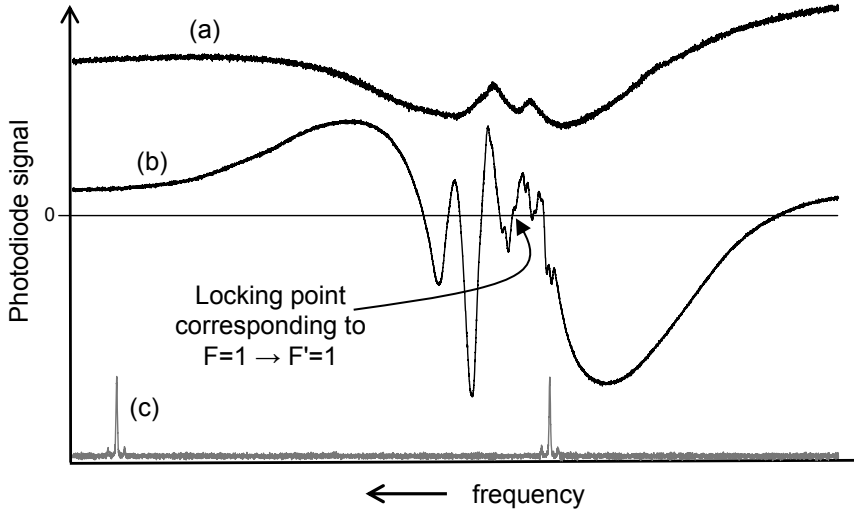


Figure 3.8: Doppler-free spectrum of the $F = 1 \rightarrow F'$ transitions of ^{87}Rb . The middle curve shows the FM spectrum. In principle it is possible to lock the laser to all the zero-crossings of the FM spectrum. In the lower part the transmission curve of the Fabry-Perot interferometer is shown.

is $E(t) = E_0 \exp(i\omega_0 t + iA_{\text{mod}} \sin \omega_{\text{mod}} t)$. The FM modulated laser beam is then sent to a rubidium vapor cell. Absorption and dispersion in the vapor cell will be different for ω_0 and ω_{mod} . After being deflected out of the vapor cell, the beam is sent to a fast photodiode (EOT, ET-2030A). The photodiode signal is then mixed with the original rf signal and filtered by a low-pass filter. The phase between the external oscillator and the modulated signal can be adjusted using a phase shifter. Depending on this phase the error signal is either an absorption or a dispersion signal, i.e., the output of the mixer is proportional to the amplitude of that part of the signal which is in phase with the rf oscillator. In this setup the rf signal generation, the mixer and the phase adjustment are provided by a commercial module from Toptica (Pound-Drever detector, PDD 100). The resulting error signal is fed into a PID regulator (Toptica, PID 100) which controls the piezo of the grating.

Figure 3.8 (a) shows the saturated absorption signal of the repumping transition. The locking signal is shown in (b), and usually the laser is locked to the $F = 1 \rightarrow F' = 1$ transition. Note the small sidebands appearing next to the transmission peaks of the Fabry-Perot interferometer (c). These sidebands originate from the 20-MHz rf signal.

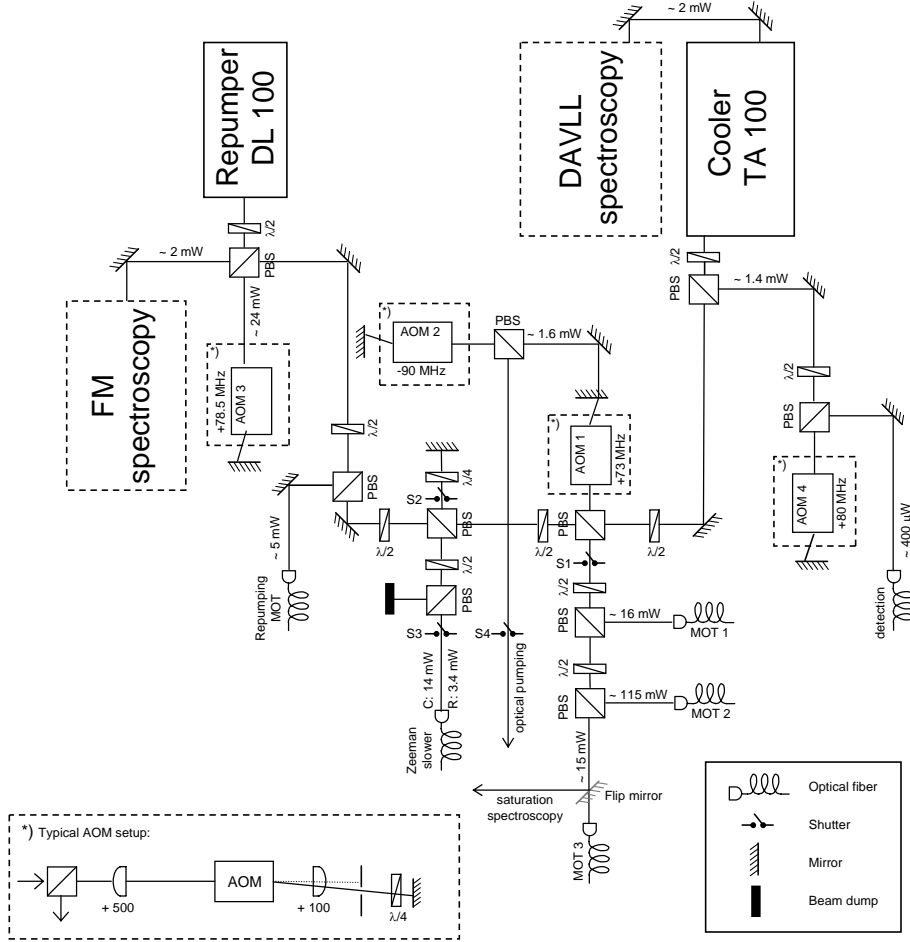


Figure 3.9: Schematic view of the setup on the optical table. Two lasers are used to create the desired beams, on the upper right the ‘cooler’ which is used to drive the cooling transition and on the upper left the ‘repumper’. The inset on the lower left shows the AOM setup which is used for all AOMs, but left out in the big diagram for simplicity. The frequencies the AOMs are driven at are labelled with + or -. This indicates if the selected first order is positive (i.e., shifted to the blue) or negative (i.e., shifted to the red). For all beams, the power injected into the polarization-maintaining fibers is indicated. Between 50% and 75% of this power can be coupled into the fiber and guided to the experiment.

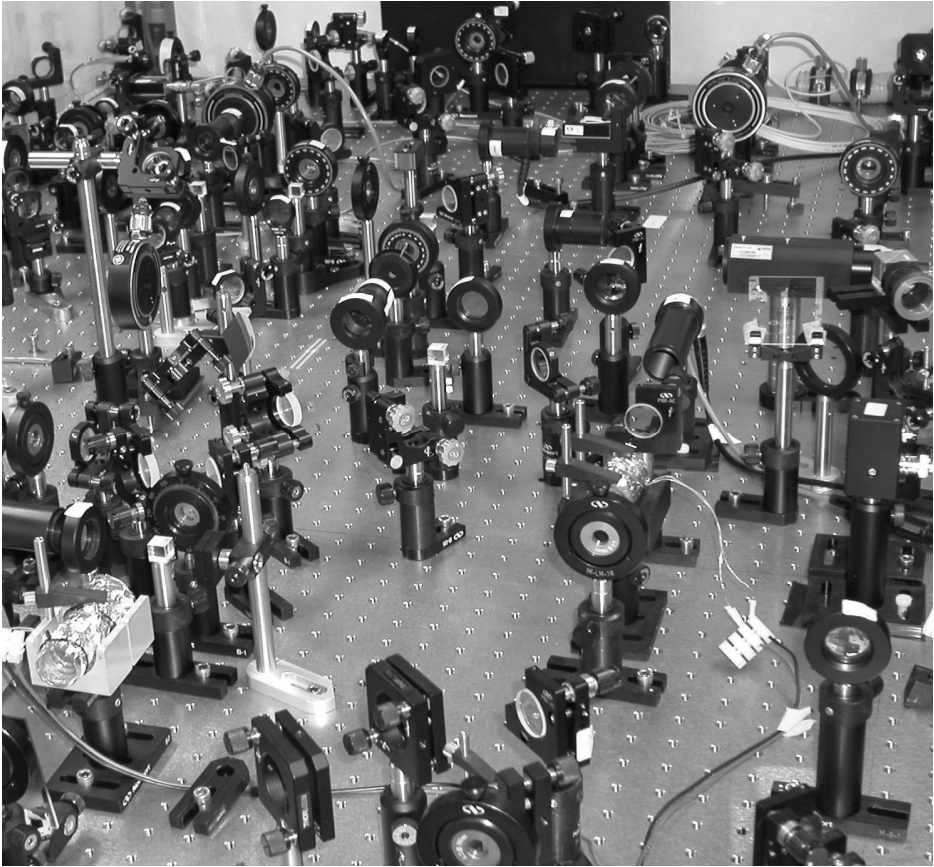


Figure 3.10: Photograph of the setup on the optical table, as seen from the laser end of the table.

Purpose	Transition of the D_2 line	Detuning (MHz)	Power (mW)
Cooling transition (MOT)	$F = 2 \rightarrow F = 3$	-14 to -35	95
Cooling transition (ZS)	$F = 2 \rightarrow F = 3$	-160	10
Repumper (MOT)	$F = 1 \rightarrow F = 2$	0	3.2
Repumper beam (ZS)	$F = 1 \rightarrow F = 2$	0	2.2
Probe beam	$F = 2 \rightarrow F = 3$	0 to -40	0.2
Optical pumping	$F = 2 \rightarrow F = 2$	0, fixed	0.8

Table 3.1: Overview of the transitions used in the experiment; ‘ZS’ denotes ‘Zeeman slower’.

3.2.2 Laser beam generation

To perform the experiment, a number of different beams and frequencies are needed. Table 3.1 gives an overview of the different beams, frequencies, detunings and powers which are employed in the experiment. For both the MOT and the Zeeman slower a cooling and a repumping beam are needed. Furthermore, a probe beam for absorption imaging and an optical pumping beam are used. Figure 3.9 shows a schematic of the beam generation on the optical table, while Fig. 3.10 is a photograph of the optics on the table. The light coming from the cooler and repumper lasers is split up into different beams. With the exception of the optical pumping beam, all laser beams are coupled into polarization-maintaining optical fibers (OZ Optics, PMJ-3A3S-780/125-3-10-1) before they are sent to the experiment. Most of the beams are shifted in frequency using acousto-optical modulators (AOMs). A typical AOM setup is shown in the inset of Fig. 3.9. It consists of a polarizing beamsplitter (PBS), two lenses to focus the beam into the AOM, a $\lambda/4$ plate, and an iris to dump unwanted orders from the AOM. For the experiment, only the first order is used, either blue detuned or red detuned, while the other orders are blocked. All AOMs (ISOMET, 1205C-2) are connected to tunable rf drivers (ISOMET, D322B) with a frequency range between 57 and 103 MHz.

The cooling laser (located at the top right in Fig. 3.9) is locked 160 MHz to the red of the $5^2S_{1/2}(F = 2) \rightarrow 5^2P_{3/2}(F = 3)$ transition. The output of the tapered amplifier chip is split into three parts. The primary beam is used for cooling in the MOT. It is sent through an AOM, labelled *AOM1* in the figure. *AOM1* is running at 73 MHz, and the first order to the blue is used in double-pass configuration. Therefore, the final detuning of the MOT cooling light is $-160 + 2 \times 73 \text{ MHz} = -14 \text{ MHz}$. The beam is then split into three, injected into fibers (*MOT1*, *MOT2*, and *MOT3*), and sent to the experiment. The second beam is used for the cooling transition in the Zeeman slower, and is 160 MHz red detuned from the cooling transition. This beam is overlapped with a part of the repumper light before the two beams are injected into the Zeeman slower fiber. The third beam is used for detection and has only little

power (≈ 1.4 mW). It goes through *AOM4* driven at 80 MHz. The positive first order is employed, such that after the usual double pass the atoms are probed directly on resonance. The beam is then injected into a fiber.

All mirrors on the optical table have a reflectivity of about 98%. Therefore, a tiny part of any beam is transmitted by each mirror. To produce the frequency needed for optical pumping, the transmission leak of the mirror behind *AOM1* is used. Although this beam is weak (only 1.6 mW of the light are not reflected by the mirror), it has enough power to saturate the transition used for optical pumping. This $F = 2 \rightarrow F = 2$ transition is separated from the $F = 2 \rightarrow F = 3$ transition by 267 MHz. Therefore, we shift the leakage beam by 2×-90 MHz using *AOM2*. This gives a total detuning of $-160 + 1 \times 73 - 2 \times 90$ MHz = -267 MHz, exactly on resonance with the optical pumping transition. This beam is directly guided to the experiment without being coupled into a fiber.

As mentioned above, the repumper laser is locked to the $F = 1 \rightarrow F = 1$ transition using FM spectroscopy. The repumper light not used for the spectroscopy is directed to *AOM3* which shifts it to the blue by $2 \times 78.5 = 157$ MHz. As the hyperfine splitting between the $F = 1$ and $F = 2$ excited state levels is 157 MHz, the repumper light used for the experiment is on resonance with the $F = 1 \rightarrow F = 2$ transition. Afterwards, the beam is split into two parts. One is coupled into a fiber and then sent to the MOT, the other one is overlapped with the cooler beam for the Zeeman slower.

During the experimental sequence, it is sometimes necessary to switch off the laser beams very quickly, i.e., within μ s. The light can be switched off with the AOMs which typically block the laser light within 5 to 10 μ s. However, AOMs never completely extinguish a laser beam, and a leakage beam in the nW-power range is always left. Therefore, three mechanical shutters *S1*, *S2*, and *S3* (Uniblitz, LS6S2, LS6ZM2, and LS6T2) are inserted in the laser beams to be able to completely switch off the light. These shutters have an opening diameter of 6 mm, and close within three ms. Another shutter (Melles Griot, 04 IES 211) with an opening diameter of 25.4 mm is inserted in the path of the optical pumping beam (*S4*) just before it is sent to the MOT glass cell.

The MOT cell and all vacuum components are set up on a rigid aluminum frame consisting of modular components (BOIKON), which we call the ‘experimental’ table. It has two levels: on the upper level four of the MOT beams are generated (see Fig. 3.11 (a)) and then directed to the lower level where all vacuum parts are located (see Fig. 3.11 (b)). The light is sent to the experimental table via the polarization-maintaining fibers. All MOT beams are expanding according to the numerical aperture of the fibers. At the appropriate distance, a lens (with a focal length of 100 mm) is put in to create a collimated beam with a FWHM of 1.2 cm. This is illustrated in the inset in Fig. 3.11 (a).

The light from fiber *MOT2* is coupled out on the upper level and is used to generate the four beams in the horizontal symmetry plane of the MOT. As schematically drawn in Fig. 3.11 (a), this beam is split into four intensity-balanced beams. Of these four beams, two counterpropagating beams (beams

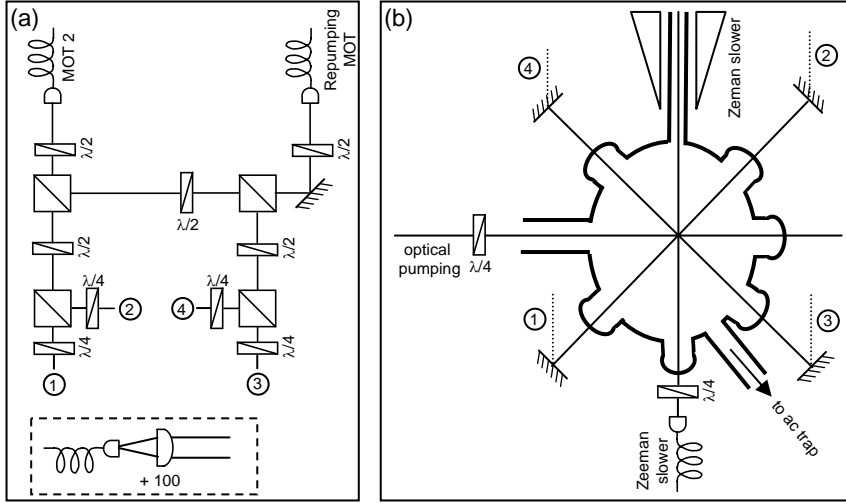


Figure 3.11: Scheme of the optical setup on the experimental table. (a) Arrangement of the MOT beams on the upper level. (b) Top view of the different beams that enter the glass cell on the lower level. At locations 1 to 4, the laser beams are sent down from the upper to the lower level.

3 and 4) are overlapped with the light from the repumper fiber which is also expanded to a full width at half maximum (FWHM) of 1.2 cm. All the beams pass through $\lambda/4$ plates to acquire the correct circular polarization needed for the MOT. Then, the light is sent through the glass cell as indicated in Fig. 3.11 (b) which shows the top view of the lower level. The two beams from the top and from the bottom, i.e., along the magnetic field axis, are not drawn (fibers *MOT1* and *MOT3*).

The light for the Zeeman slower is also sent through a $\lambda/4$ plate before it enters the glass cell towards the Zeeman slower. The Zeeman slower beam has a FWHM of about 7 mm at the lens, and is focussed such that about 150 cm downstream it reduces to a FWHM of 2 mm (i.e., at the location of the differential pumping tube between the source chamber and the Zeeman slower). The Zeeman slower beam is thus expanding the same way as the atomic beam from the source to the MOT chamber. Additionally, the Zeeman slower beam is sent through the cell slightly higher than the center of the MOT to disturb the atoms as little as possible during loading. The optical pumping beam is sent through the cell perpendicularly to the Zeeman slower beam. It is also circularly polarized with respect to an additional magnetic bias field along the beam axis.

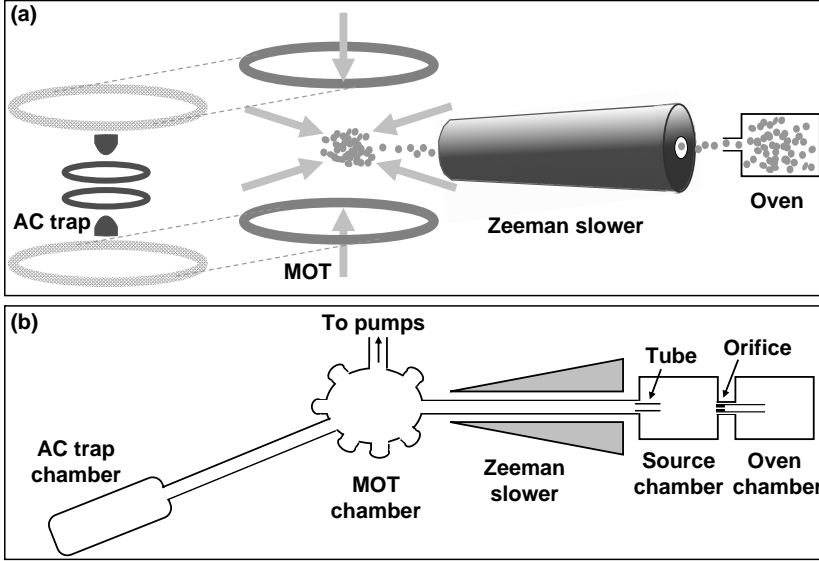


Figure 3.12: Schematic of the experimental setup. (a) The main components of the experiment are the rubidium oven, the Zeeman slower, the MOT, and the ac electric trap. (b) The associated vacuum chambers: oven chamber, source chamber, a glass cell where the MOT is created, and another glass cell housing the ac trap.

3.3 Vacuum system

Every time a cold atom cloud is created and imaged, a sequence of experimental steps is performed. The experiment is starting from a rubidium oven which serves as a source for the atomic beam. The atoms are decelerated in a Zeeman slower, and cooled and trapped in the MOT, as shown in Fig. 3.12 (a). They are loaded into the magnetic trap by ramping up the current in the quadrupole coils. Then, they are transferred to a second vacuum chamber housing the ac trap by physically moving the quadrupole coils [129]. The experimental setup consists of four vacuum chambers, as schematically drawn in Fig. 3.12 (b). The first chamber contains the rubidium oven. The gaseous rubidium effuses through an orifice into the second chamber, which we call the source chamber. It is connected via a small tube to the third chamber where the atoms first pass through Zeeman slower before they are collected in the MOT. The fourth chamber houses the ac trap and is connected to the MOT chamber via a CF-16 bellows. All chambers were brought to ultrahigh vacuum with a pressure of 10^{-9} mbar or lower. The fully assembled vacuum system was baked over several days at temperatures of 180°C to 200°C to achieve the low pressures

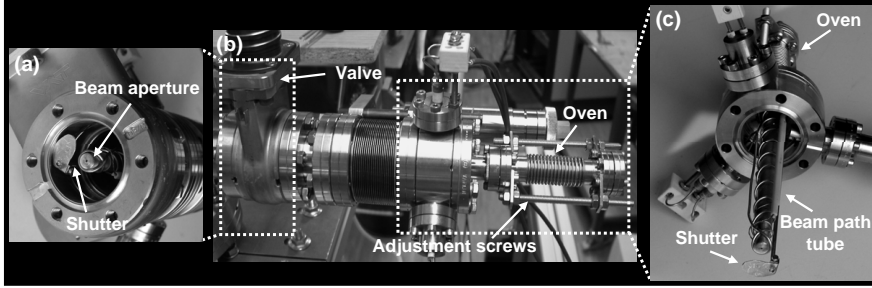


Figure 3.13: Photograph of the vacuum parts containing the rubidium oven. (a) Close-up of the 1-mm aperture where the effusive beam enters the source chamber. The aperture can be covered with a mechanical shutter. (b) Side view of the vacuum system housing the oven. The long adjustment screws are used to change the length of the oven chamber. The valve separates the oven chamber from the source chamber. (c) Copper tube where the rubidium beam is formed. A wire is wound around the long tube heating it while the experiment is running. The aperture described in (a) is visible at the end of the tube.

needed in cold atom experiments.

3.3.1 Rubidium oven and source chamber

The oven chamber in which the rubidium beam is produced, is shown in the photograph in Fig. 3.13. A rubidium dispenser could be used as an alternative to the oven, but in that case the beam flux would be smaller. The oven chamber consists of a bellows whose length can be changed using the long adjustment screws, as seen on the right in picture (b). Initially, to bring rubidium into the vacuum, an evacuated glass ampule containing 1 g of metal rubidium (Alfa Aesar, Rubidium 99.75% in breakseal ampule) was placed in the oven chamber. The chamber was pumped to a vacuum better than 10^{-8} mbar such that the rubidium could no longer react with the background gas. Then, the length of the bellows was shortened using the adjustment screws. In this way the breakseal glass ampule was broken when it was squeezed together by the bellows releasing rubidium. The oven chamber is connected to the source chamber via a copper tube, as shown in the picture (c). A small reducer is inserted into this copper tube to generate the effusive rubidium beam. It has a length of 2.75 mm, and its aperture has a diameter of 1 mm. Figure 3.13 (a) shows a close-up of the aperture. A mechanical shutter can be placed in front of the opening which is visible in Figs. 3.13 (a) and (c). By heating the oven chamber to 80–140°C (typically 130°C) every time the experiment is run, the rubidium starts to evaporate. To heat the oven, a heating tape is wrapped around the

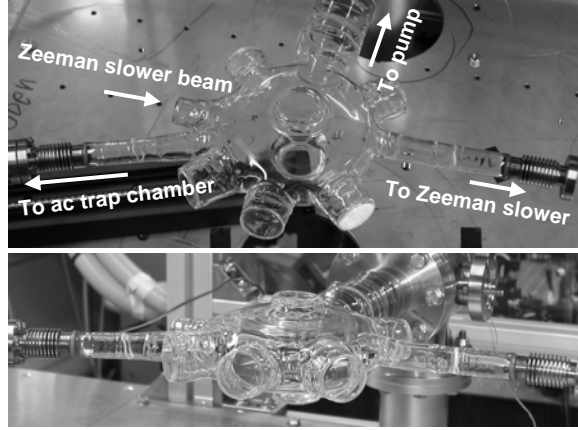


Figure 3.14: Photograph of the glass cell where the MOT is created. The MOT beams pass through the large 30-mm viewports of the cell.

bellows. Additionally, the copper tube is heated by sending a current through the wire wound around it, as shown in Fig. 3.13 (c). The oven chamber is separated from the source chamber by a valve which can be closed if the source chamber is vented.

The source chamber is pumped by two pumps, an ion pump (Varian Star Cell) and a titanium sublimation pump (VG, ZST22). Additionally, a cold finger is implemented to further improve the vacuum. It consists of a copper block which is cooled with liquid nitrogen. While the ion pump is always on, the sublimation pump is turned on once or twice every week for about 2 minutes. The pressure in the source chamber is in the low 10^{-9} mbar range.

3.3.2 MOT chamber and ac trap chamber

The source chamber is connected to the third, so-called MOT chamber via a differential pumping tube with an opening of 5 mm in diameter and a length of 6 cm. A pneumatic valve separates the two chambers which can be closed if one of the chambers needs to be vented. The beam passes through a non-magnetic stainless steel tube inside the Zeeman slower until it reaches the MOT chamber. The MOT is created in a quartz glass cell which is shown in Fig. 3.14. The glass cell has six viewports in the horizontal plane, and two 30-mm viewports at the top and at the bottom, all used for various laser beams. In the plane, four 30-mm viewports are used for the MOT beams, one 20-mm viewport for the Zeeman slower beam (as indicated in Fig. 3.14), and another 30-mm viewport can potentially be used for probing. There are three arms which connect the glass cell to the source chamber, to the fourth chamber (ac trap chamber), and

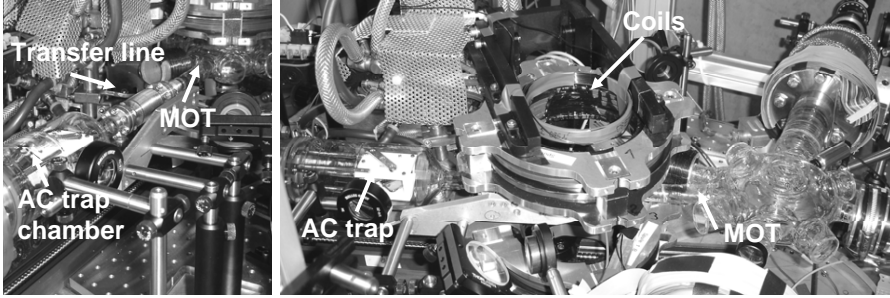


Figure 3.15: Photograph of the transfer line which brings the atoms from the MOT chamber to the ac trap chamber. The photograph is taken at the moment when the magnetic trap is about halfway from its starting point (the MOT cell) to its final destination (the ac trap cell).

to the pumps via glass-to-metal transitions.

The transfer line that connects the MOT chamber to another quartz glass cell housing the ac trap is shown in the photograph in Fig. 3.15. It consists of a small CF-16 tube and a bellows, both made out of non-magnetic stainless steel.

The MOT chamber and the ac trap chamber are pumped by two pumps, an ion pump (Varian Star Cell) and a titanium sublimation pump (VG, ZST22). Two ion gauges (Leybold Heraeus, Ionivac IM 15 and Varian, Multi Gauge L8350-301) are flanged to the system for monitoring the pressure. All pumps and ion gauges are connected to the system via the back arm of the MOT cell, as indicated in Fig. 3.12 (b) and Fig. 3.14.

The pressure in the MOT chamber is usually around 1×10^{-10} mbar, measured by the Leybold ion gauge which is about 50 cm away from the center of the glass cell. When the rubidium oven is heated to 140°C , the pressure rises to about 2×10^{-10} mbar. These low-pressure values were achieved after baking out the MOT chamber over several days at a temperature of 200°C . The titanium sublimation pump is switched on once a week for two minutes, and the ion pump is always on.

We are not able to measure the pressure in the ac trap chamber directly, but we know from lifetime measurements that it is about a factor of three higher than in the MOT chamber. This difference in pressure between the two chambers can be attributed to two factors. Firstly, the pumps are far away and the diameter of the tube between MOT and ac trap chambers is small. The ac trap chamber is therefore not pumped efficiently. Secondly, the ac trap assembly is made out of steel and ceramics. These materials can outgas and deteriorate the vacuum.

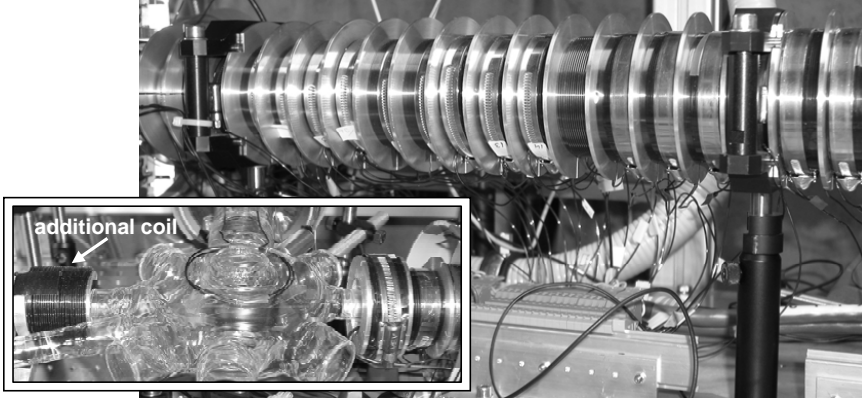


Figure 3.16: Photograph of the Zeeman slower. The inset shows a close-up of the MOT glass cell where the last three coils of the Zeeman slower are visible on the right. On the left of the MOT glass cell, an additional coil is placed which compensates for the stray fields of the Zeeman slower coils.

3.4 Magnetic field generation

3.4.1 Zeeman slower

The Zeeman slower in our experiment is used in the spin-flip configuration. It consists of 28 coils, all with a different number of windings. In this way, it is possible to connect several coils in series with one power supply. Although the same current is flowing through all of them, the magnetic field of each coil is different according to its number of windings. The number of windings varies between 29 and 394. Figure 3.16 shows a photograph of the Zeeman slower. Each coil has a width of 23.5 mm and is separated from the next coil by a thin aluminum disk which has a width of 2.5 mm. Altogether, the Zeeman slower is 73 cm long. The magnet wire used for the coils has a diameter of 1.25 mm, and is wound around an aluminum cylinder with an outer diameter of 2.25 cm. The vacuum tube for the atomic beam is placed inside this cylinder.

In a Zeeman slower consisting of several individual coils (in this case 28) the current in each coil can be adjusted separately. This is an advantage compared to a Zeeman slower consisting of one single coil where the number of winding varies over the length of the slower. The latter type of Zeeman slower is also used very often. The magnetic field in a Zeeman slower consisting of individual coils is inherently not completely smooth, but it is composed of discrete steps from coil to coil. However, this has only a negligible effect on the overall performance.

Figure 3.17 shows the field in the Zeeman slower. The straight line is the

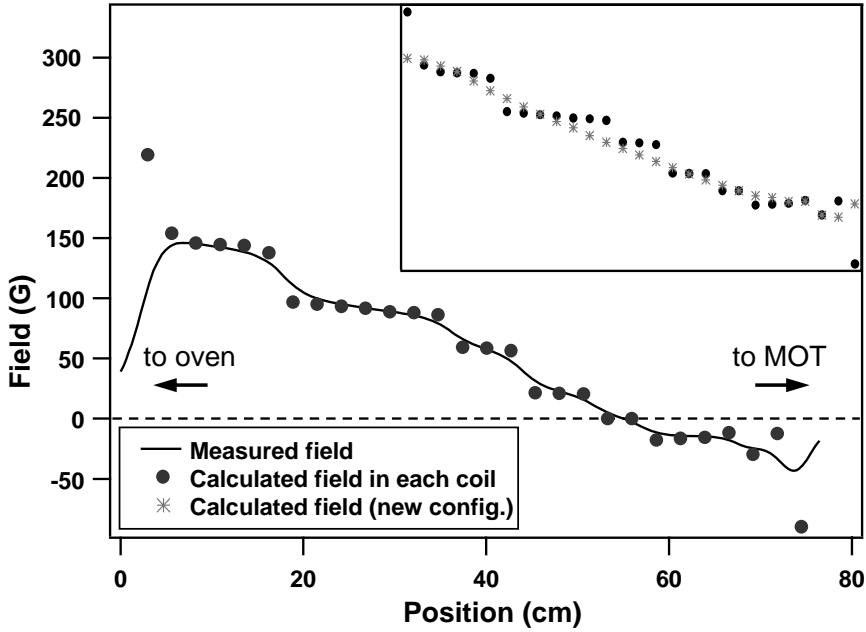


Figure 3.17: Magnetic field in the Zeeman slower. The black line shows a field measurement with a Hall probe. The black round dots are the central fields in each coil as calculated from the number of windings and the current. The grey asterisks in the inset are the calculated central fields with the coils connected to a new power supply, leading to a much smoother field.

field as measured with a Hall probe (Lake Shore, 421 Gaussmeter). At the time when this measurement was performed, the 28 coils were divided into eight groups, each connected to a different power supply. Therefore, the curve is not perfectly smooth but it has plateaus, especially at the beginning of the Zeeman slower (i.e., around a position of 10 to 30 cm in the graph) where a lot of coils were connected to the same power supply. This is more pronounced when plotting the central field in each coil as calculated from the number of windings and the current running through the coil (black round dots in the plot). Two coils are set to zero current to create the zero field needed in a spin-flip configuration (at a position of 55 cm in the graph). The overall measured field is smoother as the field in each coil is also influenced by the field of the neighboring coils. Currently, a new home-built power supply is used, where the current in each coil is adjusted individually. The grey asterisks in the inset show the calculated field of each coil in this new configuration. Compared to the old setting (black round dots), the steps have almost disappeared and the field is smoother. The vacuum has not been broken since then, and therefore

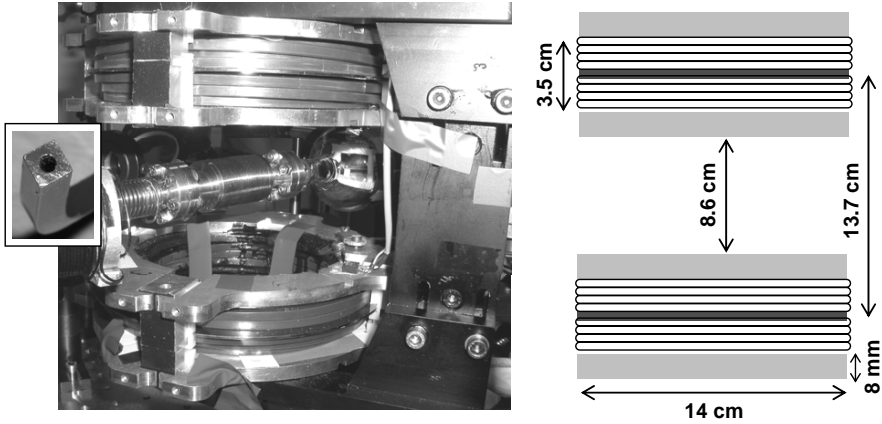


Figure 3.18: Photograph of the pair of coils in anti-Helmholtz configuration. The inset shows the square cross section of the wire which is water cooled through the hole in its middle. The dimensions and distances of the coils are indicated in the schematic on the right.

the field in the new configuration has never been measured. Even though the field should be much smoother with the new setup, the overall performance turned out not to be very different from the former configuration.

To find the correct current settings for the Zeeman slower when it was initially set up, one coil after the other was switched on, starting with the coil which is closest to the MOT. The current was adjusted by improving the fluorescence signal of the MOT on a photodiode. Subsequently, the rest of the coils were gradually turned on and individually adjusted. As the field of the coils closest to the MOT shifts the center of the quadrupole trap, an additional coil is placed on the other side of the glass cell to compensate for the stray field of the Zeeman slower, as shown on the left in the inset of Fig. 3.16.

The magnetic field of the Zeeman slower can be switched off rapidly because each coil is connected in parallel to a transorb diode (Fairchild Semiconductor, 1500 Watt Transient Voltage Suppressor, 1V5KE12CA). A transorb diode has a specified breakdown voltage U_{BD} , in our case 12 V. It consists of two back-to-back Zener diodes connected in series, and it becomes conducting as soon as the voltage is higher than the breakdown voltage U_{BD} . In this way the voltage across the coil remains constant at U_{BD} when the power supply is switched off. The current through the coil I vanishes quickly according to $L * I / U_{BD}$ within some μs .

3.4.2 Quadrupole trap and electronic setup

To trap the low-field-seeking states of rubidium in a magnetic trap, it is necessary to create a field minimum. A number of different traps exists but one of the simplest configurations is a pair of coils through which equal currents are flowing in opposite directions. In this so-called anti-Helmholtz configuration, a quadrupole field is created, where the gradient in the axial direction is twice as large as in the plane, and the field at the center between the coils is zero. Figure 3.18 shows a photograph of our coils. Each coil consists of two individual coils with 15 windings each which are connected in series. They are placed between two aluminum plates that hold the windings together. As seen in the schematic on the right of the figure, the aluminum plates are 8 mm thick and have an outer diameter of 14 cm. The distance between the centers of the two coils is 13.7 cm, and the distance between the two inner aluminum plates is 8.6 cm. The copper wire has a square cross section ($5 \times 5 \text{ mm}^2$) and a hole with a diameter of 2.5 mm, as shown in the inset on the left of Fig. 3.18. The coils are insulated with thin heat shrink tubing to prevent shortcuts between adjacent windings. Together, the coils have a resistance of $R = 22 \text{ m}\Omega$ and an inductance of $L = 220 \text{ }\mu\text{H}$. The windings experience the force of the magnetic field, and although they were tightly held together by the aluminum plates, they moved when the field was abruptly switched. Therefore, they were glued together with an adhesive that now holds them in place (Emerson and Cuming, Stycast 2850 FT).

To create the strong magnetic fields needed for the magnetic trap, high currents of up to 750 A are sent through the wires. Two power supplies (Lambda, ESS 40V 375A) are connected in parallel to generate these high currents. One of the power supplies is used as master and controls the second power supply. The current can be set with an analog output signal from the computer control. The coils need to be cooled, which is done by sending cold water through the hole in the wire. The coils are cooled in parallel. Otherwise, i.e., were the coils cooled in series, the water would already be hot when it arrived to the second coil. Furthermore, the water pressure would not be high enough.

The circuit diagram is schematically drawn in Fig. 3.19 (a). The anti-Helmholtz coils are connected to the positive output of the power supplies. Two semiconductor switches (IGBT, i.e., Insulated Gate Bipolar Transistor), that are connected in parallel, are used to quickly disconnect the coils from the power supplies. The IGBT switches (Semikron Semitrans M, SKM600GA124D) open and close within 100 ns. In the circuit they are inserted between the coils and the negative output of the power supplies. To allow the atoms to ballistically expand in the absence of a magnetic field for subsequent imaging, it is necessary to switch off the fields very quickly, i.e., within less than 0.5 ms. This is difficult as the coil current decreases slowly according to $\frac{dI}{dt} = \frac{U_{\text{ind}}}{L}$ when the fields are switched off. Here, L is the inductance of the coil and U_{ind} the induced voltage. As already explained for the Zeeman slower in Sec. 3.4.1,

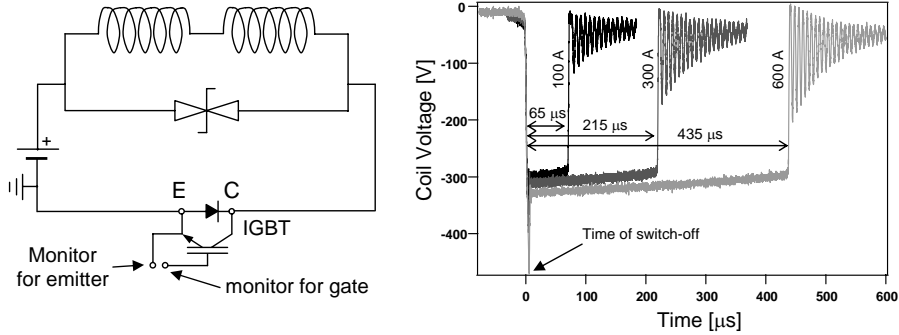


Figure 3.19: (a) Circuit diagram of the quadrupole coils. The anti-Helmholtz coils are connected in parallel with transorb diodes that decrease the switch-off times significantly. A semiconductor device (IGBT) is used to switch. (b) Measured switch-off times for different currents. Measured is the voltage drop across the coils versus the time. At the time of switch-off, i.e., when the IGBT is opened, the induced voltage is held constant by the transorb diodes at -300 V until the power in the coils has dissipated. This switch-off time is proportional to the current.

transorb diodes can be used to minimize the switch-off times. Therefore, ten transorb diodes (MDE Semiconductor, MAX 40 22C) are connected in series and then mounted in parallel to the two coils. Each diode has a breakdown voltage of 30 V, hence the voltage will rise to 300 V with ten diodes in series. When the IGBT switch is opened, the induced voltage will stay constant until the residual power in the coils has dissipated in the transorb diodes. In this way the field decays rapidly. This is shown for three different currents in Fig. 3.19 (b) where the voltage drop across the coils is plotted versus time. By the time the voltage has dropped from -300 V to 0 V, the magnetic field has vanished. For $I = 100$ A the switch-off time is $65 \mu\text{s}$, and for $I = 300$ A the switch-off time is $215 \mu\text{s}$, roughly three times longer, as expected. For $I = 600$ A the switch-off time is $435 \mu\text{s}$, i.e., twice as long as for 300 A.

The gradient in the magnetic trap was measured using a Hall probe. In the symmetry plane the gradient is 18 G/cm for 100 A flowing through the coils. In the axial direction it is twice as large.

The holder of the quadrupole coils is mounted onto a linear translation stage (THK, KR3306A and 600 LPO-0000) which is driven by a servo motor (Mitsubishi HC-MFS13) and computer controlled. The translation stage has a nominal reproducibility of $3 \mu\text{m}$ and a total travel of 511.5 mm. By physically moving the quadrupole trap, the magnetic trap can be transferred to the second vacuum chamber without significant loss in atom number or heating [129].

The stray magnetic field of the quadrupole coils initially magnetized all

parts made of stainless steel that were close to the transfer line. Therefore, aluminum rods are now used for all optics close to the coils. Additionally, μ -metal shields are placed around the translation stage because it is constructed out of highly magnetizable steel.

3.5 Evaporation

When the atoms are in the magnetic trap, the temperature of the trapped cloud can be further reduced by introducing a stage of forced evaporation. The basic idea behind evaporative cooling is to remove the hot atoms and to wait until the ensemble has reached equilibrium at a lower temperature through elastic collisions. This is illustrated in Fig. 3.20 on the left. The process of taking out atoms with subsequent rethermalization is repeated until the desired temperature is achieved. Evaporative cooling was first demonstrated in 1988 on magnetically trapped atomic hydrogen [153]. Evaporative cooling requires the rate of elastic to inelastic collisions to be large enough to allow the sample to thermalize before the number of atoms has decreased due to inelastic collisions. Inelastic collisions can be due to one-body, two-body or three-body processes. One-body losses originate from collisions with the background gas leading to a decrease in the atom number. Two-body losses are mostly suppressed in spin-polarized gases and will not be discussed here. In three-body events, three atoms collide resulting in a diatomic molecule with the residual energy transferred to the third atom. Three-body collisions do not only lead to a loss in atom number but also induce heating. More details can be found in [154]. For an efficient evaporative cooling process, the ratio of elastic to inelastic collisions should be on the order of 100.

We perform rf-induced evaporative cooling. This method exploits the fact that the splitting of the Zeeman levels depends on the position of the atom in the magnetic trap, because the magnetic field increases with the distance from the trap center. This is illustrated in Fig. 3.20 on the right for an atom in the $F = 1$ hyperfine state. If the distance between two Zeeman sublevels coincides with the energy of the rf photons, an atom in the trapped m_F sublevel can be transferred to an untrapped state, i.e., a state that is not low-field seeking and therefore not confined in the trap. Only atoms with high energy reach the outer regions of the trap and are thereby kicked out. In the experiment the rf frequency is ramped down linearly, continuously decreasing the temperature and the cloud radius.

The speed of evaporative cooling is important for its efficiency. If the trap depth is ramped down too quickly, the ensemble does not have time to thermalize, and therefore the process becomes inefficient. When the trap depth is ramped down too slowly, however, inelastic collisions become important and might lead to trap loss. The speed of evaporation can be modelled in a simple way by assuming that any atom with an energy greater than a certain energy

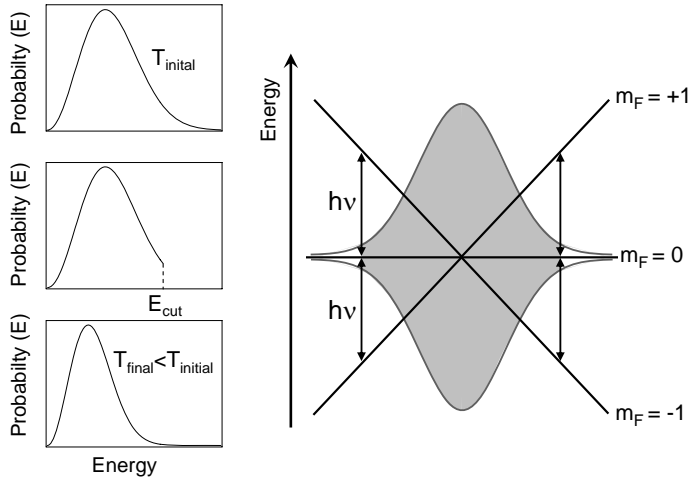


Figure 3.20: Principle of evaporative cooling. The series of plots on the left shows the probability distributions versus the energy. If the tail of the original Maxwell-Boltzmann distribution at a temperature T_{initial} is cut off, the ensemble rethermalizes, and the distribution at the final temperature $T_{\text{final}} < T_{\text{initial}}$ is shifted to smaller energies. On the right, the principle of rf-induced evaporation is illustrated for atoms in the $F = 1$ hyperfine state. Only atoms with high energy enter the region where the distance between the two Zeeman shifted hyperfine sublevels matches the rf energy. By absorbing a rf photon, the atom is transferred to an untrapped state.

ϵ_{evap} is lost. Then, the evaporation rate is equal to the scattering rate to states with energies $> \epsilon_{\text{evap}}$. Using the principle of detailed balance, the evaporation rate Γ_{evap} is given by

$$\Gamma_{\text{evap}} = n(0)\sigma\bar{v}\left(\frac{\epsilon_{\text{evap}}}{k_{\text{B}}T}\right)\exp\left(-\frac{\epsilon_{\text{evap}}}{k_{\text{B}}T}\right), \quad (3.1)$$

where $n(0)$ is the density in the trap center, σ is the collision cross section, and $\bar{v} = \left(\frac{8k_{\text{B}}T}{\pi m}\right)^{1/2}$ is the mean thermal velocity [148]. The decay time τ_{evap} is inversely proportional to the density of the atomic sample, therefore it is important to increase the density of the trapped cloud before the evaporation.

A simple coil with two windings is used as a rf antenna in the experiment, as shown in Fig. 3.21. A magnet wire with a diameter of 1.25 mm is bent into a circle with a diameter of about 7 cm. The rf frequency is generated by a direct digital synthesizer (Stanford Research Systems, DS345), computer controlled via GPIB. The output signal is frequency doubled (Mini-Circuits, FD-2 10813) and then amplified to 1 W (Mini-Circuits, ZHL-32A). For better impedance matching, the output signal of the amplifier is connected in series with a 50- Ω



Figure 3.21: Photograph of the rf antenna. The coil has two loops and is placed directly on top of the glass cell.

resistor. The synthesizer performs a linear ramp which is triggered from the computer. Depending on the rf-frequency range of the ramp and the ramping speed, the sample can be prepared at different temperatures and densities.

3.6 Imaging

3.6.1 Absorption imaging principle

To find out the number and temperature of the atoms, the cloud is imaged using laser absorption. A resonant laser beam is sent through the atom cloud which absorbs the photons. The laser beam has a larger diameter than the cloud, and its intensity is decreased in the center after passing through the cloud. This shadow of the atoms is subsequently imaged onto the CCD chip of a camera. The following relationship holds for the intensity distribution $I(y, z)$ in the laser beam after it traversed the cloud along x :

$$\frac{dI}{dx} = -n(x, y, z) \sigma_{\text{abs}} I. \quad (3.2)$$

$n(x, y, z)$ is the density distribution of the atoms and σ_{abs} is the absorption cross section for low laser intensities:

$$\sigma_{\text{abs}} = \hbar\omega \frac{\Gamma_{\text{sc}}}{I} = \hbar\omega \frac{f \Gamma/2}{I_{\text{sat}}(1 + (\frac{2\delta}{\Gamma})^2)} = \frac{3\lambda^2}{2\pi} \frac{f}{1 + (\frac{2\delta}{\Gamma})^2}. \quad (3.3)$$

f is an average over the Clebsch-Gordan coefficients and depends on the polarization of the light; in our experiment $f = \frac{7}{15}$. The scattering rate Γ_{sc} is given by Eq. 2.10 and the saturation intensity $I_{\text{sat}} = \pi\hbar c/(3\lambda^3\tau)$. Integrating Eq. 3.2 yields

$$I(y, z) = I_0(y, z) e^{-\int \sigma_{\text{abs}} n(x, y, z) dx} = I_0(y, z) e^{-OD(y, z)}, \quad (3.4)$$

where I_0 is the initial intensity of the laser beam. $OD(y, z) = \ln(I_0/I)$ is called the ‘optical density’ and depends on the intensity before transmission, I_0 , and

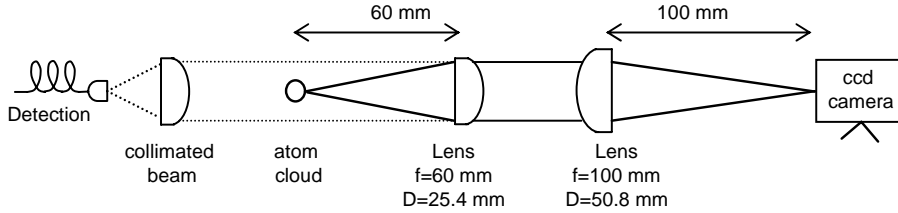


Figure 3.22: Setup for absorption imaging. The collimated beam is sent through the atom cloud and then imaged onto the CCD array of the camera. Two lenses are used, one with a focal length of $f = 60$ mm and a diameter of $D = 25.4$ mm, and the other with $f = 100$ mm and $D = 50.8$ mm.

the intensity after transmission, I . To determine the optical density of the cloud, two pictures are taken. First, a picture I_{atoms} images the shadow of the atoms. Then, a second picture I_{light} is taken with the probe beam on, but in the absence of the atom cloud. For every pixel in the picture the optical density is given by

$$OD(y, z) = \ln \left(\frac{I_{\text{light}}}{I_{\text{atoms}}} \right). \quad (3.5)$$

To find out the number of atoms and the density, a 2D-Gaussian fitting routine is used to determine the dimensions of the cloud in y and z , i.e., σ_y, σ_z . The full width at half maximum Δ_i of the cloud is related to the respective σ_i by $\Delta_i = \sqrt{8 \ln 2} \sigma_i$. The density distribution of the cloud is assumed to be

$$n(x, y, z) = \frac{1}{\sqrt{(2\pi)^3} \sigma_x \sigma_y \sigma_z} \exp \left(-\frac{x^2}{2\sigma_x^2} \right) \exp \left(-\frac{y^2}{2\sigma_y^2} \right) \exp \left(-\frac{z^2}{2\sigma_z^2} \right), \quad (3.6)$$

as already seen in Eq. 2.20. The maximum optical density OD_{max} is also determined from the pictures by averaging the optical density of a square consisting of 25×25 pixels in the center of the cloud.

Using the results from the fit, the atom number N is given by

$$N = 2\pi \frac{\sigma_y \sigma_z}{\sigma_{\text{abs}}} OD_{\text{max}}. \quad (3.7)$$

The peak density n_0 is

$$n_0 = \frac{N}{\sqrt{(2\pi)^3} \sigma_y \sigma_z \sqrt{\sigma_y \sigma_z}}. \quad (3.8)$$

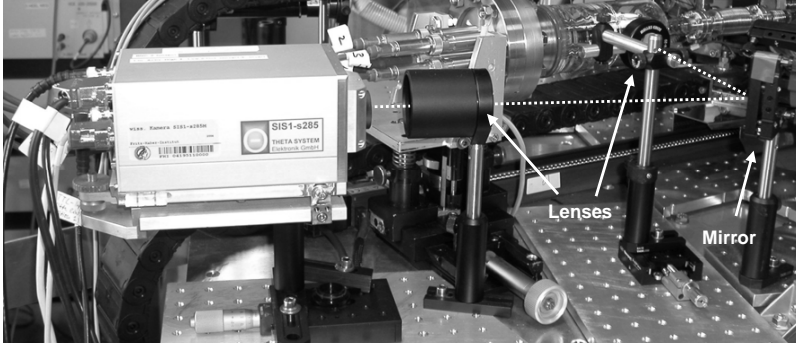


Figure 3.23: Photograph of the experimental setup for imaging the atom cloud. The detection beam (dashed line) is sent through the center of the ac trap and is imaged by the 60-mm lens close to the quartz cell. Then the light is imaged onto the CCD chip with a 100-mm lens. The 45° mirror between the two lenses directs the light onto the camera. Due to the lack of space around the ac trap chamber the camera cannot be placed in direct line of sight.

3.6.2 Imaging setup

The atoms are imaged on the $5^2S_{1/2}(F=2) \rightarrow 5^2P_{3/2}(F=3)$ transition and they are typically probed on resonance, i.e., the AOM for the detection beam (AOM4) is set to 80 MHz. The setup for imaging the atoms onto the CCD chip is shown schematically in Fig. 3.22. The beam is coupled out of an optical fiber and collimated to a FWHM of about 4 mm. This collimated beam has an intensity of 30 to 100 μW and is linearly polarized. The detection beam is sent through the atom cloud for a short exposure time which is usually around 200 μs . Short exposure times are chosen to ensure that the atom cloud is not expanding significantly during the imaging, and that the laser beam is not transferring momentum to the cloud. Figure 3.23 shows a photograph of the setup. Two lenses are used to image the cloud. Both lenses are achromatic doublets to avoid spherical aberrations. The first lens has a 60-mm focal length and is placed 60 mm away from the cloud. A second lens with a focal length of 100 mm is placed in front of the camera. This lens has a bigger diameter of 50 mm to ensure that all the light from the first lens is captured and there is no vignetting. The first lens and the camera are each placed on a translation stage to precisely adjust their position. The overall magnification factor M is calculated from the focal lengths of the lenses as $M = f_2/f_1 = 1.67$. The magnification in the z direction can also be directly measured by watching the cloud fall under the influence of gravity. The position of the cloud center is first measured versus the fall time; then g is calculated from the parabolic fit and compared with the known value. This is a useful method to precisely determine

the magnification.

The CCD camera (Theta System, SiS1-s285M) used in the experiment is a high-resolution 14-bit camera system. The CCD image sensor (Sony ICX285AL) is very sensitive with a high quantum efficiency of more than 65% at 780 nm. It has square pixels with a size of $6.45 \mu\text{m} \times 6.45 \mu\text{m}$. The entire array consists of 1392×1040 pixels, i.e., the chip has a size of 9×6.7 mm. It is controlled by an image acquisition software called ‘Vision’ running in a Borland C++ environment. The program is written specifically for BEC experiments and can be downloaded from the web [155]. The fitting routines which determine the size, number, and density of the cloud are also implemented in this program.

Imaging between the electrodes of the ac trap turned out to be difficult due to reflections from the shiny surface of the electrodes. To minimize these reflections, the beam was sent through a 2-mm wide black mask before it entered the ac trap chamber.

3.6.3 Temperature of the atom cloud

The temperature of the trapped cloud is determined with a time-of-flight (TOF) measurement. The laser fields and the magnetic (or electric) fields are switched off at a well defined time t_0 in the experimental sequence. The cloud is allowed to ballistically expand, and after a certain time of flight an absorption image of the atoms is taken. This procedure is repeated several times for increasingly longer times of flight. Assuming a uniform distribution of the cloud at the switch-off time $t_0 = 0$, the temperature can be calculated from the recorded expansion of the cloud. The density distribution at a later time can be calculated by convoluting the initial density distribution with the Maxwell-Boltzmann velocity distribution of the expanding cloud. Assuming that the initial Gaussian density distribution is not correlated with the velocity distribution, the density distribution of the atom cloud along the probing direction x is evolving as:

$$n(x, t) \propto \exp\left(-\frac{x^2}{2\sigma(t)^2}\right). \quad (3.9)$$

The width of the cloud at a later time can then be expressed in terms of the temperature T of the cloud:

$$\sigma_i(t) = \sqrt{\sigma_i^2(0) + \frac{k_B T}{m} t^2}, \quad i = y, z. \quad (3.10)$$

A fit to the cloud for every shot yields $\sigma_y(t)$ and $\sigma_z(t)$. To determine the temperature in both directions y and z , all σ are plotted versus the time of flight. Those data points are then fit to Eq. 3.10 which yields the temperature T and $\sigma_i(0)$ as fit parameters.

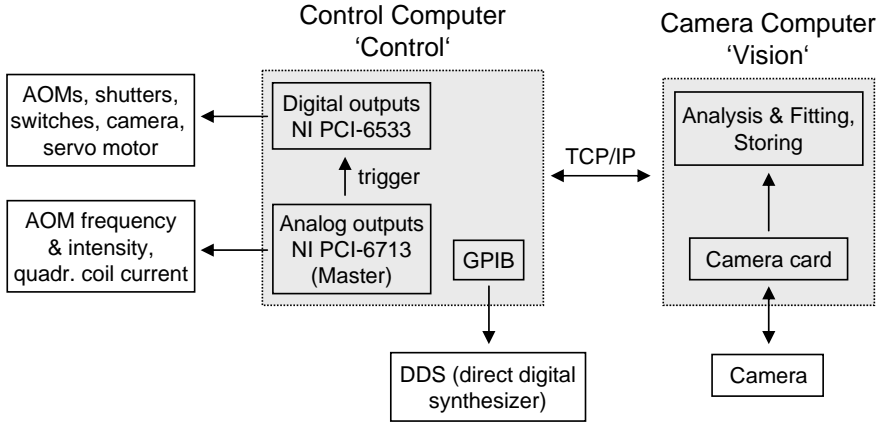


Figure 3.24: Computer control diagram illustrating the different cards in the two computers used in the experiment. The ‘control computer’ has two PCI cards and a GPIB card to produce all the output signals. The ‘camera computer’ controls the CCD camera and data acquisition, and communicates to the ‘control computer’ over TCP/IP.

3.7 Computer control

We use two computers to control the experiment. One computer controls the timing of the experiment and generates all the signals needed using a computer program called ‘Control’ [156]. The program is written in Visual C++ and was developed specifically for Bose-Einstein condensation experiments. We downloaded ‘Control’ from the web and adapted it for our experimental needs. The program provides a programming interface which allows the user to easily change the parameters and the timings employed in the experimental sequence. With this interface, a sequence can be started using interactive buttons. Also, a series of measurements can be programmed, executed and run on its own. The program communicates with the second computer which is used for data acquisition and the camera control over TCP/IP. On the second computer the program ‘Vision’ is installed which is specifically designed to control scientific CCD cameras, as mentioned in Sec. 3.6. This second computer acquires the image data, and analyzes and stores them together with the experimental parameters.

Precise timing is essential for all cold-atom experiments where a time resolution down to the μs range is required. Two PCI cards (National Instruments, NI PCI-6533 (digital) and NI PCI-6713 (analog)) are used to generate the digital and analog signals. ‘Control’ is designed to support these National Instruments cards. The NI PCI-6533 card has 32 digital output channels and produces all

external trigger signals for the AOMs, the shutters, the IGBT, the servo motor, and the camera. The NI PCI-6713 card has 8 analog output channels with an output resolution of 12 bit, and an output range of ± 10 V. It is used as master clock, i.e., this card generates the clock signals that update the output waveforms. The clock pulses are generated using the 20 MHz oscillator of the master card which is divided by an integer in ‘Control’. In our experiment, we set the update frequency to 200 kHz which relates to a resolution of $5\text{ }\mu\text{s}$. Additionally, a GPIB card is used for sweeping the rf frequency during the forced evaporation stage.

Chapter 4

Preparation of the cold atom cloud

4.1 General sequence

To obtain a cold sample of magnetically trapped atoms, it is necessary to apply a series of successive experimental steps. For each of these experimental stages, different experimental techniques and parameters are used. In this chapter, all steps are described in detail, and the corresponding experimental data are presented.

The timing diagram of a typical experimental procedure is presented in Fig. 4.1. Depending on the experiment, some stages can be left out in the experimental sequence, i.e., if we want to characterize the molasses stage, the subsequent stages except for the imaging will be omitted. Usually, an experimental sequence is executed as follows: first, the Rb atoms are collected for 5 to 10 s in the six-beam magneto-optical trap (MOT) which is loaded from the Zeeman slower. The Zeeman slower is then switched off and a compressed MOT (CMOT) stage is applied. A subsequent stage of molasses cooling further reduces the temperature of the atoms, before the laser light is switched off and the atoms are spin polarized to the $F = 2, m_F = +2$ magnetic sublevel by optical pumping. Next, the atoms are transferred to the quadrupole magnetic trap by ramping up the current in the quadrupole coils. A short stage of evaporative cooling is then applied, where a linear rf frequency ramp is carried out. The atoms can be imaged in the MOT chamber to characterize the cloud at the end of a certain stage, e.g., the MOT, CMOT, or molasses cooling stage. This is accomplished by sending a detection beam along the path of the optical pumping beam. Alternatively, the atoms can be transferred to the second vacuum chamber by horizontally moving the quadrupole coils along 42 cm. In this vacuum chamber, ac trapping experiments can be performed which will be

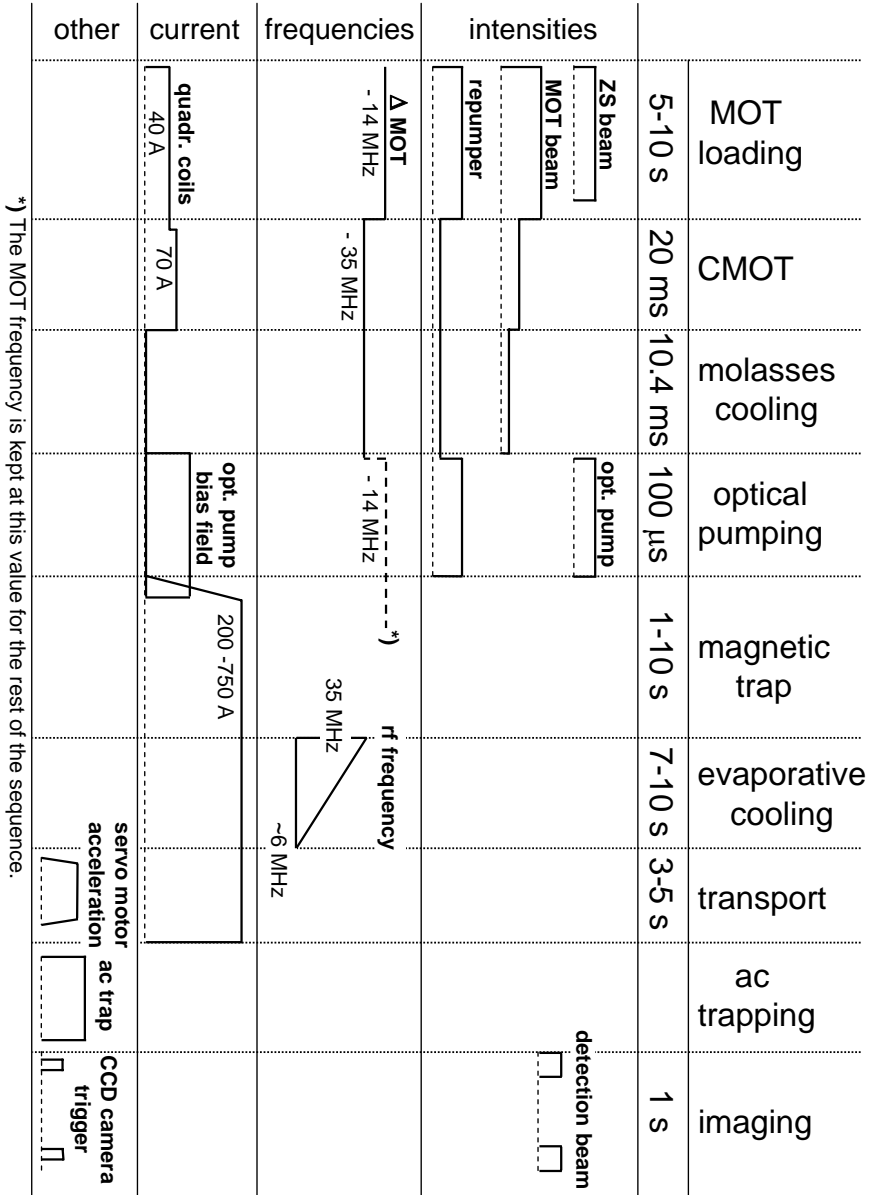


Figure 4.1: Timing diagram of a typical experimental sequence. Shown are the different cooling and trapping stages with the corresponding laser intensities and frequencies, the magnetic fields, the rf frequency, and other trigger signals. While the shutter $S1$ for the MOT beams stays closed, AOM1 is switched back on, which is necessary for the optical pumping beam. At the same time, the cooler detuning is changed back to -14 MHz and remains at this value for the rest of the sequence.

described in detail in chapter 5. Finally, the atoms are detected by absorption imaging in this second chamber. The cloud size, atom number and density are determined using the two-dimensional Gaussian fitting procedure in ‘Vision’.

4.2 The six-beam MOT loaded from the Zeeman slower

The sequence starts with continuous loading of the six-beam MOT with pre-cooled atoms from the Zeeman slower. The Zeeman slower is started up, i.e., its 28 magnetic coils, the additional coil at the other side of the glass cell (Sec. 3.4.1), and the Zeeman slower beam are switched on. In the Zeeman slower laser beam, cooling and repumping light are overlapped. The cooling light is detuned 160 MHz to the red of the $F = 2 \rightarrow F = 3$ cooling transition, while the repumper light has the same frequency as in the MOT. The Zeeman slower beam has the same circular polarization as the MOT beam along the symmetry axis z of the magnetic field.

At the same time that the Zeeman slower is started up, the MOT beams and the repumper beam for the MOT are switched on. The frequency of the MOT beams is usually detuned by -14 MHz from the cooling transition. The IGBT switch is closed and the current in the quadrupole coils is set to $I = 40$ A. To get a stable, round MOT we make sure that all six beams have equal intensities, and that they have the correct circular polarization. In a first rough alignment, the six MOT beams are aligned to the viewports of the glass cell. Then, the beams are further adjusted while looking at the fluorescence of the MOT with our CCD detection camera and another small, black-and-white CCD camera (Wetech Electronics, WM-172R) until the MOT looks round and stable. The position of the MOT center is compared with the center of the magnetic trap by ramping up the current in the quadrupole trap and watching the fluorescing cloud. We align the beams until the cloud center is no longer moving when the magnetic fields are changed. With adjusted beams we can confine up to 1×10^9 atoms in the MOT which has a cloud diameter of typically 4 to 6 mm. The temperature is about $300 \mu\text{K}$.

After the MOT has been loaded for about 5 to 9 s, the Zeeman slower beam is switched off by closing the two shutters $S2$ and $S3$ on the laser table. Due to the beam arrangement on the optical table, two shutters are needed to completely extinguish the Zeeman slower beams. At the same time, the magnetic field of the slower is switched off, including the additional coil. As discussed in Sec. 3.4.1, the Zeeman slower beam slightly disturbs the atom cloud because it is intersecting the MOT beams in the upper region of the MOT. Therefore, we wait 100 ms after the Zeeman slower has been switched off, to make sure that the MOT is in stable equilibrium. Only then we proceed with the next stage.

4.2.1 Compressed MOT (CMOT)

In the compressed MOT stage the temperature of the atom cloud is lowered and the density is increased. First, we jump the detuning of the MOT beams to -35 MHz by changing the frequency of AOM1 to 62.5 MHz, and decrease their intensity by 25%. The repumper beam is also decreased in intensity to about 5% of its former value. Two milliseconds later, the current in the quadrupole trap is raised to 70 A. The CMOT parameters are adjusted to yield the highest atom number. Ramping instead of jumping the detuning and the intensity of the MOT beams, or the magnetic field, did not result in a higher atom number. It is important to overlap the cloud centers of the MOT and the CMOT. A large offset of the centers introduces additional kinetic energy, and increases the temperature of the cloud. The whole CMOT stage lasts 20 ms. In this stage, the density is increased by one order of magnitude, and the temperature drops to about $100\ \mu\text{K}$.

4.2.2 Optical molasses

An optical molasses phase is applied next in the experimental sequence. During the optical molasses, the intensity of the MOT beams is further decreased to 50% of the MOT power, while the detuning stays at -35 MHz. The repumper intensity and frequency are kept at the CMOT value. The magnetic field, however, is switched off by opening the IGBT switch. At a current of 70 A, the field vanishes within less than $50\ \mu\text{s}$. During the 10.4-ms optical molasses stage, the temperature of the cloud is substantially decreased to about $15\text{--}30\ \mu\text{K}$.

A series of typical absorption images of the optical molasses phase is shown in the first row of Fig. 4.3. For these measurements, the atoms are loaded in the MOT and compressed in the CMOT. After optical molasses cooling, the atoms expand freely for different TOFs. The pictures show the cloud for a TOF of 4, 8, 12, and 16 ms. The cloud is expanding very little with increasing TOF, because the atoms have a low temperature of about $15\ \mu\text{K}$. Note that for longer TOFs the cloud center is shifted towards the bottom edge of the picture because the atoms are falling down due to gravity.

4.3 Magnetic trap and transport

4.3.1 Optical pumping

In the MOT the atoms are in principle distributed over all magnetic sublevels. To efficiently load the atoms into the magnetic trap, the atomic sample needs to be spin polarized such that all atoms are in the desired low-field-seeking sublevel of the ground state. As discussed in Sec. 3.1.2, the low-field-seeking sublevels in the ground state of ^{87}Rb are $F = 1, m_F = -1$, $F = 2, m_F = +1$,

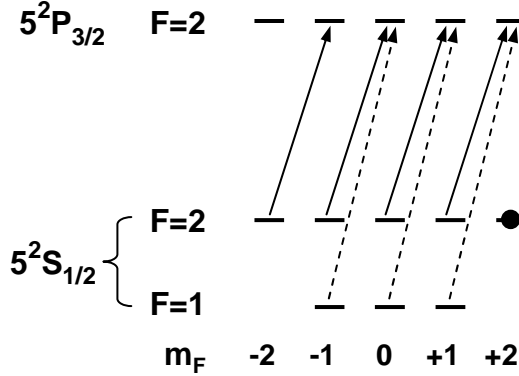


Figure 4.2: Principle of optical pumping. The optical pumping beam is circularly polarized (σ^+) and tuned to the $5^2S_{1/2} F=2 \rightarrow 5^2P_{3/2} F=2$ transition. It only drives transitions with $\Delta m = +1$. After a few pumping cycles, the atoms will accumulate in the $m_F = +2$ sublevel which is a dark state. If an atom falls down to the $F=1$ ground state, the repumper beam will bring it back up to the $F=2$ state (dashed lines).

and $F=2, m_F = +2$. In our experiment, we bring the atoms into the $F=2, m_F = +2$ stretched state by means of optical pumping.

The principle of optical pumping is illustrated in Fig. 4.2. The optical pumping beam is tuned to the $5^2S_{1/2} F=2 \rightarrow 5^2P_{3/2} F=2$ transition and is circularly polarized. A homogenous magnetic field is necessary in order to provide a quantization axis. A weak magnetic bias field is therefore applied along the beam axis during optical pumping. The laser beam is then σ^+ polarized with respect to this axis and it drives only transitions with $\Delta m = +1$. Atoms that have been pumped to the upper state decay to the sublevels of the lower state with $\Delta m = \pm 1$ and $\Delta m = 0$. Hence, after a few pumping cycles, the atoms will accumulate in the $m_F = +2$ sublevel which is a dark state, i.e., no further pumping to an upper level is possible. In case an atom falls down to the $F=1$ ground state, the repumper beam will bring it back up to the $F=2$ state.

In the optical pumping stage, the MOT beams are first quickly switched off with the AOM. The shutter $S1$ is also closed which is important because a small amount of MOT light can already disturb the optical pumping procedure significantly. The intensity of the repumper is increased to full power, and the magnetic bias field is switched on. The homogeneous bias field is created by two additional coils and is about 700 mG at the position of the atom cloud. The light for the optical pumping beam is transmitted through the partially reflecting mirror (98% reflectivity) behind $AOM1$, as shown in Fig. 3.9. Therefore, a

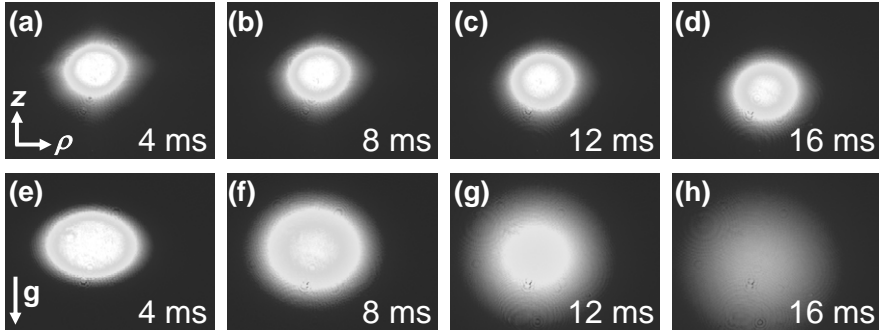


Figure 4.3: Absorption pictures of the atom cloud. In the first row [(a)-(d)] the ballistic expansion is imaged after molasses cooling, with atom temperatures around $15\ \mu\text{K}$. The second row [(e)-(h)] shows measurements in the magnetic trap, where the temperature is around $300\ \mu\text{K}$. Therefore, the magnetically trapped cloud expands much faster compared to the molasses cooling stage. Both series show the atom cloud after a TOF of 4, 8, 12, and 16 ms. Note that the atoms are falling down due to gravity which points in the negative z direction. The position of the cloud center therefore moves towards the bottom edge of the picture for longer TOFs.

beam only passes through *AOM2* if *AOM1* is on. Next, *AOM2* is switched on and only when the shutter *S1* is completely closed *AOM1* is switched back on at full amplitude and a detuning of $-14\ \text{MHz}$. The optical pumping beam is on for $100\ \mu\text{s}$, after which the repumper beam and the optical pumping beam are simultaneously switched off. Additionally, the shutter for the optical pumping beam *S4* is closed. This is necessary because stray light quickly depletes the $m_F = +2$ level and significantly limits the lifetime of the magnetic trap. The bias field is left on to provide a quantization axis while the magnetic trap is switched on.

4.3.2 Quadrupole magnetic trap

At the beginning of the magnetic trap stage, the quadrupole coils are switched back on, i.e., the IGBT switch is closed. The coil current is either jumped or ramped to a value between 200 and 750 A. Usually, we first set the current to 150 A and wait for 50 ms. Then, within 1 s, we linearly ramp up the current to 300 - 750 A. When the quadrupole field is sufficiently large to provide a new quantization axis, the optical pumping bias field is switched off. Depending on the density of the atom cloud (which is correlated to the size of the magnetic field), it can take several seconds until the cloud is in thermal equilibrium. At a current of 750 A which corresponds to a gradient of $270\ \text{G/cm}$ in the axial

direction, we are able to trap about 5×10^8 atoms at a temperature of $600 \mu\text{K}$. In our experiment, the rubidium beam is continuously injected into the MOT chamber thereby increasing the background pressure. Depending on how long the experiment is run, the lifetime can vary from day to day. In the MOT chamber, the trap lifetime typically varies between 20 s and 30 s.

The second row in Fig. 4.3 shows absorption images of the magnetic trap for TOF values of 4, 8, 12, and 16 ms. Compared to the molasses cooling pictures in the first row, the cloud is expanding faster due to its higher temperature of about $300 \mu\text{K}$. For this specific measurement, the coil current was ramped to 500 A and a short evaporation stage was implemented where a radio frequency of 30 MHz was applied for 4 s. The forced evaporation reduced the temperature by about $100 \mu\text{K}$. Finally, the atoms were kept in the magnetic trap for another 4 s to allow for thermalization. Note that the atoms are falling down due to gravity, thus disappearing out of view for longer TOFs. In general, it is difficult to image the cloud for more than 20 ms of free fall.

4.3.3 Evaporation

To perform evaporation cooling efficiently, one has to work at high densities. Only at high densities is the collision rate sufficiently high to ensure fast thermalization of the sample. Therefore, we first ramp the current up to its maximum value of 750 A. We wait for 500 ms to allow for thermalization and then start to send in the radio frequency. We begin at 35 MHz and linearly ramp down the frequency over 5 to 10 s. As the lifetime in the MOT chamber is on the order of 25 s, it is difficult to perform a much slower rf-frequency ramp. The cloud temperature can be lowered significantly depending on the final frequency and the ramping speed, e.g., for a final frequency of 6 MHz and a ramp duration of 8.3 s approximately 2×10^7 atoms remain magnetically trapped at a temperature of $30 \mu\text{K}$.

4.3.4 Transfer of the trapped cloud

The transfer of the atom cloud is initiated by sending a trigger signal to the servo motor. The servo motor has been programmed to execute a moving procedure which starts as soon as the trigger signal is sent out. The motor linearly accelerates until the programmed maximum speed is reached. Then, the stage continues to move along at this speed. When it approaches the final position the stage is linearly decelerated until it comes to a standstill. The quadrupole coils are kept at the final position until all remaining experimental procedures have been completed and are only then moved back to their initial position in the MOT chamber. We usually transfer the cloud within 3.75 s over a distance of 42 cm. We do not detect any heating from the moving but we lose about 10% of the atoms. This loss can be attributed to the higher pressure

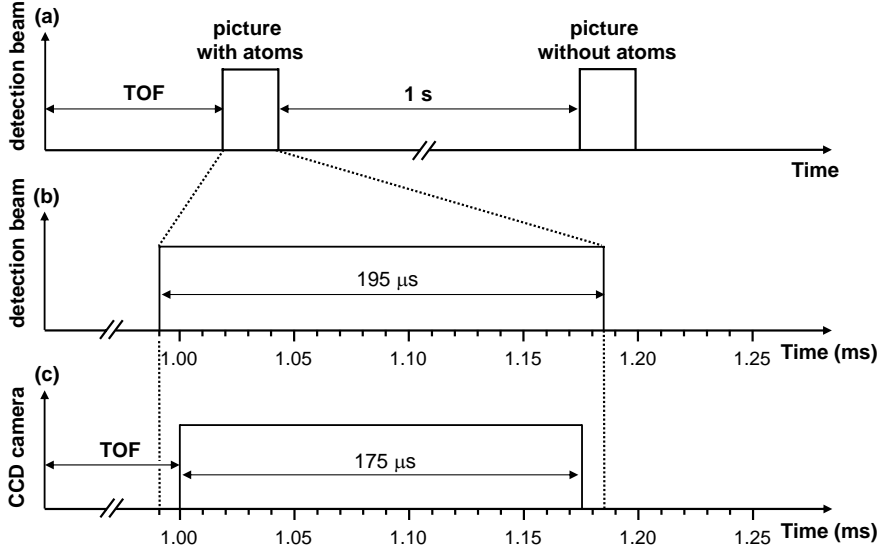


Figure 4.4: Timing of the absorption imaging procedure where the camera is switched on after a time of flight (TOF) of 1.0 ms. (a) shows the whole imaging procedure starting with the ballistic expansion of the atom cloud during a variable TOF. A zoom-in on the first picture is shown in (b) and (c). (b) shows the trigger signal of the detection beam, and (c) the trigger signal of the camera. The camera is switched on 10 μs later than the detection beam because the AOM has a 10- μs rise time.

in the transfer line and in the second vacuum chamber. In the second vacuum chamber, we measure a lifetime of 5 to 10 s.

4.4 Imaging

When we image the magnetically trapped cloud, we immediately start with the imaging procedure after the magnetic field has been switched off. Before imaging the MOT, CMOT, or optical molasses, however, additional steps are needed. First, the magnetic field and the laser beams are switched off. As no optical pumping has been applied, the atoms can also populate the $F = 1$ ground state. Therefore, we leave the repumper light on 200 μs longer than the cooler. In this way, the atoms in the $F = 1$ state are pumped into the $F = 2$ hyperfine level and they can now be imaged on the $F = 2 \rightarrow F = 3$ transition.

The imaging procedure is illustrated in Fig. 4.4. In (a), an overview of the timing during absorption imaging is shown. First, the atoms are ballistically expanding for a time-of-flight (TOF) period which is usually between 0.5 ms

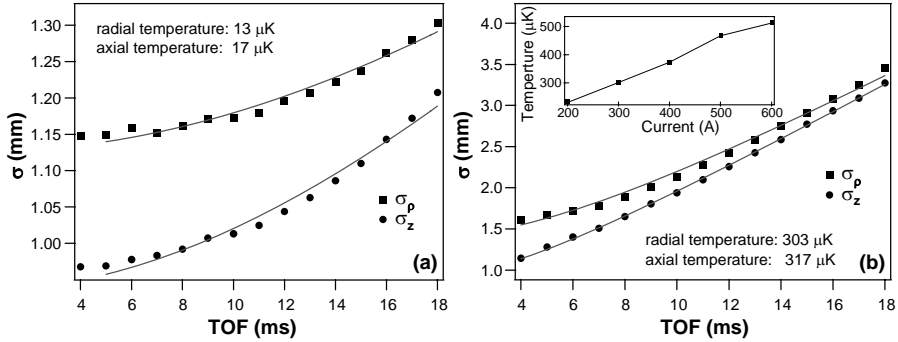


Figure 4.5: TOF measurements of the cloud after molasses cooling (a), and of the magnetic trap (b). Shown are the cloud widths in the radial and axial directions, σ_ρ and σ_z , in mm versus the TOF in ms. A fit yields a temperature of about 15 μ K for molasses cooling and a temperature of about 300 μ K for the magnetic trap. The inset in (b) shows temperature measurements in μ K versus the current in the quadrupole coils in A. As expected, the temperature rises with increasing current.

and 20 ms. Then, the atoms are imaged onto the CCD chip of the camera. Finally, a reference picture with the probe beam on, but in absence of the atom cloud, is taken as explained in Sec. 3.6. The camera needs some time for the data processing, and therefore the second picture is taken 1 s later. The imaging procedure for the second picture is identical to the one for the first picture. In (b) and (c) a zoom-in on the first detection beam pulse is shown. After a varying ballistic expansion time, the detection beam is switched on by triggering AOM4. The detection beam is usually on resonance with the $F = 2 \rightarrow F = 3$ transition, i.e., AOM4 is driven at +80 MHz. The camera is switched on 10 μ s later because the AOM has a rise time of about 8 - 10 μ s. The camera is on for 175 μ s and is then switched off. The detection beam is switched off 10 μ s later, and the second picture is taken after the picture processing time of 1 s. When a series of measurements is taken, the next sequence is started immediately afterwards.

4.5 Characteristics of the cold atom cloud

4.5.1 Temperature

Temperature measurements are important in characterizing the cold atom cloud. As already described above, Fig. 4.3 shows a typical series of TOF absorption images of molasses cooling (first row) and of the magnetic trap (second row). For every image the two-dimensional Gaussian fitting procedure

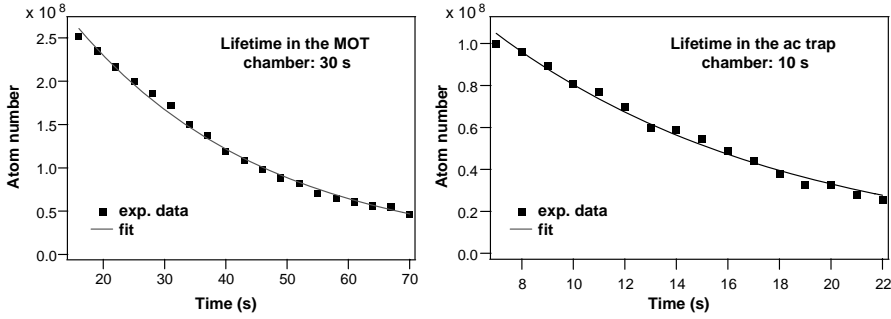


Figure 4.6: Lifetime of the magnetic trap. The atom number is plotted versus the magnetic trapping time in seconds. On the left, the measurements were taken in the MOT chamber where the lifetime was 30 s. On the right, the measurements were repeated in the ac trap chamber where the lifetime was 10 s.

in ‘Vision’ is carried out, yielding the axial and radial widths σ_ρ and σ_z of the cloud. These fit results are shown in Fig. 4.5 for both series. Plotted are σ_ρ and σ_z in mm versus the TOF in ms for the molasses cooling stage (a) and the magnetic trap (b). The temperature is determined by fitting the data to Eq. 3.10, yielding a value of about 15 μK for the molasses cooling in (a), and about 300 μK for the magnetic trap in (b).

A series of temperature measurements with varying current in the quadrupole coils is shown in the inset in (b). Plotted is the temperature in μK versus the current in A. Naturally, the density increases with higher fields in the quadrupole trap. If the transfer from a shallow to a deep trapping potential happens adiabatically, the phase-space density should remain constant, which implies that the temperature should rise with increasing current. This correlation is confirmed by our measurements.

As already mentioned in Sec. 2.1.4, Majorana spin flips occur in the zero field at the center of a quadrupole trap. This becomes increasingly important with decreasing sizes of the cloud. For a constant trap depth, a small cloud size is equivalent to a low atom temperature. The final cloud size in our experiment, however, is big enough to ensure that the trap is not affected by this loss mechanism.

4.5.2 Lifetime of the magnetic trap

Figure 4.6 shows lifetime measurements of the magnetic trap. Plotted is the number of atoms versus the magnetic trap time in seconds. The measurement on the left is performed in the MOT chamber. The experimental procedure is repeated for increasingly longer magnetic trapping times up to 70 s. An

exponential fit to the data points yields a $1/e$ lifetime of 30 s. The measurement is repeated in the ac trap chamber where the lifetime is 10 s, as shown on the right. This decrease in lifetime was explained in Sec. 3.3.2 as resulting from the reduced pumping efficiency in the ac trap chamber. Moreover, the lifetime in the second chamber was measured after the ac trap had been built in, which led to additional problems. Firstly, the trap material can outgas and deteriorate the vacuum. Secondly, rubidium can stick to the surface of the electrodes thereby increasing the local pressure. Note that the atom number is much smaller for the second measurement. The small gap between the ring electrodes reduces the cloud size, which is in turn reflected in the reduced atom number.

Chapter 5

An ac trap for rubidium

5.1 Introduction

In the previous chapters, magnetic trapping of rubidium atoms was discussed. In this chapter, we will discuss the possibility to trap ground state rubidium in an ac electric trap. Rubidium is high-field seeking in its ground state, i.e., it is attracted to the maximum in an electric field. Therefore, it is not possible to confine rubidium in a static electric trap because Maxwell's equations do not allow for a maximum of a static (electric or magnetic) field in free space. High-field seekers can, however, be confined in an electrodynamic (ac electric) trap. Similarly to trapping of ions in a Paul trap [112], three-dimensional confinement in an ac electric trap is achieved by alternating between two saddle-point configurations of the electric field. The first configuration has attractive (focusing) forces along one direction and repulsive (defocusing) forces along the other two directions, while in the second configuration the roles of the forces are reversed. Dynamic confinement of the particles is obtained by switching between these two configurations at the appropriate frequency.

In this chapter, it is experimentally demonstrated that rubidium can be confined in an ac electric trap. With our trap, it is possible to directly visualize the dynamic behavior of the atoms in the trap using absorption images taken at various phases of the ac switching cycle. These images show different cloud shapes reflecting the focusing and defocusing forces acting on the atoms. Compared to previous measurements [119], we were able to optimize

Based on/Adapted from:

Trapping of Rb Atoms by ac Electric Fields

Sophie Schlunk, Adela Marian, Peter Geng, Allard P. Mosk, Gerard Meijer, and Wieland Schöllkopf, *Phys. Rev. Lett.* **98**, 223002 (2007)

AC electric trapping of neutral atoms

Sophie Schlunk, Adela Marian, Wieland Schöllkopf, and Gerard Meijer, *Phys. Rev. A* **77**, 043408 (2008)

the number of trapped atoms by introducing an evaporative cooling stage before loading the atoms into the ac trap. As the depth of the ac trap is small, the reduction in temperature helped increase the number of confined particles, which in turn improved the quality of our images.

This chapter is organized as follows. First, the ac trap design and the electronics for switching are presented in detail in Sec. 5.2, and the theory model used for the simulations is also briefly introduced. Then, the experimental sequence used to load the atoms into the ac trap is described in Sec. 5.4. Next, we show how the atoms can be used to probe the electric fields in the trap in Sec. 5.5. The gradual formation of a stably trapped cloud in the ac trap is studied in Sec. 5.6 by imaging the atoms after an increasing number of switching cycles. This also leads to a measurement of the ac trap lifetime. Then, in Sec. 5.7, the dynamics of the atoms in the ac trap is visualized at different phases of the ac switching cycle. Additionally, the dependence of the trapped atom number on the trapping frequency and the symmetry of the switching cycle is measured. Furthermore, the phase space acceptance of the trap is probed by introducing a modified switching cycle, in Sec. 5.8. In Sec. 5.9, TOF measurements are presented, and the mean kinetic energy of the atoms is determined at various phases of the switching cycle. Finally, the prospects of sympathetic cooling of molecules using the setup presented in this thesis are discussed. Throughout the chapter, the experimental data are compared with results of numerical simulations based on full three-dimensional trajectory calculations.

5.2 AC trap setup

5.2.1 Electrode geometry and electronic setup of the ac trap

Our ac trap is cylindrically symmetric with respect to the z axis, and consists of two end cap electrodes and two ring electrodes, as shown in Fig. 5.1. The schematic on the top left is a cross section of the trap, while the photograph on the top right zooms in on the actual trap used in the experiment. The four electrodes are made of nonmagnetic stainless steel (DIN 1.3952) and are mounted between two macor (Corning Incorporated, machineable glass ceramic) plates using macor spacers. The two ring electrodes are located between the end caps, but the ring opening is not visible in the photograph on the top left as the picture is taken from the side. As indicated in the schematic, the end caps have a hemispherical shape with a diameter of 7 mm and are separated by 6 mm. The ring electrodes are 3 mm thick, corresponding to an inner semicircular shape with a radius of 1.5 mm. They have an opening diameter of 6.7 mm and are separated by a 2 mm gap. All electrodes were highly polished before the trap was assembled and were subsequently conditioned to withstand increasingly

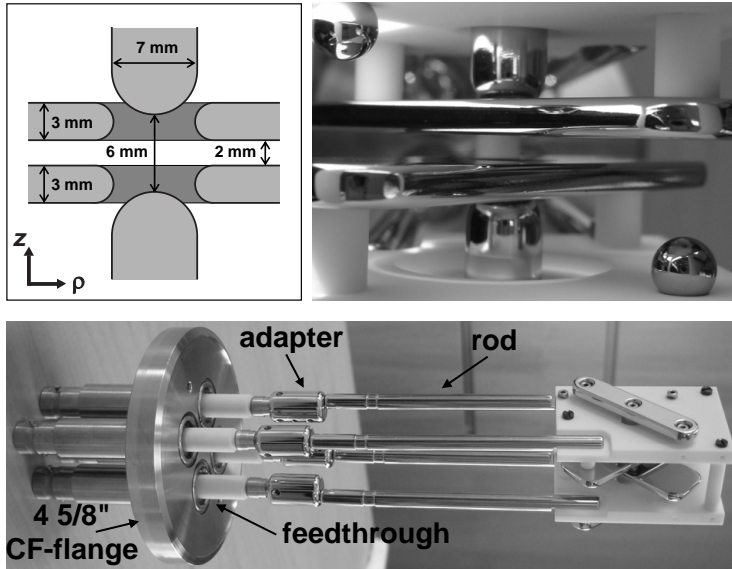


Figure 5.1: Geometry of our ac trap. The picture on the left shows a schematic of the trap where the dimensions of the electrodes and the distances between them are indicated. The photograph of the right is a close-up of the ac trap. The trap consists of two end cap electrodes and two ring electrodes where the ring opening is not visible in the photograph as the picture is taken from the side. The photograph at the bottom shows how the ac trap is mounted on four stainless steel rods that are connected to four feedthroughs on a rotatable CF- $4\frac{5}{8}$ " flange.

high voltages.

As can be seen on the photograph at the bottom of Fig. 5.1, the ac trap is mounted on four non-magnetic stainless steel rods. The rods are via stainless steel adapters rigidly screwed to four feedthroughs (Caburn MDC, HSVE20-1-W, 9271002) that are welded in a rotatable CF- $4\frac{5}{8}$ " flange. The feedthroughs are specified for a maximum voltage of 20 kV and connect the electrodes via SHV-20 plugs to the power supplies.

Each electrode is alternating between two voltages at a certain switching frequency. The switching frequencies in the experiment are below 100 Hz, and the trigger signals are provided from the computer control. The computer triggers eight high voltage switches (Behlke HTS201-03-GSM), where always two of them are connected together. The voltages are delivered by eight high voltage power supplies (FUG, HCK400-20000).

A schematic of the electronic layout is presented in Fig. 5.2. Each electrode

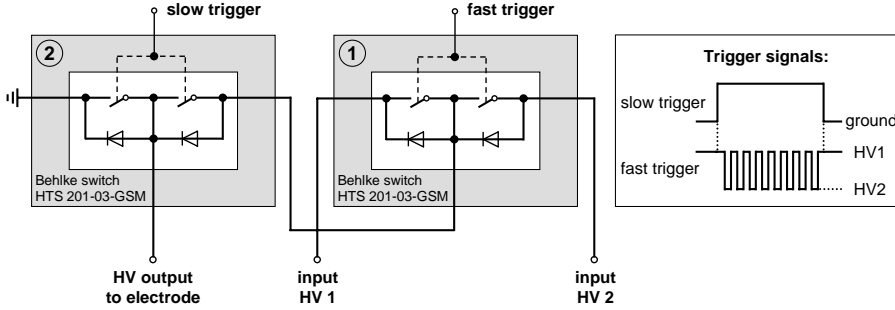


Figure 5.2: Circuit diagram of the high-voltage switches. Each electrode is switched between two voltages and ground. Two switches are connected in series. The first switch as drawn on the right alternates between HV1 and HV2. Its output is sent to the second switch which alternates between the high voltage input from the first switch and ground. The output of the second switch is connected to the electrode. On the right, the series of trigger signals as sent from the computer control to the switches is drawn schematically.

is switched between two voltages (HV1 and HV2) and ground. Two switches are connected in series to allow switching between these three potentials. The first switch, as drawn on the right, alternates between HV1 and HV2. Its output is sent to the second switch which alternates between the high voltage input from the first switch and ground. The output of the second switch is then sent to the electrode.

Both switches are controlled with trigger signals ('slow' and 'fast' trigger) from the computer as shown on the right in Fig. 5.2. To switch the ac trap on, the second switch is switched from ground to high voltage with the 'slow' trigger. The 'fast' trigger alternates between the two voltages HV1 and HV2 while the ac trap is on. To switch the ac trap off, the 'slow' trigger puts the system back to ground.

5.2.2 Electric fields in the ac trap

A superposition of a static dipole field and an alternating hexapole field is used to switch between the two saddle-point configurations. Our trapping scheme thereby follows Peik's proposal [115]. Because only the hexapole field is switched both the direction and the magnitude of the electric field at the center of the trap remain constant. Additionally, a dc quadrupole field is applied to counteract gravity. To alternate between these two configurations, two different voltage sets are applied to the four electrodes, as indicated in the schematic in Fig. 5.3.

The calculated fields the atoms experience in the two different switching

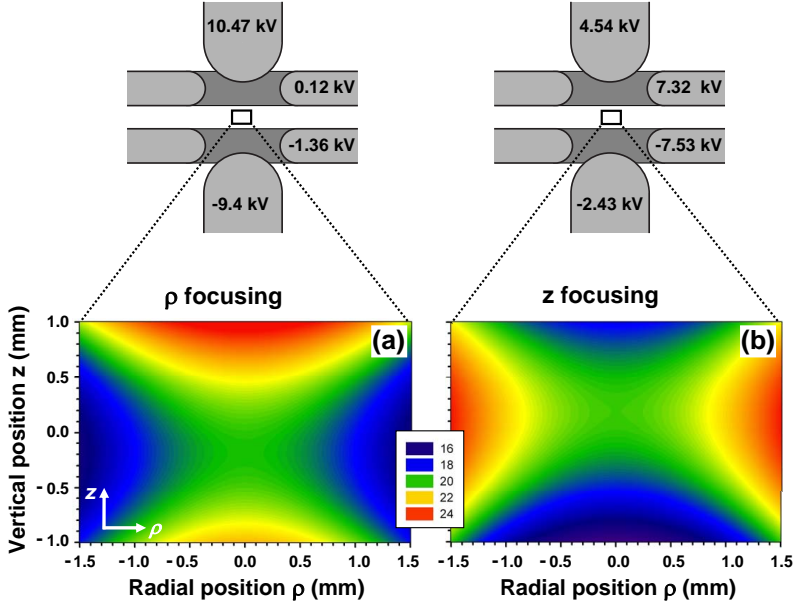


Figure 5.3: Trap voltage configurations and corresponding calculated electric field strengths in the trap. The voltages applied to the electrodes during (a) the ρ -focusing, and (b) the z -focusing phase in the switching cycle are written onto the appropriate electrode. The corresponding electric field strengths are shown in the contour plots (scale in kV/cm). The saddle point is vertically displaced due to the gravity-compensating quadrupolar field component.

configurations are shown in Figs. 5.3 (a) and (b). At the trap center, the electric field is 20 kV/cm in both configurations. For the configuration in (a), the field exhibits a maximum along the radial direction (ρ) and a minimum along the z axis, and the highest field value is found at the top of the picture. We refer to this state as ρ focusing. For the set of voltages indicated on the right-hand side of Fig. 5.3 the situation is reversed; the atoms are attracted to the center along z and repelled in the ρ direction, therefore the configuration is referred to as z focusing. Here, the highest fields are positioned symmetrically on the left and right sides of the picture. Note that the saddle points are displaced in z due to the additional dc quadrupole field. The z -direction gradients for this additional field have the same value for both trapping configurations.

The ac switching frequency is given by $1/T$, where T is the sum of the durations of the ρ -focusing and z -focusing phases, i.e., the duration of one switching cycle. At a given switching frequency, the relative duration of the two field configurations can be adjusted. This is an advantage compared to the application of a sine wave proposed in [115] where the relative duration cannot

	$\Phi_0[\text{V}]$	$\Phi_1[\text{V}]$	$\Phi_2[\text{V}]$	$\Phi_3[\text{V}]$	$\Phi_4[\text{V}]$	$\Phi_5[\text{V}]$
ρ focusing	-285	5992	604	3265	222	737
z focusing	232	5991	607	-3263	223	687

Table 5.1: Φ_i coefficients in V for our trapping geometry. The values are obtained from a multipole fit to the voltages shown in Fig. 5.3 according to Eq. 2.32.

be tuned so easily.

5.3 Trajectory calculations

Simulations are carried out to model the experimental results. First, the electric fields for our trap geometry are calculated using a commercial finite-element program (Comsol). A multipole series up to the fifth term as shown in Eq. 2.32 is then fitted to these fields. For our trap geometry, $2z_0 = 6\text{ mm}$ is the distance between the end cap electrodes. The fit yields the Φ_i coefficients which characterize the strengths of the different multipole terms. The coefficients for a fit to the voltages shown in Fig. 5.3 are given in Table 5.1. For both configurations, the dipole term Φ_1 is the dominating term in magnitude, followed by the hexapole term Φ_3 . The quadrupole term Φ_2 is smaller. Ideally, the octupole and hexapole term Φ_4 and Φ_5 would be zero, but in our trap they differ considerably from zero. These two terms are undesired nonlinearities and reduce the trap depth significantly.

From these potentials, the forces acting on the atoms are derived and trajectory calculations are carried out by numerically integrating the equations of motion. A fine grid in phase space is used to simulate the initial distribution of atoms. Throughout the chapter, the results of the simulations will be presented in conjunction with experimental data.

5.4 Experimental procedure

For all the experiments described in this chapter the following loading procedure was used; more details of the sequence can be found in chapter 4.

In the experiment, the ^{87}Rb atoms are first collected in a six-beam magneto-optical trap (MOT) loaded from a Zeeman slower. After a short compression of the MOT, optical molasses cooling, and optical pumping, the atoms are transferred into a spatially overlapped quadrupole magnetic trap. About 5×10^8 atoms in the $F = 2$, $m_F = 2$ hyperfine sublevel at a temperature of $600\text{ }\mu\text{K}$ are trapped in the magnetic trap which is characterized by a field gradient of 270 G/cm along its symmetry axis. A short evaporative cooling stage is applied next by linearly ramping a radio frequency from 35 MHz to 6 MHz in

8.3 s. At the end of the evaporative cooling stage, the field gradient is reduced to 65 G/cm. Approximately 2×10^7 atoms remain magnetically trapped at a temperature of 30 μ K. The quadrupole magnet is then moved horizontally in 3 s to a second quartz cell located 42 cm away [129]. This second ultrahigh vacuum chamber houses the ac trap. The transfer is carried out using a precision translation stage allowing for accurate overlap of the cloud with the center of the ac trap. Altogether, the cooling, trapping and transporting of the atoms take about 25 s. At the final position, the magnetic field is switched off and once it has completely disappeared, high voltage is applied to the ac trap electrodes. After a variable trapping time, the trap electrodes are switched back to ground and the confined atoms are detected by absorption imaging. In a typical experiment, the atoms are imaged 0.1 ms after the high voltage has been turned off, thereby reflecting the spatial distribution at the time of switch-off. The number of atoms is determined with an accuracy of about 5% using a two-dimensional Gaussian fitting procedure.

5.5 Mapping of the electric fields

We will now describe how the atoms can be used to sensitively probe the actual electric fields in the trap. This is important because small inaccuracies and misalignments of the electrodes can have a strong impact on the trapping fields.

To probe the electric fields in the ac trap, the usual experimental sequence is followed with the only exception that the electric fields are kept on while taking absorption images of the cloud. The atoms are confined in the ac trap for a short trapping time during the first switching cycle and the electrodes are switched to ground after obtaining the absorption images. To compensate for the resulting Stark shift, the absorption beam is detuned by several megahertz while the atoms are probed. We have already seen in Fig. 5.1 that the electric field strength varies significantly over the size of the atom cloud. Therefore, the position of an atom determines whether it is on resonance with the probing transition. Note that the absorption beam crosses the entire cloud and due to the cylindrical symmetry it can be thought of as passing once from left to right through the fields shown in the contour plots in Fig. 5.1.

In the electronic $5^2S_{1/2}(F = 2)$ ground state, the m_F sublevels remain degenerate in an electric field. In the $5^2P_{3/2}(F = 3)$ excited state, however, the degeneracy is lifted due to the tensor polarizability [157], as seen in the inset of Fig. 5.4. This gives rise to four possible energy differences (Stark shifts) between the two states, which are plotted in Fig. 5.4.

In Fig. 5.5 the first two columns show images of the atoms in the ρ -focusing and z -focusing configurations, respectively. The third and fourth columns display simulation results. For the ρ -focusing pictures in the first column, the atoms are trapped for 9.83 ms, just before switching to z focusing. For the

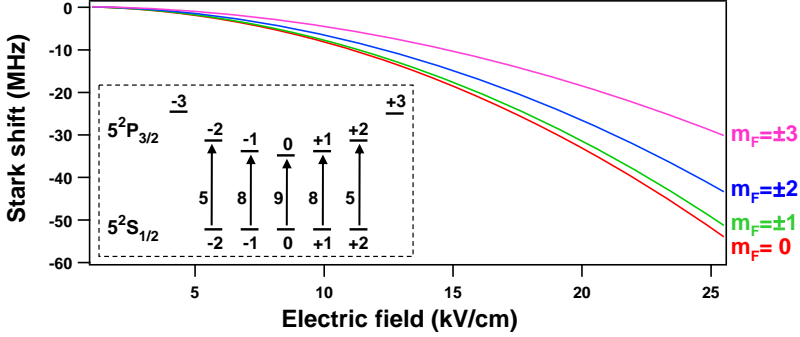


Figure 5.4: Stark shift of the $5^2S_{1/2}(F = 2) \rightarrow 5^2P_{3/2}(F = 3)$ transition used for probing. For the upper state the Stark shift is different for the $|m_F|$ sublevels, while for the lower state all m_F sublevels are degenerate. This can also be seen in the inset which shows the probing transition. All degenerate sublevels of the $5^2S_{1/2}(F = 2)$ state are populated in the trap. The linearly polarized probe beam drives only transitions with $\Delta m_F = 0$. The relative transition strengths are indicated next to the arrows.

measurements shown in the second column, the atoms are imaged immediately after switching to the z -focusing configuration, namely, after a trapping time of 9.84 ms. The difference in trapping times for the two configurations is tiny and ensures that the atom density distributions are identical. Additionally, for these short trapping times the atom cloud is dense, resulting in a good absorption signal. The experiment is repeated varying the probe detuning from -22 MHz to -38 MHz. Depending on the detuning, different electric field regions are visible, thus enabling direct probing of the field distributions shown in Fig. 5.1. For instance, the atom distributions in Figs. 5.5 (c) and (g) look like an hourglass thereby resembling the shapes of the fields in Fig. 5.1, with the saddle points located at the waist of the hourglass. As expected, the waists are displaced in z for the two pictures. The simulations, labelled with matching capital letters, agree well with the measurements.

Looking at the pictures in the first column, the lower fields corresponding to a small probe detuning are found in the center [panel (a)]. The higher fields at the top and at the bottom become visible for the larger detunings of -34 MHz in (d) and -38 MHz in (e). Note that the field strength is higher at the top than at the bottom, in agreement with Fig. 5.1 (a). The trend is reversed for the z -focusing configuration shown in the second column. For a small detuning of -22 MHz [panel (f)] atoms at the top and at the bottom are on resonance. With increasing detuning only atoms at the center of the trap are visible, confirming that along the z axis the highest fields are in the center of the trap as seen in Fig. 5.1 (b). Additionally, in the case of z focusing, the higher fields towards

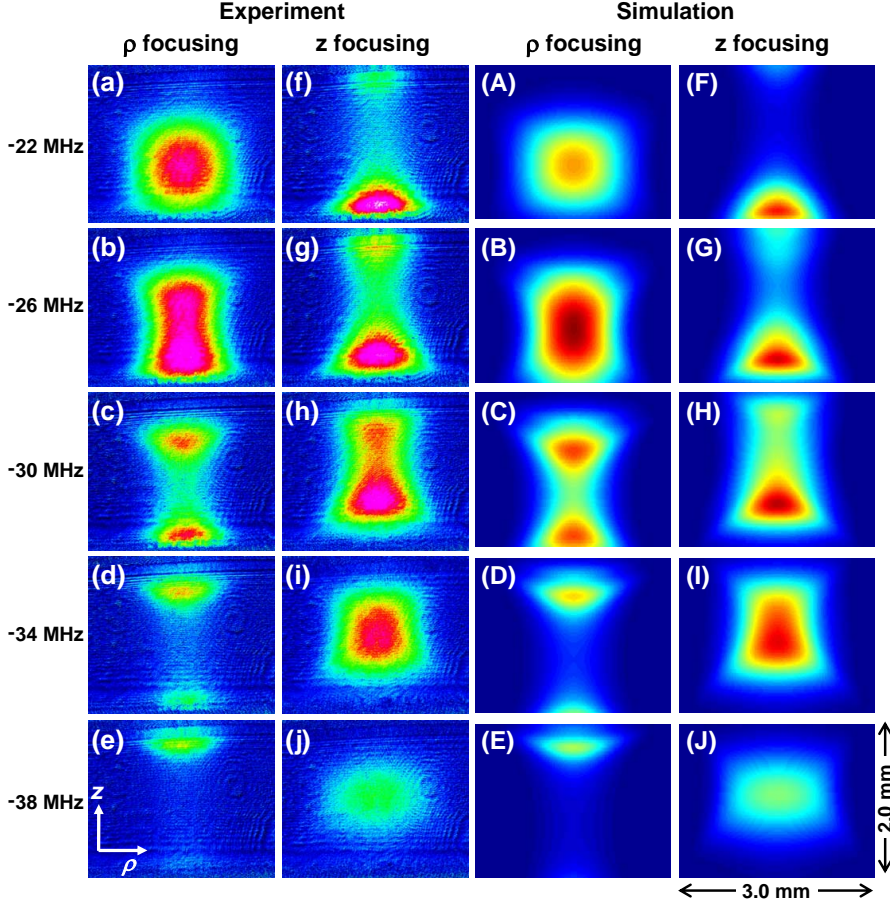


Figure 5.5: Absorption images (first two columns) and simulations (last two columns) of the atom cloud for different probe detunings with the electric fields still on. The first column displays images recorded during ρ focusing, when the atoms are kept in the trap for 9.83 ms. For the second column, the atoms are probed in the z -focusing configuration after a trapping time of 9.84 ms. All absorption images are averaged five times. The pictures in the third and fourth columns show the corresponding simulations.

larger ρ play a role. Nonetheless, the highest fields on the left and on the right side of the trap are not visible because the atom cloud is more dilute at larger ρ , and therefore the atom density is too low to image these trap regions.

As mentioned in Sec. 5.2, our simulations are carried out using a finite-element program to determine the electric field in the trap. The probe beam attenuation by an atom cloud with a Gaussian density distribution is calculated for the simulated electric fields. The resulting theory plots are shown in Figs. 5.5 (A)–(J). In the magnetic trap only the $m_F = +2$ sublevel of the $5^2S_{1/2}(F = 2)$ state is populated, while in the electric trap there no longer is a preferred orientation axis and the atoms redistribute over the degenerate m_F sublevels. However, the dipole component of the electric field is dominant at the trap center, and therefore the field points downwards along the z axis across the whole imaging region. The probe beam is linearly polarized with its polarization vector almost parallel to this axis. In general, if linearly polarized light is aligned with the quantization axis, there are no circular polarization components. Therefore, the probe beam drives only transitions with $\Delta m_F = 0$, as indicated in the inset in Fig. 5.4. Hence, no transitions to the $m_F = \pm 3$ levels of the upper $5^2P_{3/2}(F = 3)$ state are possible. The strength of the allowed transitions varies as shown in the inset in Fig. 5.4 and is accounted for in the simulations by weighting the transitions accordingly. The natural linewidth of the transition is 6 MHz; therefore the beam can simultaneously excite transitions with different m_F , if the upper sublevels are close enough in frequency. The linewidth of the laser is in the sub-MHz regime and thus has a negligible contribution.

From the simulations we determine that the actual fields in the ρ -focusing configuration are lower than expected for the ideal geometry presented in Fig. 5.1. In contrast, the simulations for z focusing match well. These lower electric fields can be reproduced by moving the lower end cap electrode down by 0.25 mm in the simulations. The calculations with the retracted end cap electrode are shown in Fig. 5.5 and they agree remarkably well with the corresponding experimental images for both trapping configurations. The displacement of the end cap results in considerable changes only for the ρ -focusing fields. In the z -focusing configuration, it is the ring electrodes that are primarily important for creating the maximum along z , whereas the end cap voltages are relatively low.

By comparing the simulations with the measurements, we conclude that in-trap imaging of the atoms is a very convenient method to monitor the electric fields in the trap. Using the simulations we are able to verify the geometry of our trap and determine possible inaccuracies. All further simulations discussed in this chapter are carried out using the fields associated with the retracted end cap geometry.

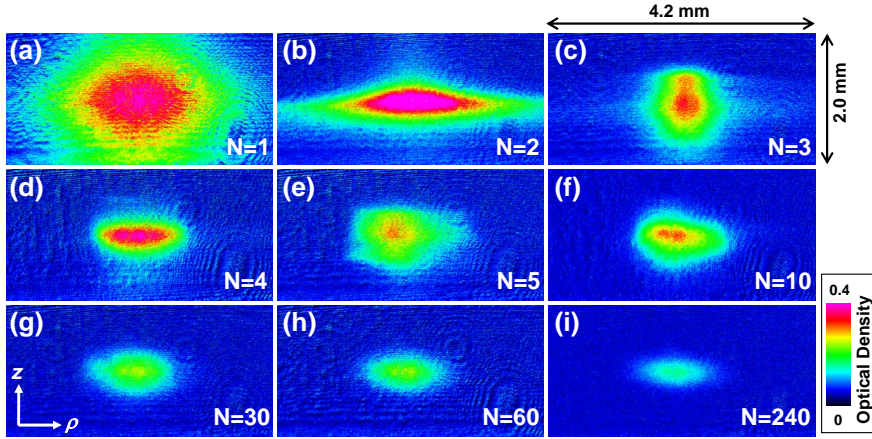


Figure 5.6: Gradual formation of the trapped atom cloud. The pictures are taken at a switching frequency of 60 Hz and show the cloud after $N = 1, 2, 3, 4, 5, 10, 30, 60$, and 240 full switching cycles. All images are averaged five times. The corresponding optical density is indicated by the color scale.

5.6 Loading the atoms in the ac trap

We will now examine the onset of stable ac electric trapping by imaging cloud shapes after a small number of switching cycles. Figure 5.6 shows the gradual formation of a trapped cloud as an increasing number N of full switching cycles is applied. The absorption images always show the 2-mm gap between the ring electrodes. In Fig. 5.6 (a) only one switching cycle at 60 Hz has been employed and the atoms completely fill the space available to them. Note that without application of this switching cycle the atoms would have by now fallen out of view due to gravity. After $N = 2$ switching cycles, as displayed in Fig. 5.6 (b), the shape of the cloud has changed dramatically. Compared to Fig. 5.6 (a), the number of atoms is now much smaller and the cloud is almost pancake shaped. In Fig. 5.6 (c) after $N = 3$ switching cycles, the cloud has taken a rounder shape. The 'final' shape emerges only after $N = 4$ switching cycles, as can be seen in Figs. 5.6 (d) and (e). However, most of the atoms are still metastably trapped and will finally escape from the trap. After $N = 5$ and $N = 10$ switching cycles, the cloud exhibits an asymmetric shape, which is visible in Figs. 5.6 (e) and (f), respectively. This asymmetry can be attributed to possible misalignments between the center of the magnetic trap and the center of the ac trap. Even after $N = 30$ switching cycles [Fig. 5.6 (g)] the shape is not as smooth as in Fig. 5.6 (h) after $N = 60$ switching cycles. A small feature is still visible on the left side of the cloud. However, the shape remains unchanged at longer trapping times, as illustrated in Fig. 5.6 (i) where

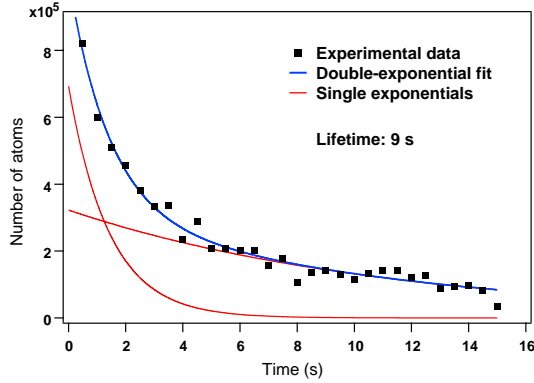


Figure 5.7: Lifetime measurement of the ac trapped atom cloud. The experiment is performed at 60 Hz, and all the data points are single-shot measurements. The solid blue line is a double-exponential fit to the data points, while the red curves show each exponential individually.

the number of atoms has decreased due to collisions with the background gas.

We also studied the atom loss from the trap more quantitatively by recording the number of atoms in the first 0.5 s of trapping. The fast decrease during the first 10 switching cycles observed in the images can be fitted by an exponential yielding a $1/e$ lifetime of about 100 ms. This can be attributed to the fact that most of the metastably trapped atoms leave the trap region within the first few switching cycles.

Figure 5.7 illustrates the lifetime in the ac trap, which is limited by the collisions with the background gas. Displayed is the number of atoms versus the trapping time in seconds. We image the atom cloud at trapping times of up to 15 s, which corresponds to $N = 900$ switching cycles at the switching frequency of 60 Hz. The data points are fit using a double exponential yielding a value of 9 s for the lifetime and a value of 1 s for the fast decay. Similarly to the 100-ms decay in the previous paragraph, this fast decay accounts for metastably trapped atoms. These atoms, however, survive in the trap much longer, as they almost have the correct initial conditions to be stably trapped. The 9-s lifetime value is consistent with measurements of a magnetically trapped cloud, performed in the same vacuum chamber.

We therefore conclude that at least 60 switching cycles have to be used in the experiment. Otherwise, the dynamics would be mainly guided by the behavior of metastably trapped atoms. Imaging the atoms after a trapping time of 1 s is a good compromise between stable behavior of the atoms and good signals, as longer trapping times suffer from atom loss due to background collisions.

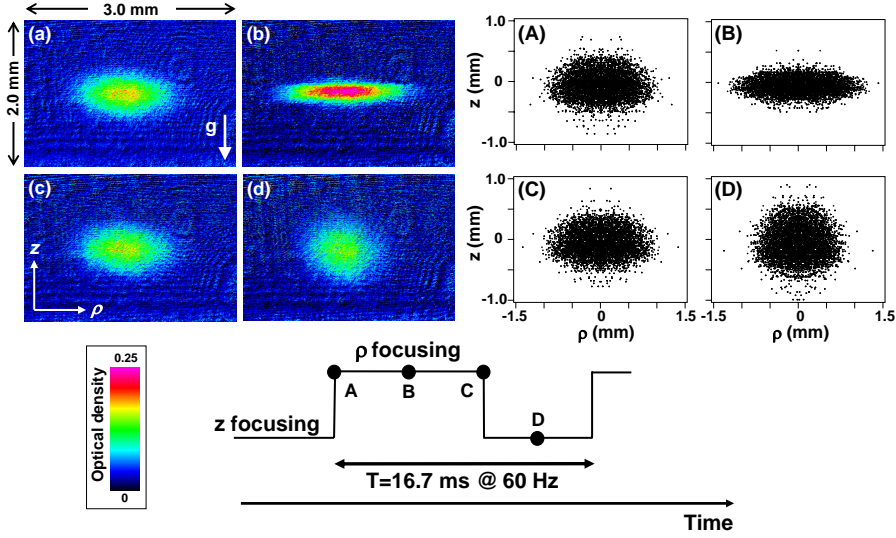


Figure 5.8: Absorption images of the atom cloud at different phases within the 61st switching cycle at a trapping frequency of 60 Hz. The pictures on the right are simulation results of the atomic distribution, labelled with matching capital letters. The schematic shows the applied switching cycle, where the appropriate phases are also indicated. The measurements are averaged five times, and the optical density is shown in the color scale.

5.7 Performance of the ac trap

In this section, we first visualize the dynamic confinement of the atoms in the trap by looking at the atomic distribution at different times within a switching cycle. From this we can qualitatively understand the motion in the trap. Next, we study the dependence of the number of trapped atoms on the switching frequency. Finally, we analyze the asymmetry of the switching cycle.

Characteristic for an ac trap is the fact that trapping is dynamic, i.e., the atoms are forced to move during the switching cycle, which is referred to as micromotion in ion traps. This can be seen in Fig. 5.8 where the images on the left show the atom cloud at different phases within the 61st switching cycle for a trapping frequency of 60 Hz. The corresponding phases A–D are indicated on the switching cycle, which is asymmetric with 59% of ρ focusing followed by 41% of z focusing.

In Fig. 5.8 (a) the atoms have just experienced z focusing and they are therefore moving inwards along z and outwards along ρ . Consequently, in the middle of ρ focusing, the cloud is focused in z and elongated in ρ , as shown in Fig. 5.8 (b). However, the ρ -focusing forces have decelerated the motion along

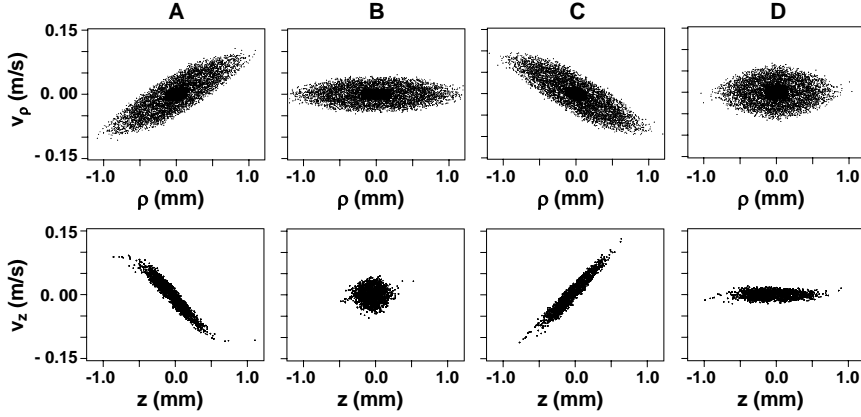


Figure 5.9: Radial (first row) and axial (second row) simulated phase space distributions of the atoms at different trap phases during the 61st switching cycle. The phase space plots are obtained for the same switch-off times A to D used in Fig. 5.8, as indicated for each column. Note that for the simulations in ρ a finer grid is used for small velocities and small positions, thus increasing the density of particles around zero.

both axes and the atoms are now at the turning point of the micromotion before they change direction. Due to this motion, inwards in ρ and outwards in z , the cloud in Fig. 5.8 (c) has a shape similar to that in (a). But as the atoms have just experienced the ρ -focusing phase, the velocity components are now pointing towards the center of the trap in ρ and outwards in z . This leads to a contraction in ρ as shown in Fig. 5.8 (d), which is recorded in the middle of z focusing where the cloud shape is round. As in (b), the atoms are at a standstill before they turn around. At the end of the switching cycle the cloud shape will be identical to the one in (a). Figures 5.8 (A)–(D) show simulations of the atomic distribution at the same switching times within the 61st cycle as the experimental data (a)–(d). The agreement between the simulations and the experimental data is very good.

Figure 5.9 illustrates the evolution of the phase space distribution during the 61st switching cycle. The radial velocity v_ρ is plotted versus ρ in the first row, and the axial velocity v_z is plotted versus z in the second row. These plots result from the same simulations carried out for the position distributions in Fig. 5.8 (A)–(D) and show the corresponding radial and axial phase space distributions. The capital letters indicate for each column the appropriate switch-off time. For the simulations in ρ , a finer grid is used for the values around zero in order to eliminate possible numerical inaccuracies.

For both coordinates ρ and z , the distribution is oscillating in both position and velocity. For the pictures in the first row, the distribution is rotating

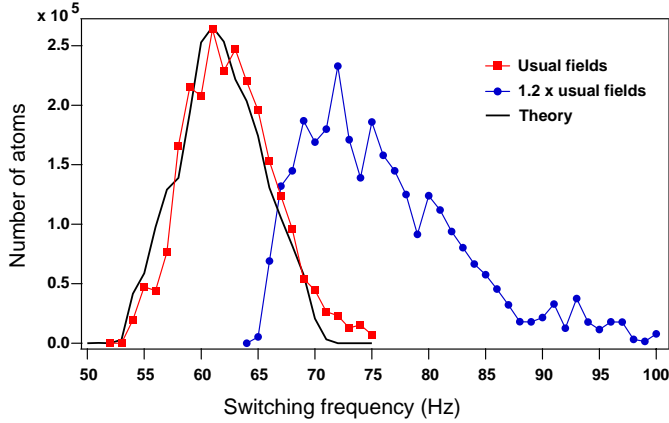


Figure 5.10: Frequency scan for two different sets of voltages. For the measurement shown in red the voltages from Fig. 5.1 are employed. The solid black curve is the corresponding theory prediction. The blue circles display measurements where higher voltages are used, resulting in electric fields that are 1.2 times stronger. The frequencies for stable trapping are then shifted to higher values. The number of atoms is measured after a trapping time of 5 s, and 10 pictures are averaged for each data point.

clockwise from A via B to C; for the second row the same happens from C via D to A. The velocity spread is maximal for A and C where the distribution is tilted by 45 degrees. Some particles are moving at a speed of more than 0.1 m/s, which corresponds to a temperature of about 50 μ K. Note that the spread in ρ and v_ρ is larger than the spread in z and v_z . As mentioned before, the atoms are at the turning point of the micromotion when they are in the middle of the focusing (defocusing) stage. The spread in position is maximal in the middle of the focusing stage, i.e., along ρ in B and along z in D, as also seen in the corresponding pictures in Fig. 5.8. On the other hand, the velocity spread is always minimal at these points, i.e., for v_ρ in B and for v_z in D. In the middle of defocusing, the cloud shape becomes round, as seen for ρ in D and for z in B. Note that the phase space distributions shown are equivalent to the phase space acceptance of the trap at that particular moment in the switching cycle. These phase space distributions have been analyzed in detail for the case of molecules moving in the same trapping configuration [118].

Figure 5.10 shows the number of trapped atoms versus the applied switching frequency after a 5-s trapping time. Two different sets of voltages are used. The red squares show a frequency scan using the voltages as indicated in Fig. 5.1. For the blue circles, the applied voltage set results in an electric field that is a factor of 1.2 higher. The solid black curve is a simulation carried out using the lower-voltage set which is in excellent agreement with the experimental data.

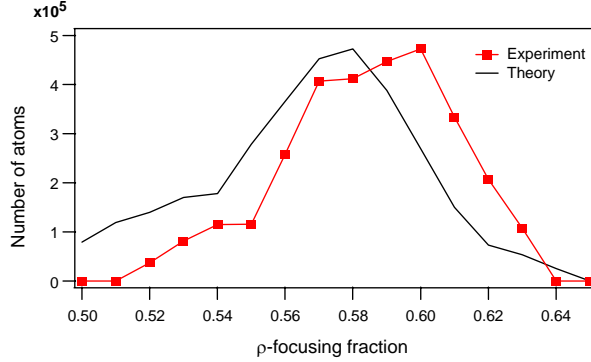


Figure 5.11: Atom number versus ρ -focusing fraction in a switching cycle of 16.7 ms corresponding to a switching frequency of 60 Hz (red squares). The data are taken after 1 s of trapping, and the measurements are averaged five times. The solid black curve is the simulation result.

For the lower voltages, trapping works in a rather narrow range between 54 Hz and 75 Hz with a maximum of 2.5×10^5 atoms trapped at 61 Hz after 5 s. No trapping is observed below the 54-Hz threshold. For the higher voltages, trapping occurs at higher switching frequencies, as expected. As with the lower voltages, there is a strong increase in signal above the threshold frequency of 64 Hz, and a slowly decreasing signal for the higher frequencies. Here, the range of working frequencies is broader. Despite the deeper trapping potential at higher voltages, the recorded number of trapped atoms is smaller, which we attribute to tiny discharges that we did not observe for the lower voltages. These discharges lead to a local increase in pressure which reduces the number of trapped atoms due to a higher rate of background collisions.

In Fig. 5.11 the relative switching time of ρ versus z focusing is varied, while the duration of the switching cycle is held constant at 16.7 ms. The first data point refers to a symmetric switching cycle with 50% of ρ focusing and 50% of z focusing, where no signal is observed. The number of trapped atoms increases with increasing ρ -focusing time. The maximum atom number after 1 s of trapping is 4.5×10^5 and is found for a switching cycle with 60% of ρ focusing. For longer ρ -focusing times the number of atoms quickly decreases with no signal observed from 64% onwards. The black curve is the corresponding theory prediction and shows the same trend as the experimental data. There is a clear shift, however, between theory and experiment, with the theoretical maximum at a smaller value of the ρ -focusing fraction. The asymmetry of the switching cycle is partly explained by the need to compensate for differences between the ideal trapping geometry and the actual experimental configuration. The experimental misalignments are likely more complex than the already mentioned

retracted end cap geometry, which is taken into account in our simulations.

5.8 Probing the phase space acceptance of the trap

The phase space acceptance can be probed by introducing a sudden change in the switching cycle. Most of the atoms have the wrong initial conditions to survive this change and they will be lost from the trap. Only the few atoms that reside in the accepted part of the phase space distribution will remain trapped if more switching cycles are applied afterwards.

For this experiment, a truncated switching cycle is applied to the stably trapped atom cloud. We will refer to this modified switching cycle as a 'phase jump'. First, 60 switching cycles with the usual 59% of ρ focusing and switching frequency of 60 Hz are applied. This ensures that most of the metastably trapped atoms have escaped from the trap. Then comes a cycle with reduced durations for both the ρ - and the z -focusing phases. This is illustrated in Fig. 5.12. In the first column, a phase jump is applied where the ρ focusing is reduced to $1/4$ and the z focusing is reduced to $3/4$ of their usual durations. For the measurements in the second column, a symmetric phase jump is applied, i.e., a $1/2$ ρ -focusing phase is followed by a $1/2$ z -focusing phase. In the third column, the measurements are again taken for an asymmetric phase jump with $3/4$ of ρ focusing and $1/4$ of z focusing.

In the first row of Fig. 5.12, the cloud is imaged directly after the phase jump. From left to right, the radial extent of the cloud decreases while the cloud becomes larger in z . In (a) the atoms have been exposed to z focusing longer than to ρ focusing, which keeps the cloud tightly together in z , whereas the atoms spread out in ρ . In (k), due to the short z -focusing phase, the cloud is spread out in z and confined in ρ . In (f) the phase jump is symmetric and the cloud shape is intermediary between the (a) and (k) situations. The pictures in the second row show the atoms after the application of an additional, full ρ -focusing phase. As a consequence, from (b) via (g) to (l) the atoms are more focused in the ρ direction. In (b) the cloud density is very low making the atoms barely visible. In (g) the cloud is fairly well confined because the atoms are not as perturbed as in (b) and (l) due to the symmetric switching. In (l) the cloud is spreading out along z as it has experienced only a short z -focusing phase. In the third row a subsequent, full z -focusing stage is applied so that the atoms have by now experienced one full switching cycle after the phase jump. In (c) the density has increased due to the z focusing, and a very dilute cloud is now visible. In (h) the cloud is pretty well confined. In (m) atoms have escaped from the trap along the z direction, the additional defocusing in ρ during the z -focusing phase leading to a dilute cloud. In the fourth row an additional ρ -focusing phase is applied. For both asymmetric phase jumps the atoms now form a small cloud. Very interesting is the pancake shape in (n), elongated

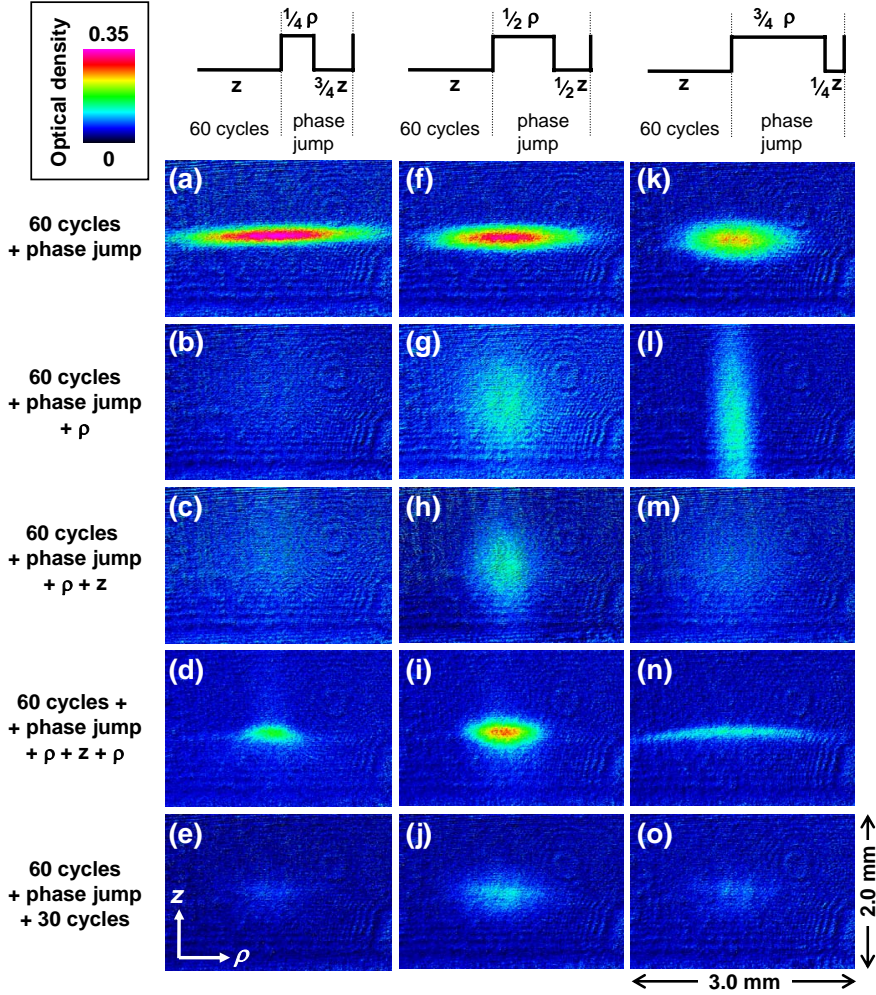


Figure 5.12: Pictures of the atom cloud after 60 switching cycles at 60 Hz followed by a phase jump. For the first column, ρ focusing is on for only $1/4$ of its usual duration and z focusing is on for $3/4$ of its usual setting. For the second column, a symmetric phase jump is performed with $1/2 \rho$ focusing and $1/2 z$ focusing. In the third column $3/4$ of ρ focusing is followed by $1/4$ of z focusing. Each column shows the atoms imaged directly after the phase jump (first row), after an additional ρ -focusing phase applied after the phase jump (second row), after a full switching cycle applied after the phase jump (third row), after a full cycle and a ρ -focusing phase (fourth row), and when 30 full switching cycles have been applied after the phase jump (last row). All pictures are averaged five times.

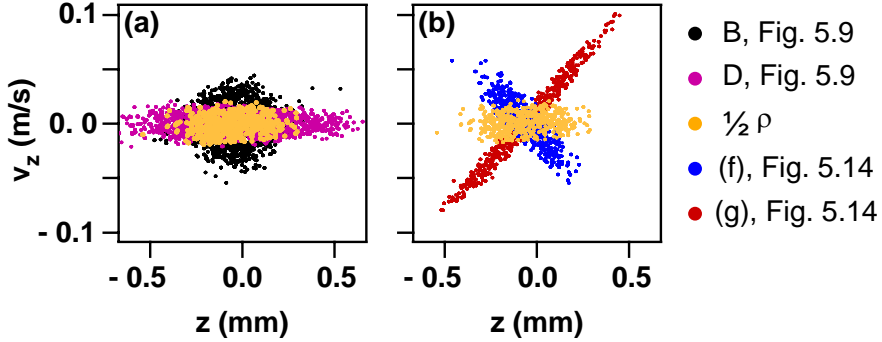


Figure 5.13: Simulated phase space distributions where v_z is plotted versus z . The figures show those atoms that survive the symmetric phase jump and the subsequently applied 30 full switching cycles. In (a), the phase space distribution after the ρ -focusing stage of the phase jump (bright orange) is plotted, along with the distributions already shown in plots B (black) and D (magenta) of Fig. 5.9. In (b), this distribution (bright orange) is shown again, along with the distributions after the entire phase jump (blue, corresponding to (f) in Fig. 5.12), and after an additional ρ -focusing stage (red, corresponding to (g) in Fig. 5.12).

along ρ and focused in z due to the prior phase of z focusing. Looking at the (l), (m) and (n) picture series, we notice that the cloud changes dramatically, being ρ focused in (l) and dilute in (m) because of the reshaping. The last row shows the atoms after 30 full switching cycles have followed the phase jump. For the asymmetric switching procedures in (e) and (o) few atoms survive, whereas in the case of symmetric switching more atoms remain confined in the trap.

As discussed for Fig. 5.9, the trap acceptance varies with the phase in the switching cycle. To visualize how the motion of the trapped atoms is perturbed by the symmetric phase jump (i.e., $1/2 \rho$ focusing followed by $1/2 z$ focusing), we carried out simulations which include the phase jump and the subsequently applied 30 full switching cycles. Note that only the atoms that survive these final 30 cycles will be discussed in the following. If this truncated switching cycle is applied, the distribution and therefore the phase space acceptance in the middle of ρ focusing is mapped onto the distribution in the middle of z focusing. This happens because the second half of ρ focusing and the first half of z focusing are missing in the modified cycle. Figure 5.13 shows the calculated phase space distributions, where v_z is displayed versus z . The phase space distribution after the ρ -focusing stage of the phase jump is presented in (a), along with the distributions already shown in plots B and in D of Fig. 5.9.

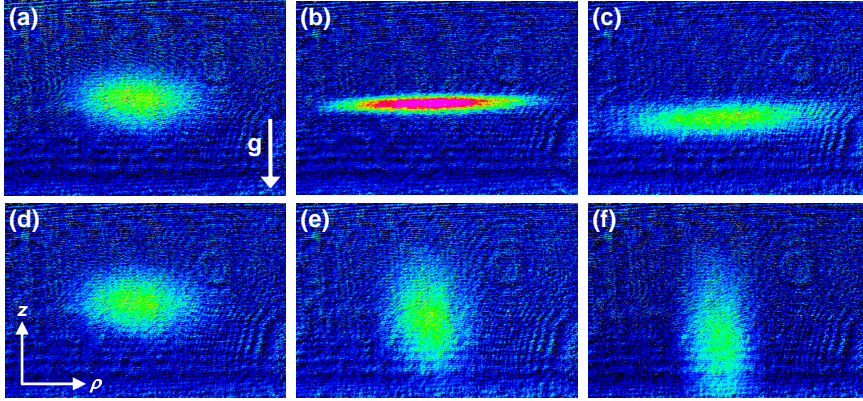


Figure 5.14: Absorption images after different free ballistic expansion times of 0.1 ms [(a),(d)], 4 ms [(b),(e)], and 7 ms [(c),(f)]. The ac trap is switched off at the end of the z -focusing phase for (a)-(c) and at the end of the ρ -focusing phase for (d)-(f). For each measurement the trapping time is 1 s and the switching frequency is 60 Hz.

Only those atoms that are in a region of phase space where the distribution after $1/2 \rho$ focusing (B, black) overlaps with the distribution after $1/2 z$ focusing (D, magenta) will remain trapped. Therefore, after the ρ -focusing stage of the phase jump the accepted phase space has reduced to this overlap region (bright orange). In Fig. 5.13 (b), this reduced distribution is again illustrated (bright orange), along with the distributions after the entire phase jump (blue, corresponding to (f) in Fig. 5.12) and after an additional ρ -focusing stage (red, corresponding to (g) in Fig. 5.12). At the end of the phase jump and therefore at the beginning of the next switching cycle (blue), the distribution has rotated clockwise by 45 degrees, as we expect from panel A in Fig. 5.9. While this distribution is narrow in both velocity and position, the distribution after an additional ρ -focusing stage (red) starts to spread out, thereby gradually refilling the whole accepted area in phase space.

It becomes clear from these simulations and the associated measurements that the overlap of the accepted areas in phase space is optimal for a symmetric phase jump. For asymmetric phase jumps, more atoms are located in the unaccepted region of phase space and will therefore be lost from the trap. This is also visible in the last row of Fig. 5.12.

5.9 Time-of-flight measurements

Figure 5.14 shows the cloud of atoms for a number of time-of-flight (TOF) values after a trapping time of 1 s at a switching frequency of 60 Hz. The

upper row of pictures shows the free ballistic expansion of the atoms directly after the z -focusing phase, whereas for the lower row the ac trap has been switched off at the end of ρ focusing. In Fig. 5.14(a) the atoms are imaged after a TOF of 0.1 ms. Given that the atoms have not moved much since the trap was switched off, this is the atomic distribution at the end of z focusing also seen in Fig. 5.8(a). After 4 ms TOF [Fig. 5.14(b)], the cloud has a pancake shape as the velocity distribution along the axial direction leads to focusing in this direction. Additionally, the cloud is expanding along ρ . Figure 5.14(c) is taken after 7 ms of expansion. The cloud has spread out in the z direction as the atoms continued to move along z ; atoms originally at the top of the cloud, are now at the bottom, and vice versa. In addition, the atoms are falling towards the electrodes at the bottom edge of the picture. Still, the cloud has a smaller diameter in the z direction than in Fig. 5.14(a). In the images (d)–(f) the atoms have just experienced ρ -focusing forces resulting in a different velocity distribution than in (a)–(c). Figure 5.14(d) shows the cloud after a TOF of 0.1 ms as already seen in Fig. 5.8(c). Now the atoms are accelerating towards the center in the radial direction and expanding in the axial direction. In Fig. 5.14(e) after 4 ms of free flight the cloud has thus become cigar shaped. In Fig. 5.14(f) after 7 ms of TOF, the cloud is even smaller in the radial direction and is falling out of view.

Using these ballistic expansion measurements of the trapped atoms, the mean kinetic energy of the cloud can be determined. The TOF measurements are carried out at various trap phases within the 61st switching cycle at our standard switching frequency of 60 Hz. Figure 5.15 (a) shows a typical TOF series where the cloud is imaged after a trapping time of 1016 ms, i.e., towards the end of the z -focusing phase. Plotted is the measured full width at half maximum (FWHM) of the cloud versus the TOF. The kinetic energy is determined from a fit to the measured FWHM, where the initial density and velocity distributions are assumed to be Gaussian. The fit yields a value of $E_\rho = k_B \times 38 \mu\text{K}$ in the radial direction (squares), and a value of $E_z = k_B \times 10 \mu\text{K}$ in the axial direction (circles) where k_B is the Boltzmann constant. Similarly to the focusing seen in Fig. 5.14, the size of the cloud in the axial direction first decreases to a minimum value at 5 ms, because the atoms are moving towards the center at this particular switch-off time. Then, the cloud FWHM increases as the atoms continue to move along z and the cloud spreads out, i.e., atoms originally at the top of the cloud are now at the bottom, and vice versa.

Figure 5.15 (b) shows the mean kinetic energy in the radial and the axial directions, E_ρ and E_z , for various ac trapping times within the same 61st switching cycle. The error bars indicate the standard deviations of the fit. The dashed lines correspond to the phases A–D of the switching cycle. As expected from Fig. 5.9, the velocities in the radial direction (squares) are higher than the velocities in the axial direction (circles) which is confirmed by our measurements. We also expect that the kinetic energy is minimal in the middle of the focusing phases, i.e., at the turning points of the micromotion, B and

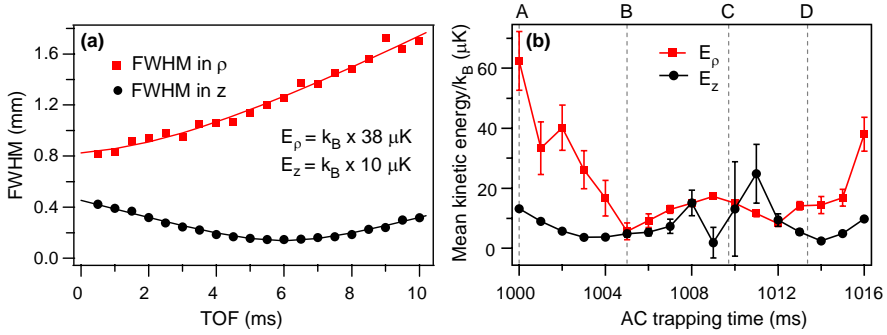


Figure 5.15: (a) Ballistic expansion measurements of the ac trapped cloud after a trapping time of 1016 ms at 60 Hz. Plotted are the measured FWHM of the cloud in the ρ (squares) and z (circles) directions versus the TOF. The solid lines show the corresponding fits. (b) Mean kinetic energies E_ρ (squares) and E_z (circles) of the atoms for various ac trapping times within the 61st switching cycle. The dashed lines indicate the times A–D in the switching cycle. All data points are plotted together with the associated error bars, which are the standard deviations of the fit.

D. Only at these phases of the switching cycle can we exclude the contribution of the micromotion to the kinetic energy. From measurements at point B and close to point D, we obtain minimum values of about $k_B \times 10 \mu\text{K}$ for the mean kinetic energy.

As the atoms do not have well-defined Gaussian velocity distributions across the entire switching cycle, the FWHM fits of the expanding cloud can have large error bars. This is primarily the case for ac trapping times where the motion of the atoms is governed by the defocusing forces, i.e., from the middle of the defocusing phase to the middle of the next focusing phase. Therefore, as seen in Fig. 5.15 (b), in the radial direction we obtain larger error bars for trapping times between D and B via A. Here we take into account the fact that the switching cycle wraps around, i.e., the end of one cycle coincides with the beginning of the next cycle. For the axial direction, the error bars are largest for trapping times between B and D, that is to say for the complementary part of the switching cycle.

5.10 Prospects for sympathetic cooling

The experimental setup presented here has been designed with the aim to sympathetically cool molecules using ultracold atoms. To avoid losses due to inelastic collisions, the molecules need to be trapped in their ground state [126], which can be accomplished by using an ac electric trap. Polarizable atoms and

polar molecules cannot be simultaneously confined in the same ac trap due to the large difference in the Stark interaction. It might be possible, however, to use an ac electric trap for the molecules and a magnetic trap for the atoms. Here, we have demonstrated that a magnetic trap for atoms can be spatially overlapped with an ac electric trap. In a separate experiment, we have also operated this ac trap with voltages and switching frequencies that would confine ground-state ND₃ molecules, while the atoms remained magnetically trapped. The switching frequency was 1 kHz and the applied voltages produced the same electric fields as used in [116]. We have thereby experimentally verified that the rubidium atoms in the magnetic trap are not perturbed by the ac electric fields needed for trapping molecules. At the same time, the magnetic fields used to trap the atoms have a negligible effect on the trapping of closed-shell polar molecules like ND₃. The compatibility of these traps is an important prerequisite for sympathetic cooling of molecules using magnetically trapped ultracold atoms.

5.11 Conclusions

In this chapter, we have presented a detailed study on trapping of rubidium in an ac electric trap. First, we showed that the atoms can be used to probe the electric fields in the trap, and we reproduced our results with simulations. By studying the gradual formation of a trapped cloud, we observed that most of the atoms that are not stably confined leave the trap within the first second. In a typical experiment, 3×10^5 atoms are stably trapped with a lifetime of about 9 s, limited by collisions with the background gas. One of the nice features of our ac trap is the ability to directly visualize the atom dynamics at different phases of the switching cycle using absorption imaging. Trajectory calculations were carried out to confirm this dynamic behavior and to understand the corresponding phase space distributions. We have also studied the dependence of the trapped atom number on the switching frequency and the symmetry of the switching cycle. Stable trapping occurs for a narrow frequency range around 60 Hz and for an asymmetric switching cycle. When a modified switching cycle is applied, the motion of the atoms in the ac trap can be readily understood from simulations of the phase space acceptance at various phases of the switching cycle. Finally, the mean kinetic energy of the trapped cloud was observed to vary across the switching cycle, as it is dominated by the micromotion in the trap. Values of about 10 μ K were measured at the points where the micromotion does not contribute.

We have also demonstrated that a magnetic trap for atoms can be spatially overlapped with an ac electric trap and have experimentally verified that the rubidium atoms in the magnetic trap are not perturbed by the ac electric fields needed for trapping molecules. The experimental setup presented here is therefore well suited to pursue cooling of ground-state molecules into the quantum

degenerate regime, either via simultaneous trapping of nonpolar molecules and atoms in an ac electric trap, or via overlapping a magnetic trap for atoms and an ac electric trap for polar molecules.

Bibliography

- [1] T.H. Maiman, *Stimulated optical radiation in ruby*. Nature **187**, 493 (1960).
- [2] A. Javan, D.R. Herriott and W.R. Bennett, *Population inversion and continuous optical maser oscillation in a gas discharge containing a He-Ne mixture*. Phys. Rev. Lett. **6**, 106 (1961).
- [3] A. Einstein, *The Collected Papers*, Vol. 5, Doc. 445. Princeton University Press (1995).
- [4] S. Bose, *Planck's law and light quantum hypothesis*. Z. Phys. **26**, 178 (1924).
- [5] A. Einstein, *Quantum theory of mono-atomic ideal gas. Second paper*. Sitzungsber. Kgl. Preuss. Akad. Wiss., 3–14 (1925).
- [6] A. Einstein, *Quantum theory of monatomic ideal gases*. Sitzungsber. Kgl. Preuss. Akad. Wiss., 261–267 (1924).
- [7] M.H. Anderson, J.R. Ensher, M.R. Matthews, C.E. Wieman and E.A. Cornell, *Observation of Bose-Einstein condensation in a dilute atomic vapor*. Science **269**, 198 (1995).
- [8] K.B. Davis, M.O. Mewes, M.R. Andrews, N.J. van Druten, D.S. Durfee, D.M. Kurn and W. Ketterle, *Bose-Einstein condensation in a gas of sodium atoms*. Phys. Rev. Lett. **75**, 3969 (1995).
- [9] J.R. Anglin and W. Ketterle, *Bose-Einstein condensation of atomic gases*. Nature **416**, 211 (2002).
- [10] M. Baranov, L. Dobrek, K. Góral, L. Santos and M. Lewenstein, *Ultracold dipolar gases - a challenge for experiments and theory*. Phys. Scr. **T102**, 74 (2002).
- [11] T. Lahaye, T. Koch, B. Fröhlich, M. Fattori, J. Metz, A. Griesmaier, S. Giovanazzi and T. Pfau, *Strong dipolar effects in a quantum ferrofluid*. Nature **448**, 672 (2007).

- [12] T.W. Hänsch and A.L. Schawlow, *Cooling of gases by laser radiation*. Opt. Commun. **13**, 68 (1975).
- [13] D. Wineland and H. Dehmelt, *Proposed $10^{14} \delta\nu/\nu$ laser fluorescence spectroscopy on Tl^+ mono-ion oscillator*. Bull. Am. Phys. Soc. **20**, 637 (1975).
- [14] D.J. Wineland, R.E. Drullinger and F.L. Walls, *Radiation-pressure cooling of bound resonant absorbers*. Phys. Rev. Lett. **40**, 1639 (1978).
- [15] W. Neuhauser, M. Hohenstatt, P. Toschek and H. Dehmelt, *Optical-sideband cooling of visible atom cloud confined in parabolic well*. Phys. Rev. Lett. **41**, 233 (1978).
- [16] W.D. Phillips and H. Metcalf, *Laser deceleration of an atomic beam*. Phys. Rev. Lett. **48**, 596 (1982).
- [17] S. Chu, L. Hollberg, J.E. Bjorkholm, A. Cable and A. Ashkin, *Three-dimensional viscous confinement and cooling of atoms by resonance radiation pressure*. Phys. Rev. Lett. **55**, 48 (1985).
- [18] S. Chu, J.E. Bjorkholm, A. Ashkin and A. Cable, *Experimental observation of optically trapped atoms*. Phys. Rev. Lett. **57**, 314 (1986).
- [19] E.L. Raab, M. Prentiss, A. Cable, S. Chu and D.E. Pritchard, *Trapping of neutral sodium atoms with radiation pressure*. Phys. Rev. Lett. **59**, 2631 (1987).
- [20] P.D. Lett, R.N. Watts, C.I. Westbrook, W.D. Phillips, P.L. Gould and H.J. Metcalf, *Observation of atoms laser cooled below the Doppler limit*. Phys. Rev. Lett. **61**, 169 (1988).
- [21] J. Dalibard and C. Cohen-Tannoudji, *Laser cooling below the Doppler limit by polarization gradients - simple theoretical-models*. J. Opt. Soc. Am. B **6**, 2023 (1989).
- [22] T. Walker, D. Sesko and C. Wieman, *Collective behavior of optically trapped neutral atoms*. Phys. Rev. Lett. **64**, 408 (1990).
- [23] H.F. Hess, *Evaporative cooling of magnetically trapped and compressed spin-polarized hydrogen*. Phys. Rev. B **34**, 3476 (1986).
- [24] J.M. Doyle, J.C. Sandberg, I.A. Yu, C.L. Cesar, D. Kleppner and T.J. Greytak, *Hydrogen in the submillikelvin regime - sticking probability on superfluid ^4He* . Phys. Rev. Lett. **67**, 603 (1991).
- [25] D.G. Fried, T.C. Killian, L. Willmann, D. Landhuis, S.C. Moss, D. Kleppner and T.J. Greytak, *Bose-Einstein condensation of atomic hydrogen*. Phys. Rev. Lett. **81**, 3811 (1998).

-
- [26] A.L. Migdall, J.V. Prodan, W.D. Phillips, T.H. Bergeman and H.J. Metcalf, *First observation of magnetically trapped neutral atoms*. Phys. Rev. Lett. **54**, 2596 (1985).
- [27] D.E. Pritchard, K. Helmerson and A.G. Martin, in *Proceedings of the 11th International Conference on Atomic Physics*. Edited by S. Haroche, J.C. Gay, and G. Grynberg, World Scientific, Singapore (1989).
- [28] C.C. Bradley, C.A. Sackett, J.J. Tollett and R.G. Hulet, *Evidence of Bose-Einstein condensation in an atomic gas with attractive interactions*. Phys. Rev. Lett. **75**, 1687 (1995).
- [29] M.O. Mewes, M.R. Andrews, D.M. Kurn, D.S. Durfee, C.G. Townsend and W. Ketterle, *Output coupler for Bose-Einstein condensed atoms*. Phys. Rev. Lett. **78**, 582 (1997).
- [30] E.W. Hagley, L. Deng, M. Kozuma, J. Wen, K. Helmerson, S.L. Rolston and W.D. Phillips, *A well-collimated quasi-continuous atom laser*. Science **283**, 1706 (1999).
- [31] M. Greiner, O. Mandel, T. Esslinger, T.W. Hänsch and I. Bloch, *Quantum phase transition from a superfluid to a Mott insulator in a gas of ultracold atoms*. Nature **415**, 39 (2002).
- [32] C.A. Regal, C. Ticknor, J.L. Bohn and D.S. Jin, *Creation of ultracold molecules from a Fermi gas of atoms*. Nature **424**, 47 (2003).
- [33] M. Greiner, C.A. Regal and D.S. Jin, *Emergence of a molecular Bose-Einstein condensate from a Fermi gas*. Nature **426**, 537 (2003).
- [34] S. Jochim, M. Bartenstein, A. Altmeyer, G. Hendl, S. Riedl, C. Chin, J. Hecker Denschlag and R. Grimm, *Bose-Einstein condensation of molecules*. Science **302**, 2101 (2003).
- [35] M.W. Zwierlein, C.A. Stan, C.H. Schunck, S.M.F. Raupach, S. Gupta, Z. Hadzibabic and W. Ketterle, *Observation of Bose-Einstein condensation of molecules*. Phys. Rev. Lett. **91**, 250401 (2003).
- [36] M.W. Zwierlein, J.R. Abo-Shaeer, A. Schirotzek, C.H. Schunck and W. Ketterle, *Vortices and superfluidity in a strongly interacting Fermi gas*. Nature **435**, 1047 (2005).
- [37] M.W. Zwierlein, A. Schirotzek, C.H. Schunck and W. Ketterle, *Fermionic superfluidity with imbalanced spin populations*. Science **311**, 492 (2006).
- [38] G. Modugno, F. Ferlaino, R. Heidemann, G. Roati and M. Inguscio, *Production of a Fermi gas of atoms in an optical lattice*. Phys. Rev. A **68**, 011601 (2003).

- [39] H. Heiselberg, C.J. Pethick, H. Smith and L. Viverit, *Influence of induced interactions on the superfluid transition in dilute Fermi gases*. Phys. Rev. Lett. **85**, 2418 (2000).
- [40] N.J. Bijlsma, B.A. Heringa and H.T.C. Stoof, *Phonon exchange in dilute Fermi-Bose mixtures: Tailoring the Fermi-Fermi interaction*. Phys. Rev. A **61**, 053601 (2000).
- [41] S. Ospelkaus, C. Ospelkaus, O. Wille, M. Succo, P. Ernst, K. Sengstock and K. Bongs, *Localization of bosonic atoms by fermionic impurities in a three-dimensional optical lattice*. Phys. Rev. Lett. **96**, 180403 (2006).
- [42] K. Günter, T. Stöferle, H. Moritz, M. Kohl and T. Esslinger, *Bose-Fermi mixtures in a three-dimensional optical lattice*. Phys. Rev. Lett. **96**, 180402 (2006).
- [43] M. Taglieber, A.C. Voigt, T. Aoki, T.W. Hänsch and K. Dieckmann, *Quantum degenerate two-species Fermi-Fermi mixture coexisting with a Bose-Einstein condensate*. Phys. Rev. Lett. **100**, 010401 (2008).
- [44] E. Wille, F.M. Spiegelhalder, G. Kerner, D. Naik, A. Trenkwalder, G. Hendl, F. Schreck, R. Grimm, T.G. Tiecke, J.T.M. Walraven, S.J.J.M.F. Kokkelmans, E. Tiesinga and P.S. Julienne, *Exploring an ultracold Fermi-Fermi mixture: interspecies Feshbach resonances and scattering properties of ^6Li and ^{40}K* . Phys. Rev. Lett. **100**, 053201 (2008).
- [45] J.J. Hudson, B.E. Sauer, M.R. Tarbutt and E.A. Hinds, *Measurement of the electron electric dipole moment using YbF molecules*. Phys. Rev. Lett. **89**, 023003 (2002).
- [46] D. DeMille, *Quantum computation with trapped polar molecules*. Phys. Rev. Lett. **88**, 067901 (2002).
- [47] A. Fioretti, D. Comparat, A. Crubellier, O. Dulieu, F. Masnou-Seeuws and P. Pillet, *Formation of cold Cs_2 molecules through photoassociation*. Phys. Rev. Lett. **80**, 4402 (1998).
- [48] C. Gabbanini, A. Fioretti, A. Lucchesini, S. Gozzini and M. Mazzoni, *Cold rubidium molecules formed in a magneto-optical trap*. Phys. Rev. Lett. **84**, 2814 (2000).
- [49] A.J. Kerman, J.M. Sage, S. Sainis, T. Bergeman and D. DeMille, *Production and state-selective detection of ultracold RbCs molecules*. Phys. Rev. Lett. **92**, 153001 (2004).
- [50] C. Haimberger, J. Kleinert, M. Bhattacharya and N.P. Bigelow, *Formation and detection of ultracold ground-state polar molecules*. Phys. Rev. A **70**, 021402 (2004).

-
- [51] M.W. Mancini, G.D. Telles, A.R.L. Caires, V.S. Bagnato and L.G. Marcassa, *Observation of ultracold ground-state heteronuclear molecules*. Phys. Rev. Lett. **92**, 133203 (2004).
- [52] D. Wang, J. Qi, M.F. Stone, O. Nikolayeva, B. Hattaway, S.D. Gensemer, H. Wang, W.T. Zemke, P.L. Gould, E.E. Eyler and W.C. Stwalley, *The photoassociative spectroscopy, photoassociative molecule formation, and trapping of ultracold $^{39}\text{K}^{85}\text{Rb}$* . Eur. Phys. J. D **31**, 165 (2004).
- [53] S.D. Kraft, P. Sta anum, J. Lange, L. Vogel, R. Wester and M. Weidemüller, *Formation of ultracold LiCs molecules*. J. Phys. B **39**, S993 (2006).
- [54] J.M. Sage, S. Sainis, T. Bergeman and D. DeMille, *Optical production of ultracold polar molecules*. Phys. Rev. Lett. **94**, 203001 (2005).
- [55] T. Bourdel, L. Khaykovich, J. Cubizolles, J. Zhang, F. Chevy, M. Teichmann, L. Tarruell, S.J.J.M.F. Kokkelmans and C. Salomon, *Experimental study of the BEC-BCS crossover region in ^6Li* . Phys. Rev. Lett. **93**, 050401 (2004).
- [56] J. Hecker Denschlag, H.C. Nägerl and R. Grimm, *Moleküle am absoluten Nullpunkt: Ultrakalte Moleküle erobern die Welt der Quantengase*. Physik Journal **3**, 33 (2003).
- [57] J.M. Doyle, B. Friedrich, J. Kim and D. Patterson, *Buffer-gas loading of atoms and molecules into a magnetic trap*. Phys. Rev. A **52**, R2515 (1995).
- [58] J. Kim, B. Friedrich, D.P. Katz, D. Patterson, J.D. Weinstein, R. DeCarvalho and J.M. Doyle, *Buffer-gas loading and magnetic trapping of atomic europium*. Phys. Rev. Lett. **78**, 3665 (1997).
- [59] J.D. Weinstein, R. DeCarvalho, J. Kim, D. Patterson, B. Friedrich and J.M. Doyle, *Magnetic trapping of atomic chromium*. Phys. Rev. A **57**, R3173 (1998).
- [60] J.M. Bakker, M. Stoll, D.R. Weise, O. Vogelsang, G. Meijer and A. Peters, *Magnetic trapping of buffer-gas-cooled chromium atoms and prospects for the extension to paramagnetic molecules*. J. Phys. B **39**, S1111 (2006).
- [61] J.G.E. Harris, R.A. Michniak, S.V. Nguyen, N. Brahms, W. Ketterle and J.M. Doyle, *Buffer gas cooling and trapping of atoms with small effective magnetic moments*. Europhys. Lett. **67**, 198 (2004).
- [62] C.I. Hancox, S.C. Doret, M.T. Hummon, L.J. Luo and J.M. Doyle, *Magnetic trapping of rare-earth atoms at millikelvin temperatures*. Nature **431**, 281 (2004).

- [63] J.D. Weinstein, R. DeCarvalho, T. Guillet, B. Friedrich and J.M. Doyle, *Magnetic trapping of calcium monohydride molecules at millikelvin temperatures*. Nature **395**, 148 (1998).
- [64] W.C. Campbell, E. Tsikata, H.I. Lu, L.D. van Buuren and J.M. Doyle, *Magnetic trapping and Zeeman relaxation of NH ($X^3\Sigma^-$)*. Phys. Rev. Lett. **98**, 213001 (2007).
- [65] M. Stoll et al., *Trapping of chromium and manganese hydride*. In preparation (2008).
- [66] R. DeCarvalho, J.M. Doyle, B. Friedrich, T. Guillet, J. Kim, D. Patterson and J.D. Weinstein, *Buffer-gas loaded magnetic traps for atoms and molecules: A primer*. Eur. Phys. J. D **7**, 289 (1999).
- [67] D. Egorov, T. Lahaye, W. Schöllkopf, B. Friedrich and J.M. Doyle, *Buffer-gas cooling of atomic and molecular beams*. Phys. Rev. A **66**, 043401 (2002).
- [68] D. Egorov, W.C. Campbell, B. Friedrich, S.E. Maxwell, E. Tsikata, L.D. van Buuren and J.M. Doyle, *Buffer-gas cooling of NH via the beam loaded buffer-gas method*. Eur. Phys. J. D **31**, 307 (2004).
- [69] J.D. Weinstein, R. DeCarvalho, C.I. Hancox and J.M. Doyle, *Evaporative cooling of atomic chromium*. Phys. Rev. A **65**, 021604 (2002).
- [70] H.L. Bethlem, G. Berden and G. Meijer, *Decelerating neutral dipolar molecules*. Phys. Rev. Lett. **83**, 1558 (1999).
- [71] H.L. Bethlem and G. Meijer, *Production and application of translationally cold molecules*. Int. Rev. Phys. Chem. **22**, 73 (2003).
- [72] C.E. Heiner, H.L. Bethlem and G. Meijer, *Molecular beams with a tunable velocity*. Phys. Chem. Chem. Phys. **8**, 2666 (2006).
- [73] H.L. Bethlem, G. Berden, F.M.H. Crompvoets, R.T. Jongma, A.J.A. van Roij and G. Meijer, *Electrostatic trapping of ammonia molecules*. Nature **406**, 491 (2000).
- [74] H.L. Bethlem, F.M.H. Crompvoets, R.T. Jongma, S.Y.T. van de Meerakker and G. Meijer, *Deceleration and trapping of ammonia using time-varying electric fields*. Phys. Rev. A **65**, 053416 (2002).
- [75] J.R. Bochinski, E.R. Hudson, H.J. Lewandowski, G. Meijer and J. Ye, *Phase space manipulation of cold free radical OH molecules*. Phys. Rev. Lett. **91**, 243001 (2003).

- [76] S.Y.T. van de Meerakker, P.H.M. Smeets, N. Vanhaecke, R.T. Jongma and G. Meijer, *Deceleration and electrostatic trapping of OH radicals*. Phys. Rev. Lett. **94**, 023004 (2005).
- [77] E.R. Hudson, C. Ticknor, B.C. Sawyer, C.A. Taatjes, H.J. Lewandowski, J.R. Bochinski, J.L. Bohn and J. Ye, *Production of cold formaldehyde molecules for study and control of chemical reaction dynamics with hydroxyl radicals*. Phys. Rev. A **73**, 063404 (2006).
- [78] S. Hoekstra, M. Metsälä, P.C. Zieger, L. Scharfenberg, J.J. Gilijamse, G. Meijer and S.Y.T. van de Meerakker, *Electrostatic trapping of metastable NH molecules*. Phys. Rev. A **76**, 063408 (2007).
- [79] S. Jung, E. Tiemann and C. Lisdat, *Cold atoms and molecules from fragmentation of decelerated SO₂*. Phys. Rev. A **74**, 040701 (2006).
- [80] F.M.H. Cromptoets, H.L. Bethlem, R.T. Jongma and G. Meijer, *A prototype storage ring for neutral molecules*. Nature **411**, 174 (2001).
- [81] F.M.H. Cromptoets, H.L. Bethlem, J. Küpper, A.J.A. van Roij and G. Meijer, *Dynamics of neutral molecules stored in a ring*. Phys. Rev. A **69**, 063406 (2004).
- [82] C.E. Heiner, D. Carty, G. Meijer and H.L. Bethlem, *A molecular synchrotron*. Nature Phys. **3**, 115 (2007).
- [83] H.L. Bethlem, A.J.A. van Roij, R.T. Jongma and G. Meijer, *Alternate gradient focusing and deceleration of a molecular beam*. Phys. Rev. Lett. **88**, 133003 (2002).
- [84] K. Wohlfart, F. Filsinger, F. Grätz, H. Haak, J. Küpper and G. Meijer, *Decoupling of longitudinal and transverse motion in the Stark decelerator using alternating gradient focusing*. In preparation (2007).
- [85] M.R. Tarbutt, H.L. Bethlem, J.J. Hudson, V.L. Ryabov, V.A. Ryzhov, B.E. Sauer, G. Meijer and E.A. Hinds, *Slowing heavy, ground-state molecules using an alternating gradient decelerator*. Phys. Rev. Lett. **92**, 173002 (2004).
- [86] M.R. Tarbutt and E.A. Hinds. *Private communications*.
- [87] K. Wohlfart, F. Grätz, F. Filsinger, H. Haak, G. Meijer and J. Küpper, *Alternating-gradient focusing and deceleration of large molecules*. Phys. Rev. A **77**, 031404 (2008).
- [88] P.F. Barker and M.N. Shneider, *Slowing molecules by optical microlinear deceleration*. Phys. Rev. A **66**, 065402 (2002).

- [89] G.J. Dong, W.P. Lu and P.F. Barker, *Decelerating and bunching molecules with pulsed traveling optical lattices*. Phys. Rev. A **69**, 013409 (2004).
- [90] R. Fulton, A.I. Bishop and P.F. Barker, *Optical Stark decelerator for molecules*. Phys. Rev. Lett. **93**, 243004 (2004).
- [91] R. Fulton, A.I. Bishop, M.N. Shneider and P.F. Barker, *Controlling the motion of cold molecules with deep periodic optical potentials*. Nature Phys. **2**, 465 (2006).
- [92] R. Fulton, A.I. Bishop, M.N. Shneider and P.F. Barker, *Optical Stark deceleration of nitric oxide and benzene molecules using optical lattices*. J. Phys. B **39**, S1097 (2006).
- [93] N. Vanhaecke, U. Meier, M. Andrist, B.H. Meier and F. Merkt, *Multistage Zeeman deceleration of hydrogen atoms*. Phys. Rev. A **75**, 031402 (2007).
- [94] S.D. Hogan, D. Sprecher, M. Andrist, N. Vanhaecke and F. Merkt, *Zeeman deceleration of H and D*. Phys. Rev. A **76**, 023412 (2007).
- [95] E. Narevicius, C.G. Parthey, A. Libson, J. Narevicius, I. Chavez, U. Even and M.G. Raizen, *An atomic coilgun: using pulsed magnetic fields to slow a supersonic beam*. New J. Phys. **9**, 358 (2007).
- [96] J. Doyle, B. Friedrich, R. Krems and F. Masnou-Seeuws, *Quo vadis, cold molecules?* Eur. Phys. J. D **31**, 149 (2004).
- [97] M.S. Elioff, J.J. Valentini and D.W. Chandler, *Subkelvin cooling NO molecules via "billiard-like" collisions with argon*. Science **302**, 1940 (2003).
- [98] M. Gupta and D. Herschbach, *A mechanical means to produce intense beams of slow molecules*. J. Phys. Chem. A **103**, 10670 (1999).
- [99] M. Gupta and D. Herschbach, *Slowing and speeding molecular beams by means of a rapidly rotating source*. J. Phys. Chem. A **105**, 1626 (2001).
- [100] S.A. Rangwala, T. Junglen, T. Rieger, P.W.H. Pinkse and G. Rempe, *Continuous source of translationally cold dipolar molecules*. Phys. Rev. A **67**, 043406 (2003).
- [101] T. Junglen, T. Rieger, P.W.H. Pinkse and G. Rempe, *Two-dimensional trapping of dipolar molecules in time-varying electric fields*. Phys. Rev. Lett. **92**, 223001 (2004).
- [102] G. Modugno, G. Ferrari, G. Roati, R.J. Brecha, A. Simoni and M. Inguscio, *Bose-Einstein condensation of potassium atoms by sympathetic cooling*. Science **294**, 1320 (2001).

-
- [103] K.J. Kügler, W. Paul and U. Trinks, *A magnetic storage ring for neutrons*. Phys. Lett. B **72**, 422 (1978).
- [104] J.J. Giliijamse, S. Hoekstra, S.A. Meek, M. Metsälä, S.Y.T. van de Meerakker, G. Meijer and G.C. Groenenboom, *The radiative lifetime of metastable CO ($a^3\Pi, v = 0$)*. J. Chem. Phys. **127**, 221102 (2007).
- [105] W.H. Wing, *On neutral particle trapping in quasistatic electromagnetic fields*. Prog. Quant. Electr. **8**, 181 (1984).
- [106] W. Ketterle and D.E. Pritchard, *Trapping and focusing ground-state atoms with static fields*. Appl. Phys. B **54**, 403 (1992).
- [107] R. Grimm, M. Weidemüller and Y. Ovchinnikov, *Optical dipole traps for neutral atoms*. Adv. Atom. Mol. Opt. Phys. **42**, 95 (1999).
- [108] T. Takekoshi, B.M. Patterson and R.J. Knize, *Observation of optically trapped cold cesium molecules*. Phys. Rev. Lett. **81**, 5105 (1998).
- [109] R.J.C. Spreeuw, C. Gerz, L.S. Goldner, W.D. Phillips, S.L. Rolston, C.I. Westbrook, M.W. Reynolds and I.F. Silvera, *Demonstration of neutral atom trapping with microwaves*. Phys. Rev. Lett. **72**, 3162 (1994).
- [110] D. DeMille, D.R. Glenn and J. Petricka, *Microwave traps for cold polar molecules*. Eur. Phys. J. D **31**, 375 (2004).
- [111] E.A. Cornell, C. Monroe and C.E. Wieman, *Multiply loaded, ac magnetic trap for neutral atoms*. Phys. Rev. Lett. **67**, 2439 (1991).
- [112] W. Paul, *Electromagnetic traps for charged and neutral particles*. Rev. Mod. Phys. **62**, 531 (1990).
- [113] M. Morinaga and F. Shimizu, *Electric trapping of neutral atoms: stability theory*. Laser Phys. **4**, 412 (1994).
- [114] F. Shimizu and M. Morinaga, *Electric trapping of neutral atoms*. Jpn. J. Appl. Phys., Part 2 **31**, L1721 (1992).
- [115] E. Peik, *Electrodynamic trap for neutral atoms*. Eur. Phys. J. D **6**, 179 (1999).
- [116] J. van Veldhoven, H.L. Bethlem and G. Meijer, *AC electric trap for ground-state molecules*. Phys. Rev. Lett. **94**, 083001 (2005).
- [117] M. Schnell, P. Lützow, J. van Veldhoven, H.L. Bethlem, J. Küpper, B. Friedrich, M. Schleier-Smith, H. Haak and G. Meijer, *A linear ac trap for polar molecules in their ground state*. J. Phys. Chem. A **111**, 7411 (2007).

- [118] H.L. Bethlem, J. van Veldhoven, M. Schnell and G. Meijer, *Trapping polar molecules in an ac trap*. Phys. Rev. A **74**, 063403 (2006).
- [119] S. Schlunk, A. Marian, P. Geng, A.P. Mosk, G. Meijer and W. Schöllkopf, *Trapping of Rb atoms by ac electric fields*. Phys. Rev. Lett. **98**, 223002 (2007).
- [120] T. Rieger, P. Windpassinger, S.A. Rangwala, G. Rempe and P.W.H. Pinkse, *Trapping of neutral rubidium with a macroscopic three-phase electric trap*. Phys. Rev. Lett. **99**, 063001 (2007).
- [121] T. Kishimoto, H. Hachisu, J. Fujiki, K. Nagato, M. Yasuda and H. Katori, *Electrodynamic trapping of spinless neutral atoms with an atom chip*. Phys. Rev. Lett. **96**, 123001 (2006).
- [122] J.J. Gilijamse, S. Hoekstra, S.Y.T. van de Meerakker, G.C. Groenenboom and G. Meijer, *Near-threshold inelastic collisions using molecular beams with a tunable velocity*. Science **313**, 1617 (2006).
- [123] D.J. Larson, J.C. Bergquist, J.J. Bollinger, W.M. Itano and D.J. Wineland, *Sympathetic cooling of trapped ions: A laser-cooled two-species nonneutral ion plasma*. Phys. Rev. Lett. **57**, 70 (1986).
- [124] N. Balakrishnan, G.C. Groenenboom, R.V. Krems and A. Dalgarno, *The He-CaH($^2\Sigma^+$) interaction. II. Collisions at cold and ultracold temperatures*. J. Chem. Phys. **118**, 7386 (2003).
- [125] H. Cybulski, R.V. Krems, H.R. Sadeghpour, A. Dalgarno, J. Klos, G.C. Groenenboom, A. van der Avoird, D. Zgid and G. Chalasinski, *Interaction of NH($X^3\Sigma^-$) with He: Potential energy surface, bound states, and collisional Zeeman relaxation*. J. Chem. Phys. **122**, 094307 (2005).
- [126] M. Lara, J.L. Bohn, D. Potter, P. Soldan and J.M. Hutson, *Ultracold Rb-OH collisions and prospects for sympathetic cooling*. Phys. Rev. Lett. **97**, 183201 (2006).
- [127] M. Lara, J.L. Bohn, D.E. Potter, P. Soldan and J.M. Hutson, *Cold collisions between OH and Rb: The field-free case*. Phys. Rev. A **75**, 012704 (2007).
- [128] A. Mosk, S. Kraft, M. Mudrich, K. Singer, W. Wohlleben, R. Grimm and M. Weidemüller, *Mixture of ultracold lithium and cesium atoms in an optical dipole trap*. Appl. Phys. B **73**, 791 (2001).
- [129] H. Lewandowski, D. Harber, D. Whitaker and E. Cornell, *Simplified system for creating a Bose-Einstein condensate..* J. Low Temp. Phys. **132**, 309 (2003).

-
- [130] D.E. Pritchard, *Cooling neutral atoms in a magnetic trap for precision spectroscopy*. Phys. Rev. Lett. **51**, 1336 (1983).
- [131] W. Petrich, M.H. Anderson, J.R. Ensher and E.A. Cornell, *Stable, tightly confining magnetic trap for evaporative cooling of neutral atoms*. Phys. Rev. Lett. **74**, 3352 (1995).
- [132] C.J. Myatt, E.A. Burt, R.W. Ghrist, E.A. Cornell and C.E. Wieman, *Production of two overlapping Bose-Einstein condensates by sympathetic cooling*. Phys. Rev. Lett. **78**, 586 (1997).
- [133] M.O. Mewes, M.R. Andrews, N.J. van Druten, D.M. Kurn, D.S. Durfee and W. Ketterle, *Bose-Einstein condensation in a tightly confining dc magnetic trap*. Phys. Rev. Lett. **77**, 416 (1996).
- [134] T. Esslinger, I. Bloch and T.W. Hänsch, *Bose-Einstein condensation in a quadrupole-Ioffe-configuration trap*. Phys. Rev. A **58**, R2664 (1998).
- [135] H.J. Metcalf and P. van der Straten, *Laser cooling and trapping*. Springer Verlag, New York, USA (1999).
- [136] W. Demtröder, *Laser spectroscopy: Basic concepts and instrumentation*. 3. edition. Springer Verlag, Berlin (2003).
- [137] C.N. Cohen-Tannoudji and W.D. Phillips, *New mechanisms for laser cooling*. Phys. Today **43**, 33 (1990).
- [138] C. Fertig and K. Gibble, *Measurement and cancellation of the cold collision frequency shift in an ^{87}Rb fountain clock*. Phys. Rev. Lett. **85**, 1622 (2000).
- [139] P. Kohns, P. Buch, W. Suptitz, C. Csambal and W. Ertmer, *On-line measurement of sub-Doppler temperatures in a Rb magneto-optical trap by trap center oscillations*. Europhys. Lett. **22**, 517 (1993).
- [140] C.D. Wallace, T.P. Dinneen, K.Y.N. Tan, A. Kumarakrishnan, P.L. Gould and J. Javanainen, *Measurements of temperature and spring constant in a magneto-optical trap*. J. Opt. Soc. Am. B **11**, 703 (1994).
- [141] C.G. Townsend, N.H. Edwards, C.J. Cooper, K.P. Zetie, C.J. Foot, A.M. Steane, P. Szriftgiser, H. Perrin and J. Dalibard, *Phase-space density in the magneto-optical trap*. Phys. Rev. A **52**, 1423 (1995).
- [142] G. Herzberg, *Atomic spectra and atomic structure*. Dover Publications (1944).
- [143] D. Auerbach, E.E.A. Bromberg and L. Wharton, *Alternate-gradient focusing of molecular beams*. J. Chem. Phys. **45**, 2160 (1966).

- [144] J. van Veldhoven, *AC trapping and high-resolution spectroscopy of ammonia molecules*. Radboud Universiteit Nijmegen, Ph.D. thesis (2006).
- [145] R.F. Wuerker, H.M. Goldenberg and R.V. Langmuir, *Electrodynamic containment of charged particles by three-phase voltages*. J. Appl. Phys. **30**, 441 (1959).
- [146] G. Breit and I.I. Rabi, *Measurement of nuclear spin*. Phys. Rev. **38**, 2082 (1931).
- [147] D.A. Steck. *Rubidium 87 D Line Data*. <http://steck.us/alkalidata>. Revision 1.6 (2003).
- [148] C.J. Pethick and H. Smith, *Bose-Einstein condensation in dilute gases*. 3. edition. Cambridge University Press, Cambridge (2002).
- [149] C.E. Wieman and L. Hollberg, *Using diode-lasers for atomic physics*. Rev. Sci. Instrum. **62**, 1 (1991).
- [150] K.B. MacAdam, A. Steinbach and C. Wieman, *A narrow-band tunable diode-laser system with grating feedback, and a saturated absorption spectrometer for Cs and Rb*. Am. J. Phys. **60**, 1098 (1992).
- [151] K.L. Corwin, Z.T. Lu, C.F. Hand, R.J. Epstein and C.E. Wieman, *Frequency-stabilized diode laser with the Zeeman shift in an atomic vapor*. Appl. Opt. **37**, 3295 (1998).
- [152] G.C. Bjorklund, *Frequency-modulation spectroscopy – new method for measuring weak absorptions and dispersions*. Opt. Lett. **5**, 15 (1980).
- [153] N. Masuhara, J.M. Doyle, J.C. Sandberg, D. Kleppner, T.J. Greytak, H.F. Hess and G.P. Kochanski, *Evaporative cooling of spin-polarized atomic-hydrogen*. Phys. Rev. Lett. **61**, 935 (1988).
- [154] E.A. Burt, R.W. Ghrist, C.J. Myatt, M.J. Holland, E.A. Cornell and C.E. Wieman, *Coherence, correlations, and collisions: What one learns about Bose-Einstein condensates from their decay*. Phys. Rev. Lett. **79**, 337 (1997).
- [155] T. Meyrath and F. Schreck. *A Laboratory Control System for Cold Atom Experiments*. <http://george.ph.utexas.edu/~schreck/schreck/>. Vision, Borland C++ 5.02 (2004).
- [156] T. Meyrath and F. Schreck. *A Laboratory Control System for Cold Atom Experiments*. <http://george.ph.utexas.edu/~schreck/schreck/>. Control, Visual C++ 6.0 (2004).
- [157] C. Krenn, W. Scherf, O. Khait, M. Musso and L. Windholz, *Stark effect investigations of resonance lines of neutral potassium, rubidium, europium and gallium*. Z. Phys. D: At., Mol. Clusters **41**, 229 (1997).

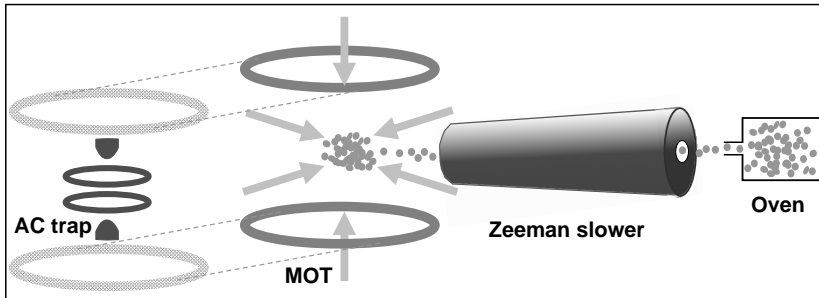
Hoofdstuk 6

Samenvatting

Het in dit proefschrift beschreven werk is verricht aan atomen die tot extreem lage temperatuur gekoeld zijn en die vervolgens werden opgesloten in een val. De bereikte temperaturen liggen in het μK gebied, veel lager dan de van nature in het heelal voorkomende temperaturen. Nadat de atomen gekoeld zijn, kunnen ze gevangen worden door gebruik te maken van magnetische of elektrische velden. In dit proefschrift wordt aangetoond dat het mogelijk is rubidiumatomen op te sluiten in een macroscopische, met wisselspanning werkende, elektrische val.

Om de atomen op ultralage temperaturen te brengen zijn laserkoelmethode gebruikt, zoals beschreven in hoofdstuk 2. Deze methoden zijn in de jaren tachtig van de vorige eeuw ontwikkeld [19] en succesvol ingezet in een groot aantal experimenten in de atoomfysica. Na het laserkoelen worden de rubidiumatomen in een magnetische val geladen en terwijl het magnetische veld de atoomwolk vasthoudt, vindt vervolgens verdampingskoeling plaats. Het principe van deze koelmethode is het langzaam verlagen van de valdiepte, waardoor de atomen met de hoogste energie kunnen ontsnappen. De overblijvende atomen komen in thermisch evenwicht op een lagere temperatuur. Op deze wijze kan de temperatuur significant omlaag gebracht worden. Verdampingskoeling van atomaire gassen is in 1991 voor het eerst gedemonstreerd [24] en bleek een beslissende stap te zijn op weg naar Bose-Einstein condensatie in atomaire gassen. Na deze koeling worden de atomen uiteindelijk van de magnetische val naar de elektrische val overgebracht.

Mijn promotieproject omvatte ook het ontwerpen, ontwikkelen en bouwen van de experimentele apparatuur, en het implementeren van de verschillende koelmethode die nodig zijn om een sample van koude rubidiumatomen te maken. Hoofdstuk 3 van dit proefschrift is gewijd aan de beschrijving van de apparatuur en in hoofdstuk 4 worden de methoden en procedures die gebruikt worden om de atomen te koelen uitgelegd. Tot slot wordt in hoofdstuk 5 de dynamica van de atomen in de elektrische val in detail beschreven, en wordt



Figuur 6.1: Schema van de experimentele opstelling met de rubidiumoven, de Zeeman vertrager, de magneto-optische val en de elektrische val.

de werking van de val beschreven als functie van de valparameters.

6.1 Een elektrische wisselspanningsval

In het onderzoeksgebied van koude atomen worden voornamelijk magnetische vallen gebruikt om paramagnetische atomen te vangen, omdat deze vallen betrouwbaar en eenvoudig te bouwen zijn. Waarom is het dan interessant om in plaats daarvan elektrische velden te gebruiken?

Deeltjes in een zogeheten laagveldzoekende toestand ondervinden een kracht in de richting van een veldminimum. Ze kunnen daarom in het minimum van een statisch elektrisch (of magnetisch) veld gevangen worden. Deeltjes in een hoogveldzoekende toestand kunnen niet in een statisch veld gevangen worden, omdat statische velden geen maximum in de vrije ruimte kunnen hebben. Omdat de grondtoestand altijd hoogveldzoekend is, zijn dynamische velden nodig om atomen en moleculen in de grondtoestand te kunnen vangen. Een elektrische wisselspanningsval is een breed inzetbare methode die toegepast kan worden op ieder atoom of molecuul in de grondtoestand. In onze groep zijn voor het eerst neutrale atomen in de grondtoestand (^{87}Rb) in een macroscopische elektrische wisselspanningsval gevangen [119]. Eerder zijn polaire moleculen [116] en strontiumatomen op een chip [121] elektrisch opgesloten. Zeer recent zijn rubidiumatomen ook in een drie-fasen elektrische val gevangen [120].

Net als bij het opsluiten van ionen in een Paul-val wordt in een elektrische wisselspanningsval de driedimensionale opsluiting bereikt door op de juiste frequentie te schakelen tussen twee zadelpuntconfiguraties van het elektrische veld. De eerste configuratie oefent aantrekkende (focuserende) krachten uit in de ene richting en afstotende (defocuserende) krachten in de andere, in de tweede configuratie zijn de rollen van de krachten precies omgedraaid.

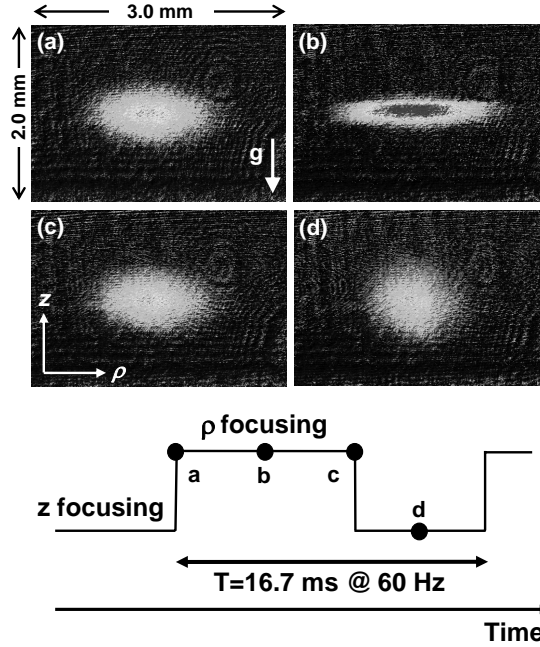


Figuur 6.2: Afbeelding van onze wisselspanningsval. De val bestaat uit twee afsluitkap-elektroden en twee ringelektroden. Het gat in de ring is niet zichtbaar omdat de afbeelding van de zijkant is genomen.

6.2 Experiment

In ons experiment worden de rubidiumatomen gekoeld in een magneto-optische val (MOT, magneto-optical trap) die geladen wordt door een straal uit een Zeeman-vertrager, zie Figuur 6.1. In een MOT worden de atomen gekoeld en opgesloten door de combinatie van laserlicht en een magnetisch veld. In onze MOT worden zes onafhankelijke stralen gebruikt, waarbij er steeds twee tegengesteld gericht zijn. Nadat de MOT enkele seconden geladen is, worden de atomen op dezelfde plaats in een magnetische val geladen, door het laserlicht uit te schakelen en de stroom in de magneetspoelen te vergroten. Terwijl de atoomwolk in de magnetische val vastgehouden wordt, passen we geforceerde verdampingskoeling toe, waardoor de temperatuur ongeveer een factor tien omlaag gaat. De koude rubidiumwolk wordt dan naar een tweede vacuümkamer gebracht door de magneetspoelen te verplaatsen. In de tweede vacuümkamer bevindt zich de elektrische wisselspanningsval, die bestaat uit vier niet-magnetische roestvrijstalen elektrodes, namelijk twee ringen en twee afsluiters, te zien in Figuur 6.2. Nadat het magneetveld is uitgeschakeld, worden twee verschillende spanningsconfiguraties afwisselend aangebracht op deze vier elektroden om tussen de zadelpuntconfiguraties te schakelen. Hierdoor vindt dynamische opsluiting van de atomen plaats.

Stabiele opsluiting van de atomen observeren we in een nauwe band van schakelfrequenties rond 60 Hz, zoals voorspeld door baanberekeningen. In een typisch experiment worden ongeveer 3×10^5 rubidiumatomen gevangen, met een levensduur van ongeveer 9 s bij een valdiepte van $10 \mu\text{K}$. Een van de goede



Figuur 6.3: Absorptie-afbeelding van de Rb-wolk op verschillende tijdstippen in de 61ste schakelcyclus, namelijk in het begin en het midden van de horizontale focussering (a, b) en in het begin en het midden van de verticale focussering (c, d). De corresponderende tijden zijn aangegeven in het schakelpatroon; de schakelfrequentie is 60 Hz, de periode is $T = 16.7$ ms.

eigenschappen van onze val is dat hij de mogelijkheid heeft de dynamische opsluiting van de atoomwolk direct te visualiseren: in absorptiebeelden die op verschillende tijdstippen in de valcyclus genomen zijn, zijn de verschillende vormen van de atoomwolk te zien die het gevolg zijn van de focuserende en defocuserende krachten (zie Figuur 6.3). We hebben de karakteristieke parameters van de val bestudeerd als een functie van de schakelcyclus en hebben dit vergeleken met de resultaten uit baanberekeningen. Bovendien laten we zien dat de atomen gebruikt kunnen worden om gevoelig de elektrische velden in de val te meten, door de atoomwolk af te beelden met de velden nog aan. We bepalen ook het acceptatievolume van de val in de faseruimte door de schakelcyclus plotseling te veranderen.

Tot slot bespreken we de vooruitzichten voor het koelen van moleculen door thermisch contact met ultrakoude atomen, die als koelmiddel dienen. De hier beschreven opstelling is zeer geschikt voor experimenten gericht op het koelen

van moleculen in de grondtoestand tot in het kwantumontaarde regime. Dit kan gebeuren door apolaire moleculen en atomen tegelijk in een elektrische val in te vangen, of door een magnetische val voor atomen te combineren met een elektrische wisselspanningsval voor polaire moleculen.

Chapter 7

Summary

The work presented in this thesis is carried out on neutral atoms that are cooled to very low temperatures and subsequently confined in a trap. The temperatures are typically in the μK range which is much lower than the naturally occurring temperatures anywhere in the universe. After the atoms have been cooled, it is possible to trap them using either magnetic or electric fields. Here, it is demonstrated that rubidium atoms can be confined in a macroscopic ac electric trap.

To bring the atoms to ultralow temperatures, the technique of laser cooling and trapping is used as explained in chapter 2. This method was developed in the 1980s [19] and was successfully used in a large number of experiments in atomic physics. The rubidium atoms are then loaded into a magnetic trap. While the cloud is held in place by the forces of the magnetic field, a stage of evaporative cooling is applied. The principle of this cooling technique is to gradually lower the trap depth, thus letting the most energetic atoms escape and the remaining atoms rethermalize. In this way, the temperature of a trapped sample can be decreased significantly. Evaporative cooling was demonstrated in 1991 for the first time [24] and turned out to be one of the key steps to achieve Bose-Einstein condensation. After this cooling stage, the atoms are transferred from the magnetic trap into the ac electric trap.

My PhD project also involved the design, development, and assembly of the experimental setup, as well as the implementation of the various cooling methods that are needed to prepare a sample of cold rubidium atoms. Chapter 3 of this thesis is dedicated to the description of the experimental setup, while chapter 4 explains the methods and the experimental procedure used to cool and trap the atoms. Finally, in chapter 5, the atom dynamics in the ac electric trap are investigated in detail and the performance of the trap is studied as a function of the trapping parameters.

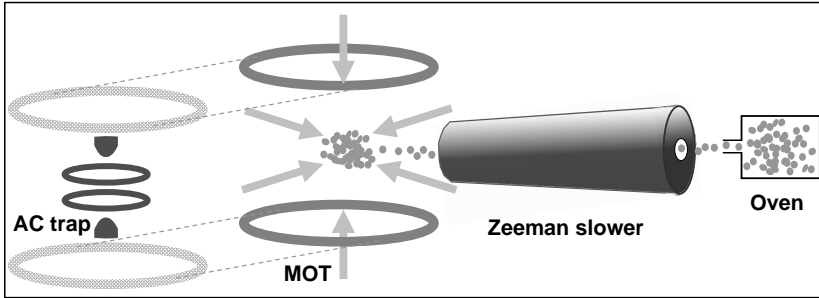


Figure 7.1: Schematic of the experimental setup with the rubidium oven, the Zeeman slower, the MOT, and the ac electric trap.

7.1 Principle of ac electric trapping

In the field of ultracold atoms, mostly magnetic traps are used to confine paramagnetic atoms, because this type of trap is easy to implement and works reliably. Why is it interesting to use electric fields instead?

Particles in a so-called low-field-seeking state are always attracted to lower field regions. They can thus be trapped in the minimum of a static electric or magnetic field. Particles in a high-field-seeking state, however, cannot be trapped in a static field, since such fields cannot possess a maximum in free space. Therefore, dynamic fields have to be used to trap atoms and molecules in their ground state, which is always high-field seeking. Trapping by ac electric fields is a very versatile method applicable to any ground-state atom or molecule. Our group was the first to demonstrate trapping of ground-state neutral atoms (^{87}Rb) in a macroscopic ac electric trap [119]. AC electric trapping has been previously achieved for polar molecules [116] as well as strontium atoms on a chip [121], and recently for rubidium atoms in a three-phase electric trap [120].

Similarly to trapping of ions in a Paul trap, three-dimensional confinement in an ac electric trap is achieved by switching at the right frequency between two saddle-point configurations of the electric field. The first configuration has attractive (focusing) forces along one direction and repulsive (defocusing) forces along the other two directions, while for the second configuration the roles of the forces are reversed.

7.2 Experiment

In our experiment, the rubidium atoms are cooled in a magneto-optical trap (MOT) loaded from a Zeeman slower, as shown in the schematic in Fig. 7.1. In a MOT the atoms are cooled and trapped by the combination of the laser



Figure 7.2: Photograph of our ac trap. The trap consists of two end cap electrodes and two ring electrodes; the ring opening is not visible in the photograph as the picture is taken from the side.

light and an additionally applied magnetic field. For our MOT, six independent laser beams are used where always two of them are counterpropagating. After the MOT has been loaded for several seconds, the atoms are transferred into a spatially overlapped magnetic trap by switching off all laser beams and ramping up the current in the magnetic field coils. While the cloud is held in the magnetic trap, a stage of forced evaporation is applied, which lowers the temperature of the sample by about one order of magnitude. The cold rubidium cloud is then transferred, by physically moving the coils, into a second vacuum chamber housing the AC trap. Our trap consists of four nonmagnetic stainless steel electrodes, namely two end caps and two rings as shown in Fig. 7.2. After the magnetic field has been turned off, two different sets of voltages are alternately applied to these four electrodes to switch between the two saddle-point configurations. This leads to dynamic confinement of the atoms.

Stable electric trapping is observed in a narrow range of switching frequencies around 60 Hz, in agreement with trajectory calculations. In a typical experiment, about 3×10^5 rubidium atoms are trapped with lifetimes on the order of 9 s and trap depths of about $10 \mu\text{K}$. One of the nice features of our trap is the ability to directly visualize the dynamic confinement of the atoms in the trap; absorption images of the trapped cloud taken at various phases of the ac switching cycle show different shapes reflecting the focusing and defocusing forces acting on the atoms (see Fig. 7.3). The operation characteristics of the trap are studied as a function of the switching-cycle parameters and then compared with the results from our trajectory calculations. Additionally, we show that the atoms can be used to sensitively probe the electric fields in the trap by

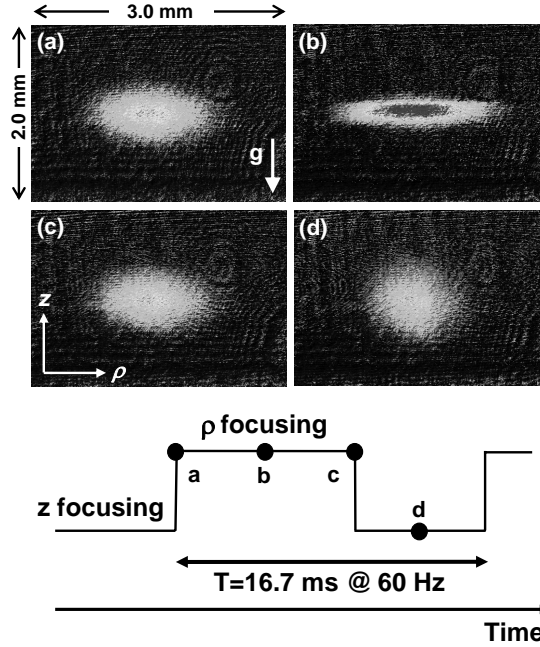


Figure 7.3: Absorption images of the Rb cloud at different times within the 61st switching cycle, i.e., at the beginning and middle of the ρ -focusing (a, b) and at the beginning and middle of the z -focusing (c, d) phase. The corresponding times are indicated in the switching pattern; the switching frequency is 60 Hz, giving a period of $T = 16.7$ ms.

imaging the cloud while the fields are still on. We also probe the phase space acceptance of the trap by introducing a sudden change in the switching cycle.

Finally, the prospects of sympathetic cooling of molecules using ultracold atoms as a coolant are addressed. It is found that the setup presented here is well suited to pursue cooling of ground-state molecules into the quantum degenerate regime, either via simultaneous trapping of nonpolar molecules and atoms in an ac electric trap or via overlapping a magnetic trap for atoms and an ac electric trap for polar molecules.

Appendix

Physical properties of ^{87}Rb

Atomic number	Z	37
Total nucleons	$Z + N$	87
Atomic mass	m	86.909 180 520(15) u $1.443\,160\,60(11) \times 10^{-25}$ kg
Relative natural abundance	η	27.83(2)%
Nuclear lifetime	τ_{n}	4.88×10^{10} yr
Vapor pressure at 25°C	P_{v}	4.0×10^{-7} mbar
Melting point	T_{m}	39.31°C
Boiling point	T_{b}	688°C
Nuclear spin	I	3/2
Ionization limit	E_{Ion}	33 690.804 8(2)cm $^{-1}$ 4.177 127 0(2) eV

Table A.1: Physical properties of ^{87}Rb . All values are taken from [147].

Optical properties of ^{87}Rb

Wavelength (vacuum)	λ	780.246 291 629(11) nm
Lifetime	τ	26.24(4) ns
Natural linewidth/ Decay rate	Γ	$2\pi \cdot 6.065(9)$ MHz $38.11(6) \times 10^6 \text{ s}^{-1}$
Maximum acceleration	$\frac{\hbar k \Gamma/2}{m}$	$0.110 \times 10^6 \text{ m/s}^2$
Recoil energy	ω_{r}	$2\pi \cdot 3.7709$ kHz
Recoil velocity	v_{r}	5.8845 mm/s
Recoil temperature	T_{r}	361.95 nK
Doppler velocity	v_{D}	11.8 cm/s
Doppler temperature	T_{D}	146 μK

Table A.2: Properties of the D_2 ($5^2S_{1/2}(F=2) \rightarrow 5^2P_{3/2}(F=3)$) transition of ^{87}Rb . Values are taken from [147].

Electron spin g -factor	2.002 319 304 373 7(80)
Nuclear g -factor	−0.000 995 141 4(10)
Magnetic Dipole Constant $A_{5^2S_{1/2}}$	3.417 341 305 452 15(5) GHz
Ground state polarizability $\alpha_0(5^2S_{1/2})$	$h \cdot 0.0794(16) \text{ Hz}/(\text{V}/\text{cm})^2$
D_2 scalar polariz. $\alpha_0(5^2P_{3/2}) - \alpha_0(5^2S_{1/2})$	$h \cdot 0.1340(8) \text{ Hz}/(\text{V}/\text{cm})^2$
D_2 tensor polariz. $\alpha_0(5^2P_{3/2})$	$h \cdot -0.0406(8) \text{ Hz}/(\text{V}/\text{cm})^2$

Table A.3: Important magnetic and electric field interaction parameters. Values are taken from [147].

Vapor pressure of Rubidium

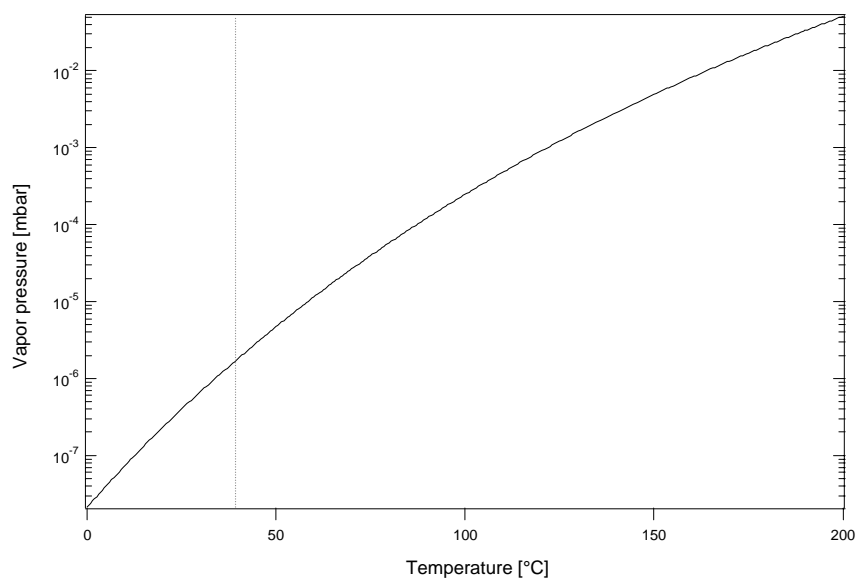


Figure A.4: Vapor pressure of rubidium in mbar versus the temperature in °C. The values were obtained using formulas that can be found in [147]. The vertical line indicates the melting point of rubidium at 39.3°C.

Curriculum Vitae

Sophie Schlunk

Born on August 13, 1976 in Schwäbisch Hall, Germany

- | | |
|-------------|--|
| 1996 | Abitur at the Hohenzollerngymnasium Sigmaringen, Germany |
| 1997 - 1999 | Physics studies at the Eberhard-Karls-Universität Tübingen, Germany |
| 1999 - 2001 | Physics studies at the Freie Universität Berlin, Germany |
| 2001 - 2002 | Research for the diploma thesis under the supervision of Prof. Dr. K. Burnett at the Clarendon Laboratory, Oxford University, United Kingdom. Subject of the diploma thesis: “Cold atoms in a periodic optical potential - a system for studying quantum chaos” |
| 2003 - 2008 | PhD student employed by the “Stichting voor Fundamenteel Onderzoek der Materie” (FOM) in the group of Prof. dr. G.J.M. Meijer. My PhD work was started in April 2003 at the FOM Instituut voor Plasmafysica “Rijnhuizen” in Nieuwegein, the Netherlands. As of December 2003, the experiment was carried out at the Fritz-Haber-Institut der Max-Planck-Gesellschaft in Berlin, Germany. |